UNIVERSITÀ DEGLI STUDI DI BERGAMO
SCHOOL OF ENGINEERING
DEPARTMENT OF ENGINEERING AND APPLIED SCIENCES
DOCTORAL PROGRAMME IN ENGINEERING AND APPLIED SCIENCES

INCIDENCE EFFECTS ON AERODYNAMIC AND THERMAL PERFORMANCE OF A FILM-COOLED GAS TURBINE NOZZLE GUIDE VANE

Doctoral Dissertation of:
HAMED ABDEH

Supervisor:
Prof. Antonio Perdichizzi

Tutor:
Prof. Giovanna Barigozzi

The chair of doctoral Program:
Prof. Valerio Re

Year 2017 - Cycle XXX

Abstract

In this study, the influence of inlet flow incidence on the aerodynamic and thermal performance of a film cooled linear nozzle vane cascade is fully assessed. Tests have been carried out on a solid and a cooled cascade. In the cooled cascade, coolant is ejected at the end wall through a slot located upstream of the leading edge plane. Moreover, a vane showerhead cooling system is also realized through 4 rows of cylindrical holes. The cascade was tested at a high inlet turbulence intensity level (Tu_1 = 9%) and at a constant inlet Mach number of 0.12 and nominal cooling condition, varying the inlet flow angle. In addition to the reference incidence angle (0°), four other cases were investigated: +20°, +10°, -10° and -20°. The aero-thermal characterization of vane platform was obtained through 5-hole probe, endwall and vane showerhead adiabatic film cooling effectiveness measurements. Vane load distributions and surface flow visualizations supported the discussion of the results. On the vane, a significant movement in stagnation point happened when incidence angle varied, resulted in changing of the coolant distribution pattern between SS and PS of the cooled vane; which adversely affects the efficiency for both negative and positive inlet flow incidence angles. On the platform, however, a relevant negative impact of positive inlet flow incidence on the cooled cascade aerodynamic and endwall thermal performance was detected. A negligible influence was instead observed at negative incidence, even at the lowest tested value of -20°.

Acknowledgment

It's been more than 3 years and still, I cannot believe how fast could life pass, but does life speed up as you get older?

Moving to another country is not really easy, especially if you are changing your major and if you don't know even the language! As a graduate chemical engineer, it was hard to get used to the new environment here in Italy and studying/working in a turbomachinery lab. But I was very lucky! I've had the best friend next to me; my wife Sami (Samaneh Rouina), who is going to graduate with me. I have to thank you for all your help and support. As a colleague, you are a genius, as a friend you are trustful and as a wife you are devoted.

Unfortunately, you cannot learn a new language or get used to a new culture by simply watching outside from your window, you have to go out. My cool Italian friends were really nice to us and help us a lot. Paolo (Epis), you were the first one that I met. Thanks for all your help and thank you for taking us around. I wish you a great life with your love, Marta. Victor (Valcarenghi) and Simone (Rinaldi) thank you for all your help and chats during the lunchtime. Mairo (Marco Miranda), the darkroom is your relic in the lab, I swear to keep it dark till I'm here. Also, thank you for PSP lessons. Ettore (Notarbartolo) and Luca (Padovan), you are still really close to us, thank you for everything. I will always remember your face when I was running the wind tunnel at high Mach number for a straight 2 hours. I have to thank your ears as well! Luca, I will not

forget the beers that we had together in the lab. I still cannot believe how you were able to get home.

During my PhD, I've learned many things from my advisors, Prof. Giovanna Barigozzi and Prof. Antonio Perdichizzi. We spend many times together dealing with different issues and problems; from the strange secondary flow pattern at +20 incidence angle to the struggle for performing TLC test on the vane. From the ghost in the lab that cut the wires during the night to the thermistor that should be 150mm but arrived 150cm! You were really kind to us and I will always be thankful. I should also thank the reviewers; Prof. Vincenzo Dossena (Politecnico di Milano) and Prof. Luca Casarsa (Università di Udine) for their useful comments, which improved the quality of this manuscript.

The next group that I would thank them are physically located 3500 Km far from me but they are always in my heart. My family in Tehran, Iran that everything that I have and achieved until now is only because of them. My mother, father, and my lovely sister. You thought me the most important lessons in the word; to be a human, to love other people and to consider the importance of education. It's hard to say how much I missed you here and how much I love you. Thank you for all your support from my childhood until now.

Contents

List of Figures

CHAPTER 1

CHAPTER 2

CHAPTER 3

CHAPTER 4

CHAPTER 5

List of Tables

Preface

The energy was, still is and definitely would be a major challenge for the human life. Nowadays, the main part of the energy delivers to the human activities are produced by turbomachines, especially gas turbines. The future of the gas turbine technology would be a more efficient cycle with an acceptable fuel to air ratio from the environmental point of view. However, the first solution to increase the cycle efficiency is to increase the inlet gas temperature, which increases the fuel consumption. Much efforts had been made throughout past decades in order to make even a small modification to the existing turbine design. For example, even 0.1% reduction in fuel consumption would draw attentions from both economical, as well as the environmental viewpoints, considering the total fuel that a gas turbine would consume during its lifetime.

In this journey, designers encounter new problems which were not an issue before, and solving them is sometimes challenging. This work is a basic research in this field and it tries to deal with a basic issue of the lean premixed combustors. These combustors are shown to be a promising technology, basically for its low NOx formation.

1

Introduction

Gas turbines are used in a very wide range of services, historically for aircraft propulsion of all types but also in land-based power generation systems and mostly at industrial plants for driving mechanical equipment such as pumps, compressors, and small electric generators in electrical utilities. Compared with the steam plants, gas turbines have shown many advantages in industrial and utility applications. They are smaller in size, weight and initial cost per unit output. They also offer flexibility in supplying process needs, such as compressed air, in addition to electric power and in using a range of liquid and gaseous fluids. However, their main disadvantage could be their low cycle efficiency, which prevents them as major base-load prime mover [1]; Therefore, developments in gas turbines and the effort to increase the turbine efficiency have been an integral part of recent studies. In this regard, increasing the turbine inlet temperature has been one of the most frequent solutions, but limitations in thermal load on metal parts inside the turbine restrict the elevation in inlet temperature. This limitation is the stresses, which are originally the temperature gradients generated in the airfoil, especially during engine start-up and shut down [2].

Overcoming this problem could be a formidable task and in general, the effort could be divided into three categories; first is the improvements in metallurgy and material science, where the vanes and blades are designed to be constructed. Nickel-based single crystal super-alloys are designed to withstand

extreme conditions of temperature and loading during operation [3]. The further discussion regarding this topic is not in the scope of this study but it has vastly discussed and expanded in the literature. Second, the use of gas turbine in combined cycles is another scheme to overcome their present low cycle efficiency for utility base-load use, while at the same time offering the utilities the gas turbine advantages, such as quick starting and flexible operation over a wide range of loads [1].

The last approach is the cooling technology, which is being studied in this work. According to Fig. 1.1, advanced gas turbine engines operate at high temperatures (1300~1700°c) to improve thermal efficiency and power output. To have a better understanding of the profound effect of inlet turbine temperature on turbine efficiency, Fig. 1.2 shows the specific core power production plotted as a function of turbine inlet temperature in different engines. As one can notice, engines tend to track fairly close to the ideal performance line, which represents a cycle power output with 100% efficiency turbines with no leakage or cooling flow [6]. Apparently, increasing the inlet temperature gives a better performance; however, according to Fig. 1.1 these temperatures are far higher than maximum allowable metal temperature; therefore, turbine blades need to be cooled. In future aircraft gas turbines to have a double power, the turbine inlet temperature must be increased from today's 1500°C to 1900°C using the same amount of cooling air (3~5% of compressor bleeding air), with an increase in compressor pressure ratio from today's 35 to around 40 or even higher. This means that in future gas turbines would have significantly higher inlet turbine temperature with the same amount of cooling air from high-pressure compressor bleed.

To achieve this, high-temperature material development together with highly advanced cooling technologies are two important issues to be addressed to ensure high performance, high power gas turbine for the next century [6]. A very famous example of this effort could be Pratt & Whitney's F117 turbofan

(Fig. 1.3) which all R&D activities are aimed at doubling the capability of turbine engines through improving the cooling effectiveness, using high temperature materials with Thermal Barrier Coating (TBC) and increasing the flow path efficiency with reducing leakage.

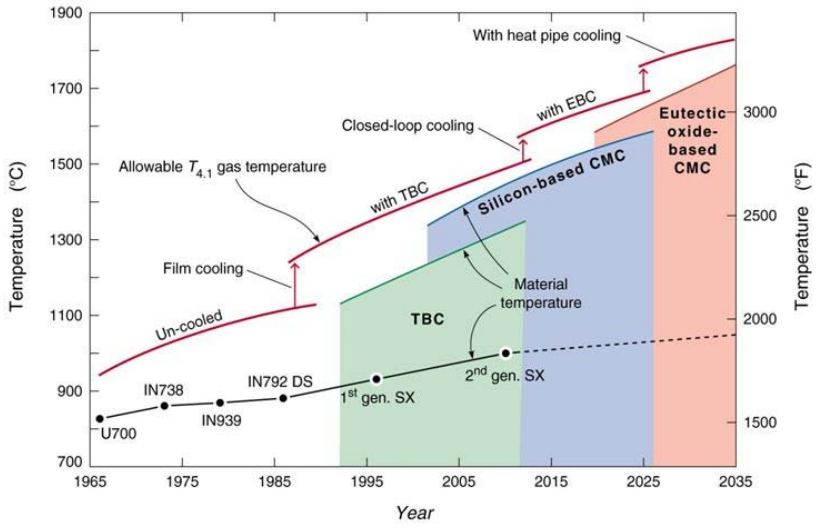

Fig. 1.1- The past and future (predicted) evolution of materials, coatings, cooling concepts and turbine inlet temperature, courtesy of Wadley Research Group, University of Virginia

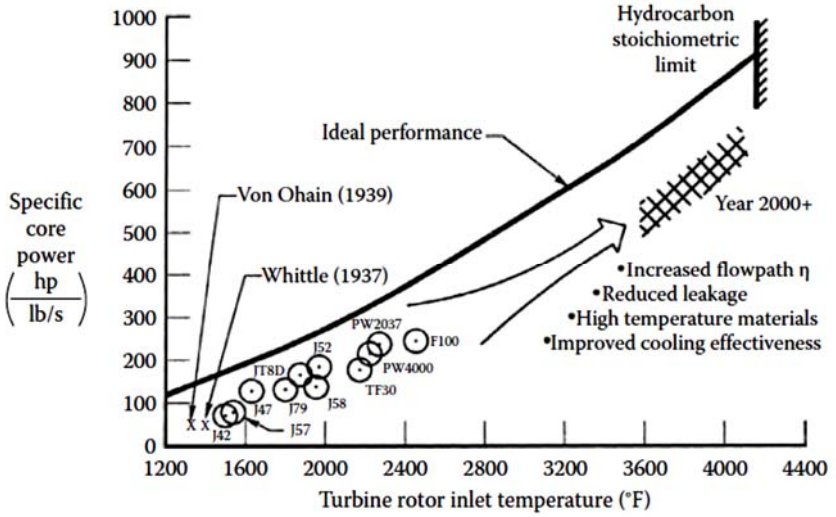

Fig. 1.2- Increasing inlet temperature dramatically improves cycle power output; Sautner et al. [5] (courtesy of Pratt &Whitney)

1.1. Thermodynamics Review

The first law of thermodynamics is the law of *conservation of energy*, which states that energy can neither be created nor destroyed. The energy of a system undergoing change (process) can be increased or decreased by exchange with surroundings and converted from one form to another within that system, but it does not indicate whether conversion of energy from one form to another is or not performed perfectly or whether some forms may be completely converted to others. Such limitations are left to the second law. A general form of the first law can be discussed through a *steady-state open system*, where mass and energy flows across the boundaries do not vary with the time and the mass remains constant within the system. This system is schematically shown in Fig. 1.4 and the first law for that system (applicable for mechanical energy; i.e. ignoring electrical, magnetic, chemical and other effects) could be written as:

$$PE_1 + KE_1 + IE_1 + FE_1 + \Delta Q = PE_2 + KE_2 + IE_2 + FE_2 + \Delta W_{sf} \tag{1-1a}$$

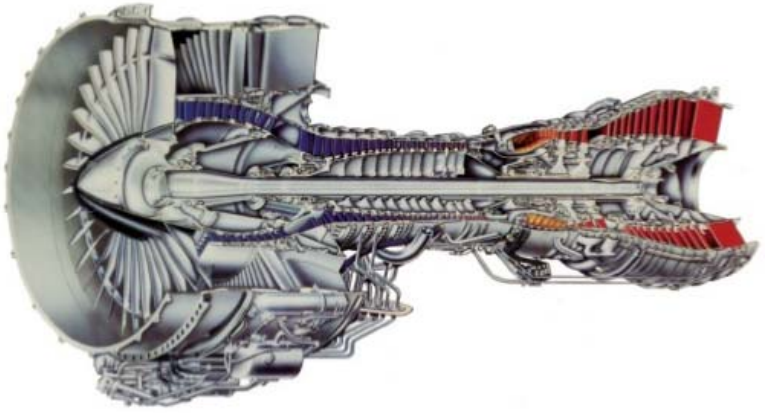

Fig. 1.3- F117 turbofan engine developed by Pratt & Whitney (courtesy of Pratt & Whitney)

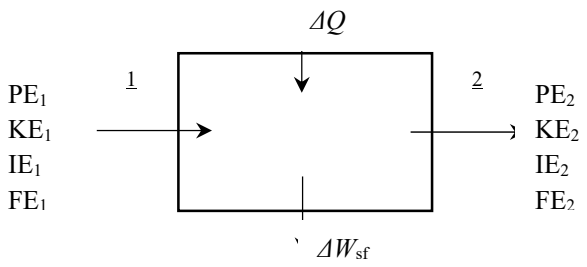

Fig. 1.4- Schematic of a steady-state open system with one inlet and one outlet

Where the subscripts 1 and 2 indicate the inlet and exit stations of the open system, *PE* is the potential energy, *KE* is the kinetic energy, *IE* is the internal energy, *FE* is the flow energy and they are described as below equations:

$$PE_1 = mz\frac{g}{g_c} \tag{1-2}$$

m is the mass of a quantity of matter or fluid entering and leaving the system, *z* is the elevation of the stations *1* and *2* above a common datum, *g* is the gravitational acceleration and g_c is the conversion factor numerically equal to 32.2 $lb_m \,.\, ft/(lb_f \,.\, s^2)$ and is 1 in metric system ($1.0\ kg.\ m/(N\,.\,s^2)$)

$$KE_1 = m\frac{V_s^2}{2g_c} \tag{1-3}$$

where V_s is the velocity of the mass at 1 and 2.

$$IE = internal\ energy = U \tag{1-4}$$

Internal energy is a measure of the internal (molecular) activity and interaction of the fluid, which is a sole function of temperature for perfect gases; while for non-perfect gases it is also a weak function of pressure

$$FE = PV = Pmv \tag{1-5}$$

Flow energy, or flow work, is the work done by the external fluid to push the quantity represented by mass *m* into, and out of the system. Mathematically it is equal to the product of pressure P and volume V.

$$\Delta Q = net\ heat\ added = Q_A - |Q_R| = mC_n(T_2 - T_1) \tag{1-6}$$

where Q_A is heat added to (entering) and Q_R is the heat rejected by (leaving) the system across its boundaries. Entering heat is normally considered as positive and the leaving heat is negative. C_n is a specific heat that depends on the process which the system takes from 1 to 2. Values for C_n in the various process are given in Table 1.1.

$$\Delta W_{sf} = \text{net steady-flow mechanical work done by the system}$$
$$= W_{sys} - W_{surr} = -\int_1^2 V\ dP \tag{1-7}$$

where W_{sys} is the work done by the system (considered as positive)and W_{surr} is the work that is done on the system by the surrounding (considered as a negative work). The integral equation requires a relationship between V and P. The most general form of equation could be $V^n = cnst.$, where *n* is called *polytropic exponent* and varies from zero to infinity and its value is given in Table 1.1 for some processes.

Equation (1-1*a*) may now be written for mass *m* entering and leaving the system as eq. (1-1*b*) and may be written for a unit mass as eq. (1-1*c*):

$$mz_1\frac{g}{g_c} + m\frac{V_{s1}^2}{2g_c} + U_1 + P_1V_1 + \Delta Q$$
$$= mz_2\frac{g}{g_c} + m\frac{V_{s2}^2}{2g_c} + U_2 + P_2V_2 + \Delta W_{sf} \tag{1-1b}$$

$$z_1\frac{g}{g_c}+\frac{V_{s1}^2}{2g_c}+u_1+P_1v_1+\Delta q=z_2\frac{g}{g_c}+\frac{V_{s2}^2}{2g_c}+u_2+P_2v_2+\Delta w_{sf} \tag{1-1c}$$

The sums $U+PV$ and $u+Pv$ are frequently used in thermodynamics and is the *enthalpy* (H or h). Enthalpy and internal energy are properties of the fluid, which means that they would have single values at any given state of the fluid. They are defined as C_v and C_p, specific heats at constant pressure and volume, respectively:

$$C_v\equiv\left(\frac{\partial u}{\partial T}\right)_v \quad ,C_p\equiv\left(\frac{\partial h}{\partial T}\right)_p, \quad C_p-C_v=R \tag{1-8}$$

where R is the gas constant.

Whereas the first law of thermodynamics declares that all forms of energy are convertible to one another, the second low puts a limitation on the conversion of some forms of energy to another. We are most concerned with two forms, heat and work. Work is the more valuable commodity and it can be completely and continuously converted to heat; however, the opposite is not true. In other word, the thermal efficiency of continuously converting heat to work, in a heat engine, must be less than 100 percent. The concepts of *reversibility* and *entropy* are introduced within the second law of thermodynamics.

Table 1.1- Values for C_n and n for various processes

Process	C_n	n
Constant pressure	C_p	*0*
Constant temperature	∞	*1*
Adiabatic reversible	*0*	$\gamma=\frac{C_p}{C_v}$
Constant volume	C_v	∞
Polytropic	$C_v\frac{\gamma-n}{1-n}$	$0-\infty$

Reversibility applies to processes and a cycle can be reversible, but only if all its processes are reversible. One irreversible process in a cycle renders the whole cycle irreversible. A reversible process also called an ideal process, is one which can reverse itself exactly by following the same path taken in the first place and thus restore to the system or surroundings the same heat and work previously exchanged. It goes without saying that there are no ideal, and therefore no reversible processes exists in real condition. Real processes are *irreversible*, although the degree of reversibility varies between processes. The main sources of irreversibility are *friction*, *heat transfer*, *throttling,* and *mixing*.

Entropy is a property, as are temperature or pressure, which remains constant in an adiabatic reversible process. In the modern context, the formulation of entropy is fundamental for understanding thermodynamic aspects of self-organization, the evolution of order and life that we see in Nature. When a system is isolated, energy increase will be zero. In this case, the entropy of the system will continue to increase due to irreversible processes and reach the maximum possible value, which is the state of thermodynamic equilibrium. In the state of equilibrium, all irreversible processes cease. When a system begins to exchange entropy with the exterior then, in general, it is driven away from equilibrium, and the entropy producing irreversible processes begins to operate. The exchange of entropy is due to exchange of heat and matter. The entropy flowing out of an adiabatic system is always larger than the entropy flowing into the system, the difference arising due to entropy produced by irreversible processes within the system [7].

According to the eq. 1-7, the non-flow work is, graphically, the area under the process when plotted on a *P-V* diagram. Heat is also an important energy term in energy systems, so we can invent the same equation like eq. 1-7, but for the heat and strictly for a reversible process and the area under process 1-2 on the T-S diagram (Fig. 1.5) equals ΔQ:

$$\Delta Q = \int_1^2 T\, ds \qquad (1\text{-}9)$$

For an adiabatic $\Delta Q = 0$ and reversible process, one can notice that $ds = 0$, since T could not be equal to zero. Therefore, an adiabatic reversible process is one of constant entropy or *isentropic* process. Considering that the gas starts at 1 with T_1 and s_1 expands adiabatically to pressure P_2, such process is represented by 1-2$_s$.

If such process goes under an irreversible process, the temperature of the gas leaving in P_2 is beyond that for the adiabatic reversible process; hence $T_2 > T_{2s}$. A more irreversible expansion results in greater self-heating of the gas and the process would be 1-2'. In other words, the greater the irreversibility, the greater the increase in entropy in an adiabatic process. If this expansion occurs in a turbine, the work obtained from the first law for the three processes cases would be $H_1 - H_{2s}$, $H_1 - H_2$ and $H_1 - H_{2\prime}$, where $H_{2\prime} > H_2 > H_{2s}$ because the gas temperature for the irreversible process is higher than the adiabatic reversible one. In sum, the adiabatic reversible turbine produces the most work; the greater the irreversibility, the less the work.

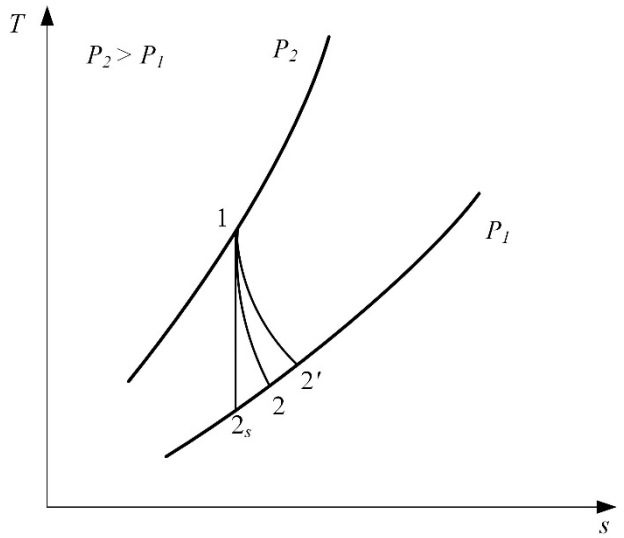

Fig. 1.5- Expansion of a gas from P_1 to P_2 on the *T-S* diagram. 1-2$_s$ adiabatic reversible, 1-2 & 1-2' adiabatic irreversible.

The degree of irreversibility is given by an expansion or turbine efficiency called the *turbine efficiency* (η_T) or isentropic or also sometimes adiabatic turbine efficiency, which is given by the following equation:

$$\eta_T = \frac{H_1 - H_2}{H_1 - H_{2s}} = \frac{h_1 - h_2}{h_1 - h_{2s}} \tag{1-10}$$

And for constant specific heats, we can rewrite the above equation as

$$\eta_T = \frac{T_1 - T_2}{T_1 - T_{2s}} \tag{1-11}$$

In case of compression from P_1 to P_2 where $P_2 > P_1$, the work absorbed in compression $|W_c|$ increases with the irreversibility. The degree of irreversibility in this case called the *compressor efficiency* (η_c) or isentropic or also sometimes adiabatic compressor efficiency, which is given by following equation:

$$\eta_c = \frac{H_{2s} - H_1}{H_2 - H_1} = \frac{h_{2s} - h_1}{h_2 - h_1} \tag{1-12}$$

And for constant specific heats, we can rewrite the above equation as

$$\eta_c = \frac{T_{2s} - T_1}{T_2 - T_1} \tag{1-13}$$

1.2. Gas-Turbine Cycles

Gas turbines are available in one-shaft or two-shaft models. The latter has two shafts that rotate at a different speed. One shaft has the compressor and a turbine that drives it, the other has the power turbine connected to the external load. Another configuration could be the following: one shaft might have high pressure sections of the compressor and the turbine, while the other has the low-pressure compressor, turbine and external load. In either case, the portion of the system containing the compressor, combustion chamber, and high-pressure

turbine is sometimes called the *gas generator*. The two-shaft configuration allows the load to be driven at variable speed, which is well suited to many industrial applications. Gas turbines designed for aircraft propulsion are sometimes modified and used for industrial service. Single-shaft turbines have the compressor, turbine, and load on one-shaft running at constant speed. This configuration is used to drive small generators for utility use. Schematics of this two configurations are shown in Fig. 1.6.

The ideal cycle for gas turbine work is the *Bryton Cycle* (Fig. 1.7). It is composed of two adiabatic-reversible (and hence isentropic) and two constant-pressure processes. The gas compressed isentropically from point 1 to 2, heated at constant pressure from 2 to 3, and then expanded isentropically through the turbine from point 3 to 4. Cooling is occurred from point 4 to 1, either in a heat exchanger or in the open atmosphere.

The work done in a turbine is equal to the rate of change in its enthalpy (when the change in gas kinetic energy is negligible). Thus,

$$\dot{W}_T = \dot{H}_3 - \dot{H}_4 = \dot{m}(h_3 - h_4) \tag{1-14}$$

where $\dot{H}$ is total enthalpy of flowing gas in *W*, *h* is the specific enthalpy in *J/kg* and $\dot{m}$ is the mass flow rate of gas in *kg/s*. This equation can be rewritten in this form

$$\dot{W}_T = \dot{m} \int_{T_4}^{T_3} C_p(T) dT \tag{1-15}$$

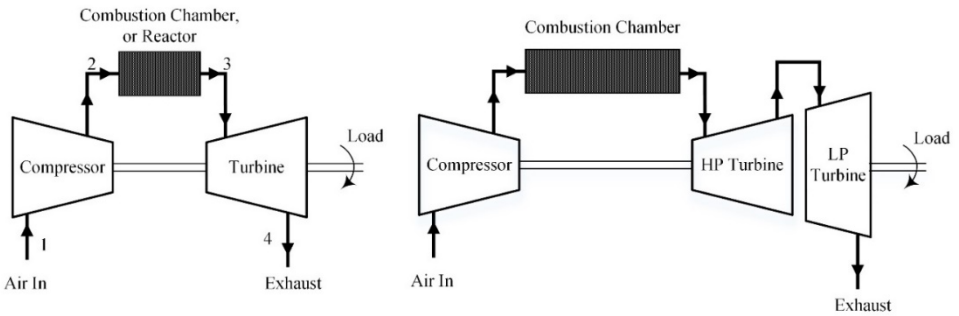

Fig. 1.6- Schematic of a single shaft and a double shaft direct open gas turbine

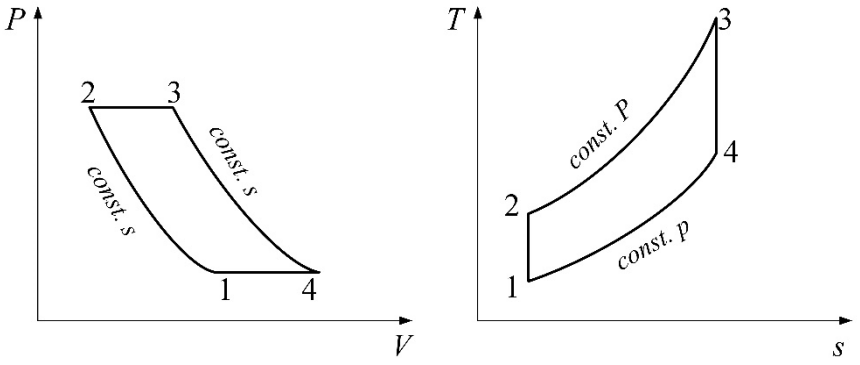

Fig. 1.7- *P-V* and *T-s* diagrams of an ideal Bryton cycle

where $C_p(T)$ is the specific heat at constant pressure of the gas, which is a function of temperature *T*. If we assume to have a constant C_p, which could be true for monatomic gases such as helium and argon, the above equation becomes

$$\dot{W}_T = \dot{m}C_p(T_3 - T_4) \tag{1-16}$$

Using the ideal gas law, we can rewrite eq. (1-16) in terms of pressure ratio across the turbine, which is related to the temperature ratio and is given by

$$\beta_{PT} = \frac{P_3}{P_4} \quad , \quad \frac{T_3}{T_4} = \beta_{PT}^{(\gamma-1)/\gamma} \tag{1-17}$$

where β_{PT} is the pressure ratio across the turbine and γ is the specific heat ratio at constant pressure and volume; hence $\gamma = {C_p}/{C_v}$. Now we can combine these equation to give the work done in the turbine as

$$\dot{W}_T = \dot{m}C_pT_3\left(1 - \frac{1}{\beta_{PT}^{(\gamma-1)/\gamma}}\right) \tag{1-18}$$

The same procedure could be applied to the compressor, where the pressure ratio across the compressor β_{Pc} is given by

$$\beta_{Pc} = \frac{P_2}{P_1} \quad , \quad \frac{T_2}{T_1} = \beta_{Pc}^{(\gamma-1)/\gamma} \tag{1-19}$$

and the absolute magnitude of the rate of work of the compressor would be given by

$$\left|\dot{W}_c\right| = \dot{m} C_p T_2 (1 - \beta_{Pc}^{(\gamma-1)/\gamma}) \tag{1-20}$$

Assuming not to have any pressure loss in the cycle, compressor and turbine pressure ratio would be equal to β_P and by this common assumption of the ideal case the net work $\dot{W}_n$ could be define as

$$\dot{W}_n = \dot{W}_T - \left|\dot{W}_c\right| = \left[\dot{m} C_p (T_3 - T_2)\right] \left(1 - \frac{1}{\beta_P^{(\gamma-1)/\gamma}}\right) \tag{1-21}$$

The right-hand side of this equation is obviously the heat added to the cycle $\dot{Q}_A$, while the second expression is the cycle thermal efficiency η_{th}

$$\eta_{th} = 1 - \frac{1}{\beta_P^{(\gamma-1)/\gamma}} \tag{1-22}$$

For an ideal cycle, the thermal efficiency of the cycle is a sole function of β_P and it is independent of inlet or maximum cycle temperature, which is not true for the non-ideal cycles. However, the optimum pressure ratio for ideal cycles could be derived by differentiating the net work equation with respect to β_P and then equating the derivative to zero. This gives us the following set of eq. (1-23):

$$T_2 = (T_1 T_3)^{1/2} \quad , \quad (T_2 = T_4)_{opt} \quad , \quad \beta_{Popt} = \left(\frac{T_2}{T_1}\right)^{\gamma/(\gamma-1)} = \left(\frac{T_3}{T_1}\right)^{\gamma/2(\gamma-1)} \tag{1-23}$$

Nonideal cycles, on the other hand, work with nonideal or real fluids, which show friction during the process. The compression and expansion processed with fluid friction can be assigned *adiabatic* or *isentropic efficiencies*, as follows:

$$\eta_c = \text{compressor polytropic efficiency} = \frac{ideal\ work}{actual\ work} = \frac{h_{2s} - h_1}{h_2 - h_1},$$

$$\text{for constant specific heat} = \frac{T_{2s} - T_1}{T_2 - T_1}$$

and $$\eta_T = \text{Turbine polytropic efficiency} = \frac{actual\ work}{ideal\ work} = \frac{h_3 - h_4}{h_3 - h_{4s}},$$

$$\text{for constant specific heat} = \frac{T_3 - T_4}{T_3 - T_{4s}} \tag{1-24}$$

using the above equations and considering constant specific heats, the net power of the cycle in terms of initial temperature T_1, a chosen metallurgical limit T_3 and the compressor and turbine efficiencies could be:

$$\dot{W}_n = \dot{m} C_p T_1 \left[\left(\eta_T \frac{T_3}{T_1} - \frac{\beta_P^{(\gamma-1)/\gamma}}{\eta_c}\right)\left(1 - \frac{1}{\beta_P^{(\gamma-1)/\gamma}}\right)\right] \tag{1-25}$$

The heat added to the cycle, Q_A is given by

$$\dot{Q}_A = \dot{m} C_p (T_3 - T_2) = \dot{m} C_p \left[(T_3 - T_1) - \left(T_1 \frac{\beta_P^{(\gamma-1)/\gamma} - 1}{\eta_c}\right)\right] \tag{1-26}$$

The efficiency of the non-ideal Bryton cycle can be then obtained by dividing eq. (1-24) by eq. (1-25). Although the efficiency of the ideal cycle is independent of cycle temperatures, except as they may affect γ, the efficiency for the non-ideal cycle is very much a function of the cycle temperatures T_1 and T_3. The two optimum pressure ratios, for specific power and for efficiency, are not the same, and this necessitates a compromise in design. Another effect of non-ideality is fluid friction in heat exchangers, piping, etc. which results in a pressure drop. In other words the pressure ratio across the compressor β_{Pc} would be greater than the pressure ratio across the turbine β_{PT}.

Other non-idealities could be from mechanical losses in bearings friction and auxiliaries, heat losses from combustion chambers, and also from air bypass to cool the turbine blades, which were not taken into account in the above calculations. In fact, these calculations nonetheless do not take into account some of the complications of a real powerplant and are hence on the optimistic side.

1.3. Turbine Cooling Technology

1.3.1. Concepts of Turbine Blade Cooling

Advanced gas turbine engines operate at high temperatures (1300~1500°C) to improve thermal efficiency and power output. As the turbine inlet temperature increases, the heat transferred to the turbine blades also increases. The level and variation in the temperature within the blade material (which causes thermal stresses) must be limited to achieve reasonable durability goals.

The operating temperatures are far above the permissible metal temperatures. Therefore, there is a need to cool the blades for safe operation. The blades are cooled by extracted air from the compressor of the engine. Since this extraction incurs a penalty to the thermal efficiency, it is necessary to

understand and optimize the cooling technique, operating conditions, and turbine blade geometry. Gas turbine blades are cooled internally and externally. Internal cooling is achieved by passing the coolant through several enhanced serpentine passages inside the blades and extracting the heat from the outside of the blades. Both jet impingement and pin~ fin cooling are also used as a method of internal cooling. External cooling is also called film cooling. Internal coolant air is ejected out through discrete holes or slots to provide a coolant film to protect the outside surface of the blade from hot combustion gases.

The engine cooling system must be designed to ensure that the maximum blade surface temperatures and temperature gradients during operation are compatible with the maximum blade thermal stress. Too little coolant flow results in hotter blade temperatures and reduced component life. Similarly, too much coolant flow results in reduced engine performance. The engine cooling system must be designed to minimize the use of compressor bleed air for cooling purposes to achieve maximum benefits of the high inlet gas temperature.

Highly sophisticated cooling techniques in advanced gas turbine engines include film cooling, impingement cooling, and augmented convective cooling. Fig. 1.8 shows the first stage high-pressure nozzle guide vane (NGV) for the GE CF6 turbofan engine. The cooling air comes from the 14^{th} stage compressor bleed and impinges on the inner walls of the NGV. After impingement cooling, the spent air provides film cooling through the leading edge holes, gill holes, midchord holes, and trailing edge slots. Fig. 1.9 shows the first stage internal cooled high-pressure turbine rotor blade for a GE CF6 turbofan engine. The cooling system is based on the use of convective cooling in the leading edge region and film cooling through the gill holes, augmented convective cooling with rib turbulators in the midchord region, and squealer tip-cap cooling and augmented convective cooling with pin fins in combination with film cooling

at the trailing edge. The optimum combination of these cooling techniques to meet the highly complex design requirements is the key to design air-cooled turbine blades and vanes.

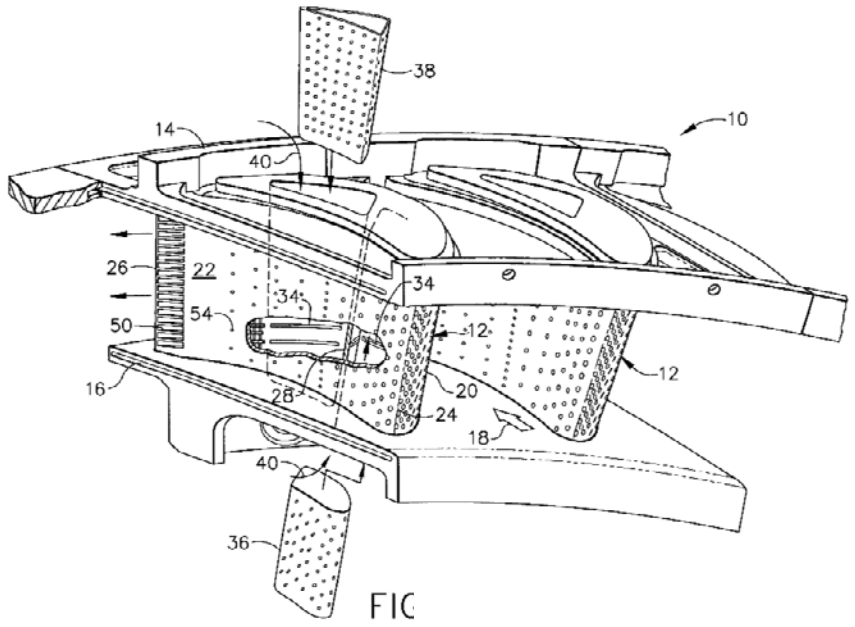

Fig. 1.8- First stage high pressure turbine nozzle vane for the GE CF6 engine [9].

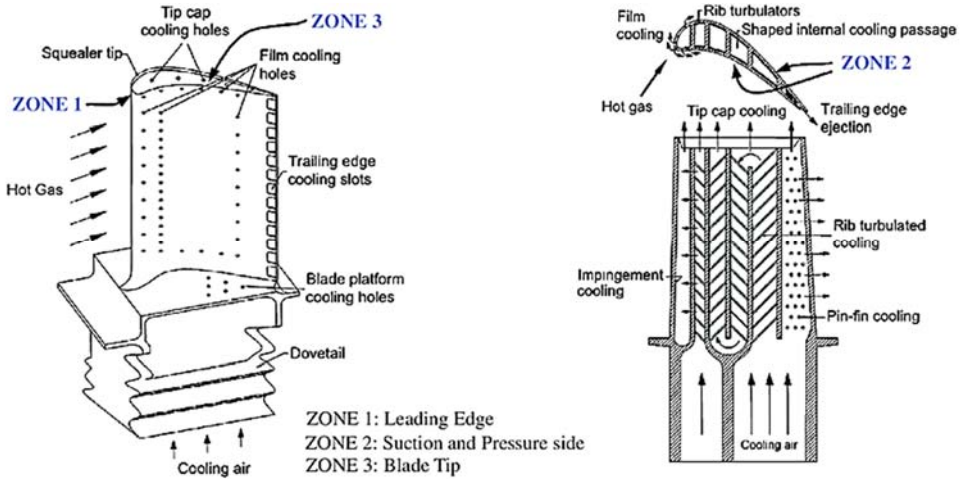

Fig. 1.9- High pressure turbine rotor blade for GE CF6 engine [8].

1.3.2. Typical Turbine Cooling System

Gas turbine-cooling technology is complex and varies from engine manufacturer to engine manufacturer. Even the same engine manufacturer uses different cooling systems for various engines. However, most cooling system designs are quite similar regardless of engine manufacturer and models. An example of such cooling system is provided in this paragraph [9]. Note that the cooling systems for today's advanced gas turbine engines have improved beyond this engine. Fig. 1.10 is an overall view of the rotor, stator, and casing cooling supply system. The first stage nozzle is cooled by air extracted from the inner and outer combustion liner cavities, and the stage-1 rotor is cooled by air extracted at the compressor diffuser midspan. The stage-2 nozzle coolant comes from the stage-7 compressor bleed, and the stage-2 rotor coolant comes from the stage-1 rotor inducer system. This design includes two separate impingement inserts and trailing-edge pressure side bleed slots. The design also uses both impingement cooling and film cooling at the nozzle leading-edge and midchord region with two rows of compound angle holes on the

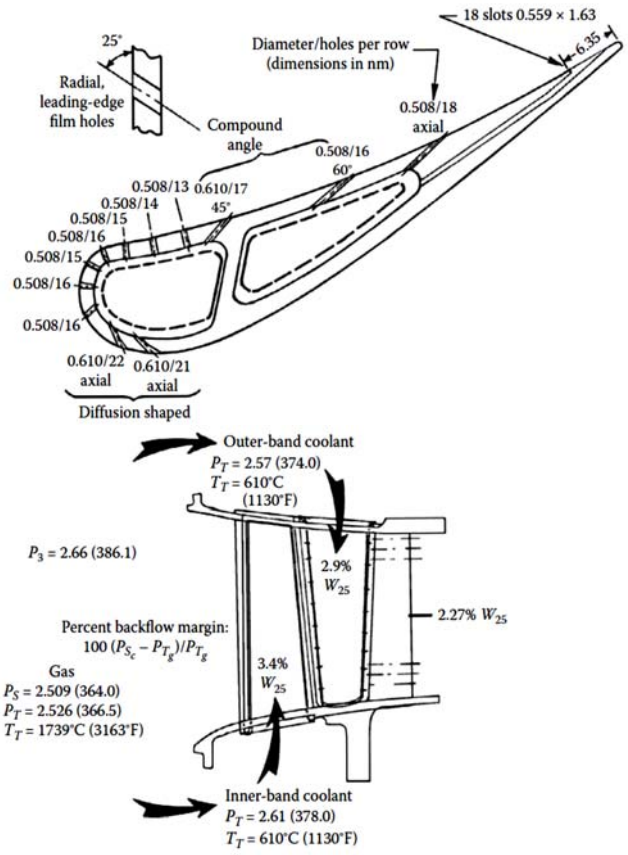

Fig. 1.10- stage-1 high pressure turbine vane- cooling geometry and cooling air supply [9].

pressure side and two rows of diffusion- shaped holes on the suction side. The vane inner band or endwall is cooled by impingement, then film-cooled through shaped holes (Fig. 1.11). The vane outer band is film-cooled through diffusion-shaped holes (Fig. 1.12). The goal is to minimize the coolant consumption, maximize the cooling effect, and produce an acceptable temperature level and distribution on the vane surface, as shown in Fig. 1.13.

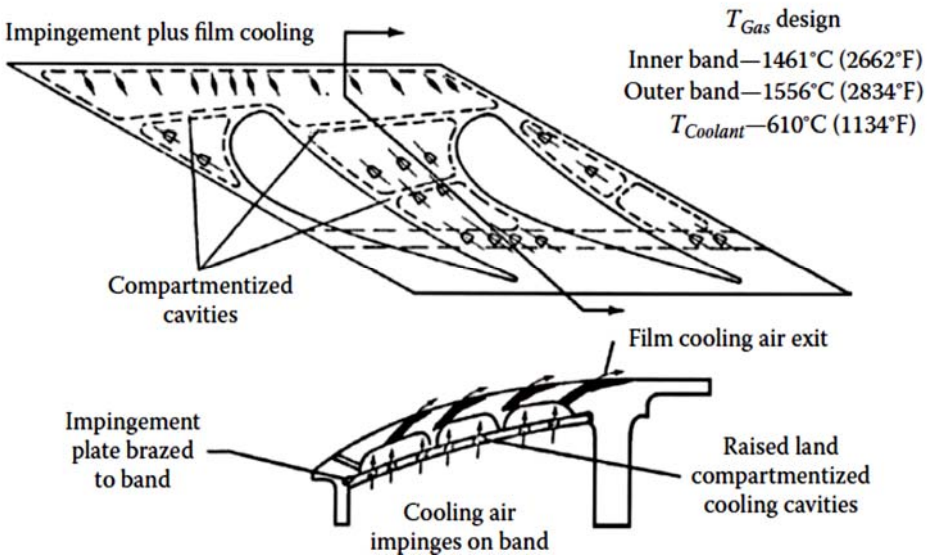

Fig. 1.11- First stage high pressure turbine vane, inner-band-cooling design [9].

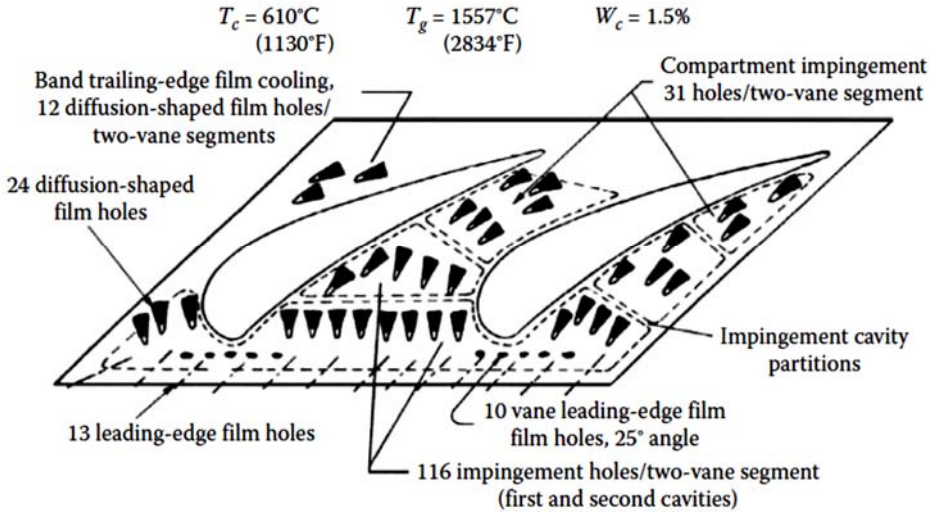

Fig. 1.12- First stage high pressure turbine vane, outer-band-cooling design [9].

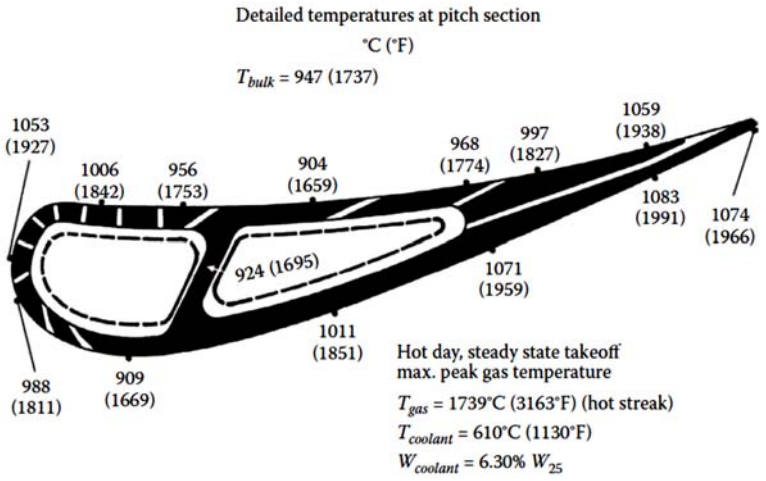

Fig. 1.13- First stage high pressure turbine vane, pitch section detailed temperature distribution [9].

Fig. 1.14 shows the detailed cooling air supply for the stage-1 rotor blade cooling system. The stage-1 rotor blade cooling system uses a two-circuit augmented convection and film-cooling design. In the forward circuit, leading-edge impingement holes are supplied by a three-pass serpentine passage with rib turbulators. The leading edge is cooled by a combination of impingement and film cooling through three rows of radial angle holes. A single row of round, axial angle holes provides the pressure side film-cooling air. The second circuit has a three-pass forward -flowing serpentine passage with rib turbulators. This second loop also provides air for the trailing-edge impinged pin film-cooling design. Trailing-edge cooling air exits through the pressure side bleed slots and produces external film cooling for the remainder of the trailing edge. The third pass of the second loop exits through a single row of pressure side, midchord, compound angle holes for reinforcing the pressure side film cooling from the upstream gill holes. Fig. 1.15 shows the first stage rotor blade-tip-cap cooling design. The tip-cap and squealer-tip cooling are achieved by bleeding a small portion of the cooling air through holes in the tip-cap region. The goal is to minimize the coolant consumption, maximize the cooling

effect, and produce an acceptable temperature level and distribution on the rotor blade surface.

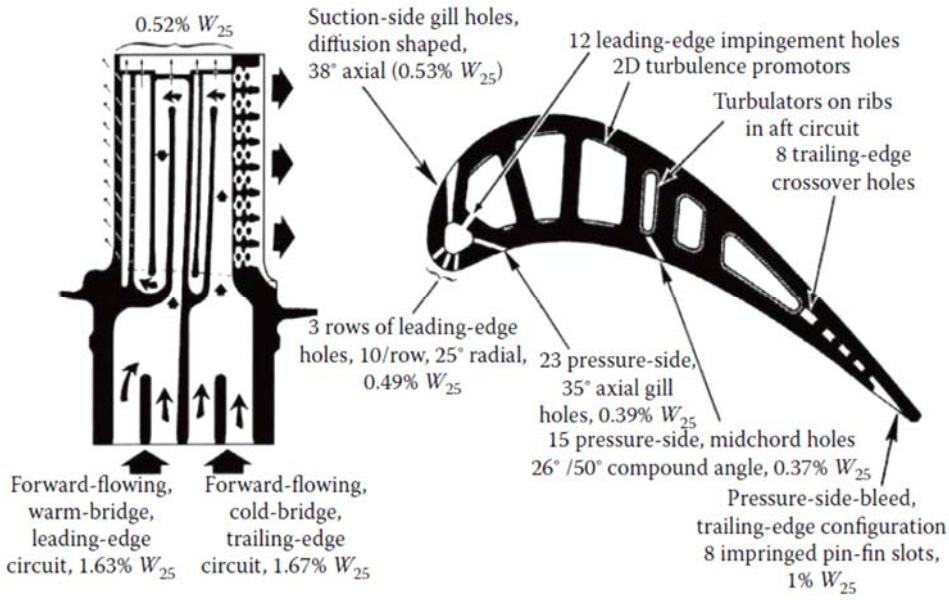

Fig. 1.14- First stage high pressure turbine rotor blade cooling system- [9].

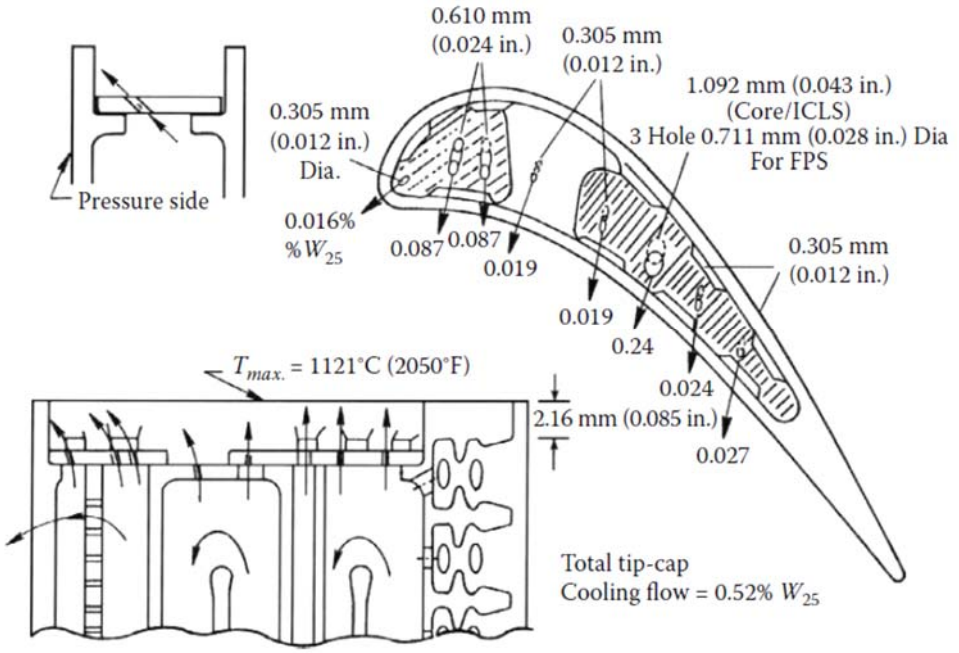

Fig. 1.15- First stage rotor blade-tip-cap cooling design- [9].

1.3.3. Turbine Vane and Blade Heat Transfer

Different cooling techniques such as augmented internal cooling and external film cooling is being used to maintain acceptable life and operational requirements under extreme heat load conditions inside modern turbines. To design a system that most efficiently cools the turbine hot-gas flowpath components, it is necessary to better comprehend the detailed hot-gas flow physics within the turbine itself. There is a great need to increase the understanding of heat transfer within this unsteady high-turbulence and highly 3-D complex flow field. It should be noted that it is critical to predict accurately the local-heat-transfer coefficient as well as the local blade temperature in order to prevent local hot spots and increase turbine blade life. Current turbine designs are characterized by an inability to predict accurately heat-transfer coefficient distributions under turbomachinery flow conditions. This results in a non-optimized design using inordinate amounts of cooling air, which ultimately causes significant penalties to the cycle in terms of thrust and specific fuel consumption.

Hot-gas path components include turbine stator vanes and turbine rotor blades. *Turbine first-stage vanes are exposed to high-temperature, high turbulence hot gases from the exit of the combustor. It is important to determine the heat load distributions on the first-stage vanes and their endwalls under engine flow Reynolds and Mach numbers for a typical gas turbine engine.* An accurate estimate of the heat-transfer distributions can help in designing an efficient cooling system and prevent local hot-spot overheating. For this reason, we have to firstly focus on the source of these heat stresses which is the combustor part of the engine. Fig. 1.16 shows both typical annular and can-annular type combustion chambers.

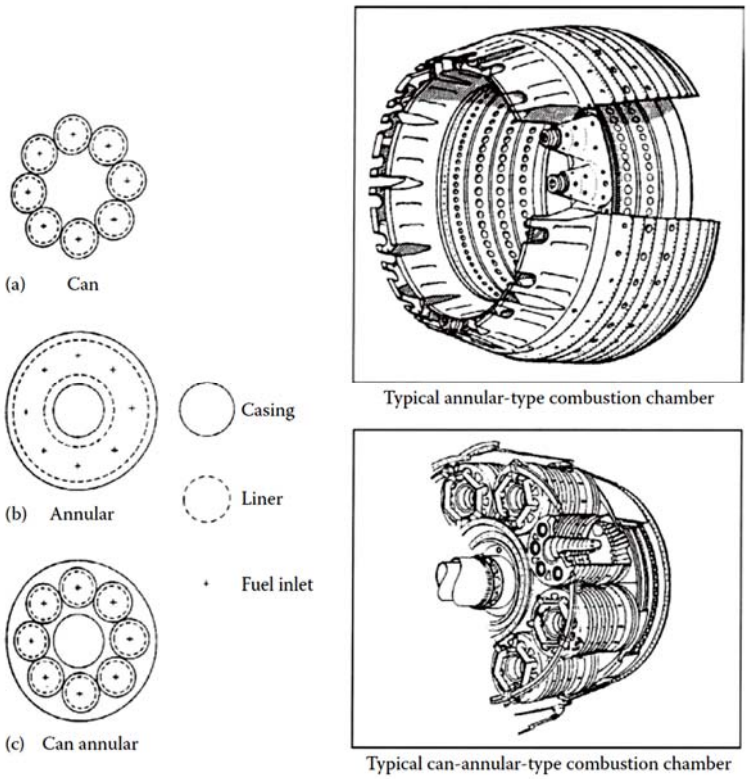

Fig. 1.16- Typical annular type and can-annular type combustion chambers and their cross-sections- [10].

In the first stage turbine stators, the inlet temperature profile and high turbulence (turbulence intensity up to 20%) affect the secondary flows produced near the endwalls, make the heat-transfer prediction even harder. After accelerating from the first-stage vanes, hot gases move into the first stage rotor blades to produce turbine power. At the inlet of the first-stage rotor blade, both the temperature and turbulence levels are lower compared to the inlet of the first-stage vane. However, the inlet velocity could be two to three times higher. Besides, the blade receives unsteady wake flows from the upstream vane trailing edge. More importantly, blade rotation causes hot gases to leak from the pressure side through a tip gap to the suction side. This often causes damage on the blade tip near the pressure side trailing-edge region. It is important to understand the complex 3-D flow physics and associated heat-

transfer distributions on the rotor blade, particularly near the tip region, under typical engine flow conditions. This can aid in designing a better cooling system and prevent blade failure due to insufficient cooling under high rotating thermal stress conditions. Fig. 1.17 shows the conceptual view of the three-dimensional (3-D) flow field inside a first-stage vane passage. The location of film holes and their cooling effectiveness is strongly influenced by the presence of these secondary flows.

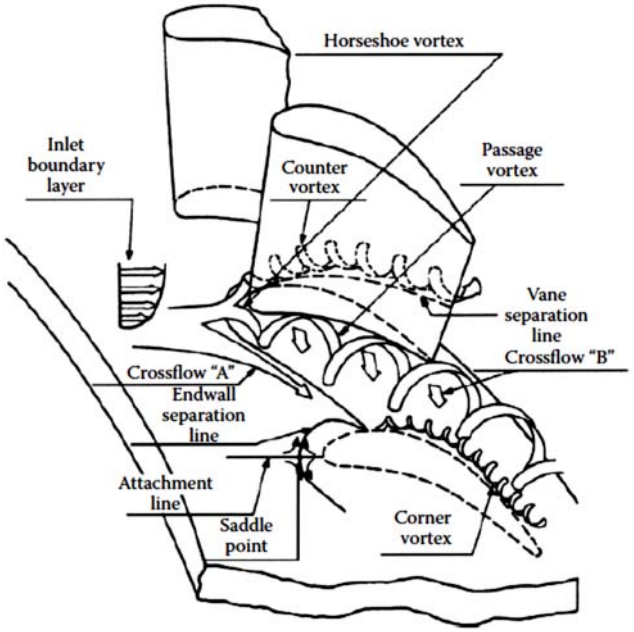

Fig. 1.17- Complex flow phenomena in a turbine rotor hot-gas passage, including secondary flows, tip flows, wakes, and rotation flows [11].

1.3.4. Film Cooling in Turbine

Cooling the turbine parts which are exposed to a high detrimental temperature flow is an evitable procedure in modern gas turbine. Different cooling schemes have been used for different turbine compartments, but film cooling normally is used when the internal cooling schemes failed to reach the desired cooling effectiveness. Film cooling is the introduction of a secondary fluid (coolant or injected fluid) at one or more discrete locations along a surface exposed to a high-temperature environment to protect that surface not only in

the immediate region of injection but also in the downstream region (Goldstein, 1971[12]).

The primary process by which film cooling reduces the heat transfer to the wall is by reducing the gas temperature near the wall, i.e. reducing the driving temperature potential for heat transfer to the wall. As the coolant flows from the coolant holes, it mixes with the mainstream gas (T_g or more common T_∞) resulting in an increase in coolant temperature to film temperature (T_f). A typical example of this is presented in Fig. 1.18 [13].

The principal film cooling parameters that concern the designers are the hole diameter D, the angle that the hole makes with the surface α, and the hole pitch P. The coolant flow ejection parameters of significance are the coolant density ρ_c velocity V_c and temperature T_c. (Fig. 1.19). T_c is the coolant temperature at the exit of the hole. The film cooling effectiveness is define as the ratio of the gas-to-film and the gas-to-coolant temperature. The coolant temperature at the wall will be at the adiabatic wall temperature, T_{aw}, and this temperature is generally assumed to be the driving temperature potential for heat transfer into the wall. Generally, the adiabatic film cooling effectiveness is define using T_{aw} as [14]:

$$\eta = \frac{T_g - T_{aw}}{T_g - T_{c,exit}} \tag{1-28}$$

Film cooling depends primarily on the coolant-to-hot-mainstream pressure ratio (P_c/P_t), temperature ratio (T_c/T_g), and the film-cooling hole location, configuration, and distribution on a film-cooled airfoil. The coolant-to mainstream pressure ratio can be related to the coolant-to-

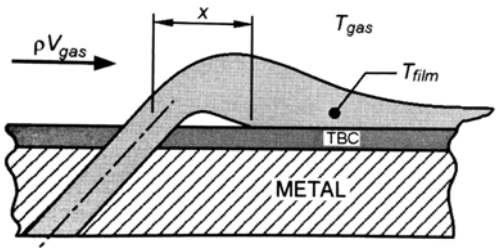

Fig. 1.18- Film cooling effectiveness [13].

mainstream mass flux ratio or the so called *Blowing Ratio*, while the coolant-to-mainstream temperature ratio can be related to the coolant-to-mainstream density ratio. In a typical gas turbine airfoil, the P_c/P_t ratios vary from 1.02 to 1.10, while the corresponding blowing ratios vary approximately from 0.5 to 2.0. Whereas the T_c/T_g values vary from 0.5 to 0.85, the corresponding density ratios vary approximately from 2.0 to 1.5. In general, the higher the pressure ratio, the better the film-cooling protection (i.e., reduced heat transfer to the airfoil) at a given temperature ratio; however, a high blowing ratio may reduce the film-cooling protection because of the jet lift-off from the surface. Therefore, it is important to optimize the amount of coolant for airfoil film cooling under engine operating conditions.

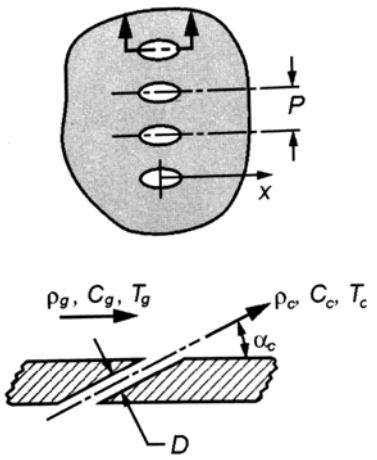

Fig. 1.19- Film cooling parameters [13].

It is also important to determine the effects of free-stream turbulence and unsteady wakes on the airfoil film-cooling performance. In addition, film-hole patterns such as film-hole location, distribution, angle, and hole geometry affect film-cooling performance. Injection of a foreign gas may trip the blade surface boundary layer into turbulence if it is laminar, or further, energize it if it is already turbulent, and so careful considerations must be given to the location of the injection holes or slots for aerodynamic as well as heat transfer and thermal reasons.

1.4. Combustor-Turbine interaction in modern Gas-Turbine

The gas turbine combustors exit flow and thermal fields govern the overall performance of the downstream turbine. Indeed, the turbine must react on whatever the flow condition exits the combustor. Therefore, a better understanding of how the combustor exit flow alters the flow development and heat transfer within the downstream turbine is needed. Today, in turbine development, to design the inlet condition of the NGV, two parameters are commonly used; the overall temperature distribution factor (OTDF) and the radial temperature distribution factor (RTDF). However, this information would not predict the real condition in which the first nozzle vanes are exposed. In fact, there exist several studies in the literature emphasizing that the temperature field exiting from the combustor is highly nonuniform and the aerodynamics and the heat loading of the turbine are actually influenced by this nonuniformity

The flow exiting from the combustor is influenced by the secondary flow effects within the stator, which will affect the temperature distribution, concerning downstream stages [40]. Also, the swirl from the combustor may additionally have an impact on the flow through the stator and succeeding stages of the turbine.

As it was indicated in the previous sections, increasing the turbine inlet temperature will enhance the Carnot cycle efficiency, but further increments in turbine inlet temperature would be achieved at the expense of more fuel consumption which is not acceptable from the environmental point of view. This, in fact, has led to a shift from conventional rich-bum combustors to lean-premixed combustors, because of the superior emission characteristics of LPM combustors. The aerodynamic behavior of fluids within LPM combustors is greatly influenced by the swirl generators (they are used to provide effective mixing due to strong shear regions and high turbulence [41,42]). The swirl flow

produced by LPM combustors then entered the turbine and interact with the first nozzle vane and leads to the aerothermal challenges for the turbine, which significantly affect heat transfer, secondary flows, and film cooling within the turbine.

As it was mentioned before, a thorough knowledge of turbine and combustor interaction is the key to the future of gas turbine industry. An important consequence of the swirled flow is the change of inlet flow incidence angle, which was not experimentally investigated on a cooled vane before. The present study is focused on this phenomenon and is trying to address all the possible issues regarding this effect. The following chapter shall give an overview of the previous research activities on combustor-turbine interaction in LPM combustors as well as the recent swirl flow investigations. The effect of incidence angle is a very new research area, thus only a few publications are available and will discuss in the next chapter.

2

Literature Survey

In the open literature, the interest over the subject of this thesis, has been raised recently since legislative requirements to lower CO_2 and NOx emissions in aero engines obliged the industry to reconsider the turbine design, specially in the combustor design. On the other hand, the need for increasing the turbine efficiency led the industry to increase the turbine inlet temperature; which means a higher fuel to air ratio and then higher NOx and CO_2 emission.

All these parameters are burdening the NOx performance of a combustion system; therefore, a new design in gas combustors is inevitable, thereby increasing the turbine inlet temperature with the same (or even less) fuel consumption. In fact, future engine cycles will be characterized by the demand for lowest fuel consumption and CO_2 emissions, resulting in highly loaded core engines with increased combustor inlet pressures, temperatures, and significant lower air-to-fuel-ratios.

Lean-premixed (pre-vaporized) combustors described by Lazik et al. [15] is identified to be the key technology to achieve the legislative CO_2 and NOx requirements. In this concept, a higher fraction of air is guided through the swirl generator to take part in the combustion reaction while the rest is injected

through the end walls for cooling purposes; therefore, peak temperatures are reduced and hence, less thermal NOx is generated. However, highly swirling flow enters the turbine for two reasons: first, a stronger swirl compared to conventional combustion chambers is generated from the beginning because of the high air ratio entering the swirl generator. Second, less air is injected radially through the end walls which could attenuate the swirling main flow [16].

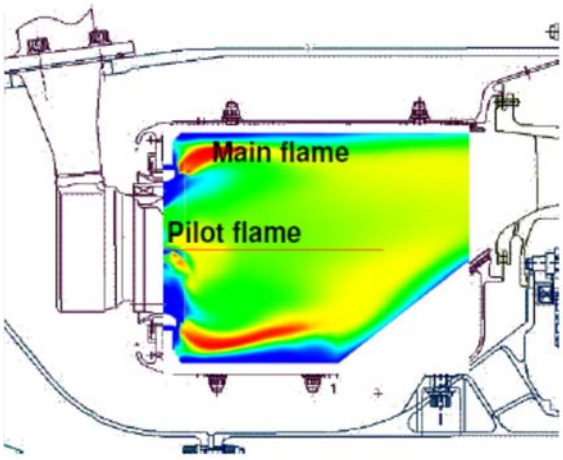

Fig. 2.1- Core engine single annular combustor configuration [15]

So, the concept consists of a single annular combustor which offers more favorable surface to volume ratio and features a reduced amount of wall cooling air (Fig. 2.1). Designing such combustor may solve the problem for NOx emissions and eventually could delivers a high-temperature inlet flow with an acceptable fuel consumption rate, however, there are consequences that should be dealt with, specially about the inlet flow behavior that contacts the first stage vanes. One can expect discrete swirl cores and hot spots which exit from this combustor. This is an important issue since the axial inflow and swirling inflow conditions have different behavior. High swirl levels are desired for the optimization of the combustion process [17], however, to maintain a predictability of the turbine flow, swirl levels in the combustor are designed to be limited. In addition, the swirl flow may cause an additional loss if it is not taken into account in turbine design; because turbine airfoils are usually optimized for an axial inflow.

In the literature, numerical and experimental investigations on swirl flow and its influence on turbine have been received much attention in these years. An initial work regarding turbine inlet swirl was numerically conducted by Turrell et al. [18]. They investigated the interaction between the high swirl flow exiting the lean premixed dry low emission (DLE) combustor of 13.4MW Cyclone gas turbine and the first nozzle guide vanes (NGV). The swirler was computed in a separate simulation, and the result was used as inlet boundary condition for the combustion chamber. The vortex causes high tangential velocities just upstream of the NGV. The vortex core contains hot gas and migrates towards the hub within the NGV passage showing an unsteady behavior in terms of location and vorticity, and as a result, a high wall temperature values was reported at the hub and on the vane suction side. The upstream impact of the NGV on the combustion process was simulated by Klapdor [19] using Rolls-Royce CFD code; in which it was shown that the effect is negligible. The model simulation is shown here in Fig. 2.2.

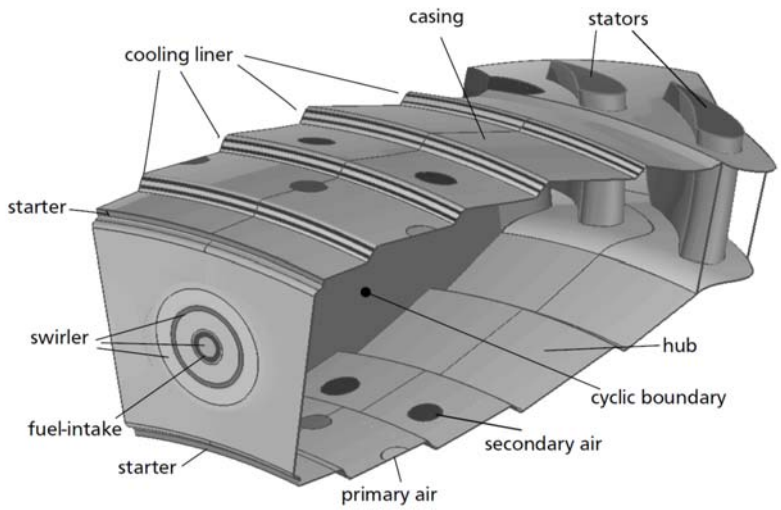

Fig. 2.2- Model of swirl interaction on first stage vane described by Klapdor [19].

At *Technische Universität Darmstadt*, Schmid et al. [16] numerically investigated the impact of swirl flow on turbine aerothermal behavior. Their setup consists of a 1 ½ stage turbine, the NGV featured endwall cooling, airfoil

film cooling, and a trailing edge slot ejection as well as the purge gap flow. A swirl generator was designed and was utilized in their simulation, according to Klinger et al. [20], to provide an inlet incidence angle as high as in real engines with lean combustion. Their results indicated that the swirl generator causes a recirculation zone inside the combustion chamber and consequently, the total pressure at turbine inlet is reduced at midspan and increased near the end walls. Moreover, they showed that incidence angles of ±15° occur at hub and casing of the NGV. Heat transfer coefficient (HTC) on the endwall with injection holes upstream of the vanes was also reported (see Fig. 2.3), showing the influence of swirl position and swirl rotation. Reduction in HTC value in positive swirl comparing to the negative one is noticed. In addition, the negative swirl gives more uniform HTC distribution between the two passages. Their study also shows a significant reduction in turbine efficiency for the swirl inflow case comparing to the axial inflow condition.

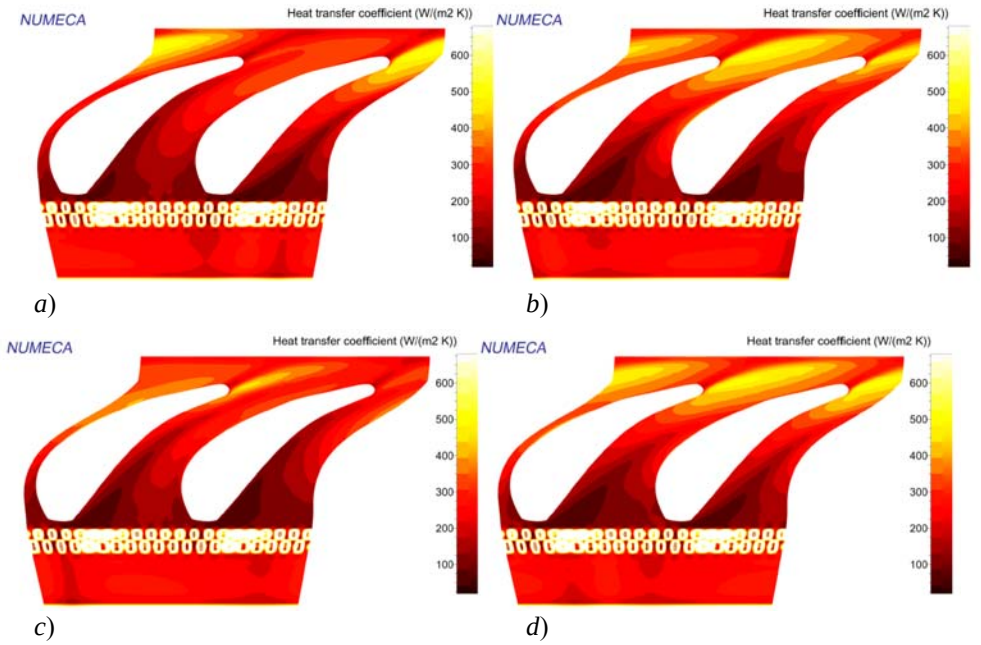

Fig. 2.3- NGV Hub HTC reported by Schmid et al. [16]; Swirl generator aligned to the *mid passage* with *a*) *positive* swirl, *b*) *negative* swirl; Swirl generator aligned to the *leading edge* with *c*) *positive* swirl, *d*) *negative* swirl

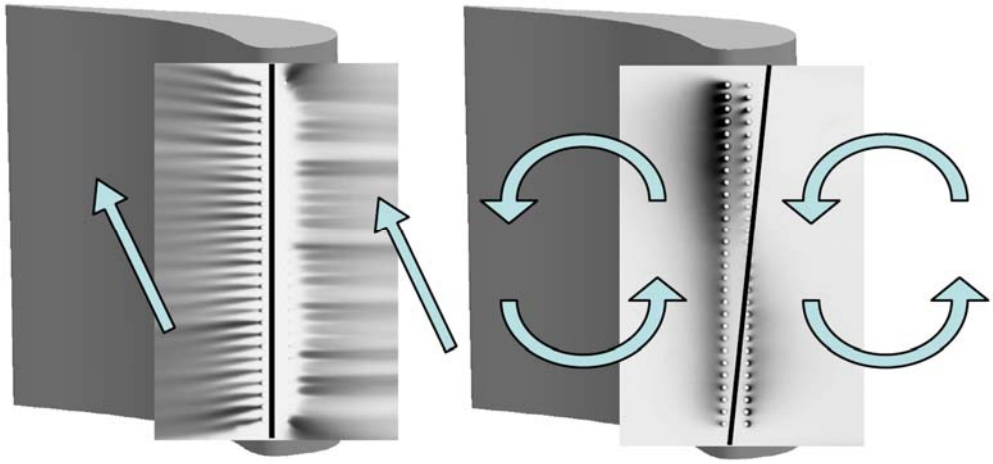

Fig. 2.4- Vane film cooling results *(ammonia diazo technique)* at axial inflow *(right)* and swirling inflow *(left)*, with simplified stagnation line; reported by *Giller and Schiffer* [22]

Qureshi et al. [21] carried out numerical and experimental investigations on inlet swirl in an annular cascade. They reported that a swirl number of 0.7 causing an incidence of ±50°, increases mixing, reduces the boundary layer thickness, augments heat transfer and deforms the stagnation line. It was also reported that the inlet swirl orientation causes positive incidence at 10% span increasing the loading there and hence, negative incidence at 90% span reducing the loading. At midspan, the low pressure area in the vortex core is ingested to the suction side which decreases the loading. Giller and Schiffer [22] investigated a linear nozzle vane cascade with upstream swirl generator in collaboration with Schmid and Schiffer [23], which were investigating the CFD simulations of the same system. Measurements show a domination of the swirl in the secondary flow field which is still visible after passing through the passages of the vanes. The pitch of a swirl generator matches one passage, causing the swirl cores to merge upstream of the leading edge; this results in a massive change of incidence angle which influences the vane load. Furthermore, because of the incidence, the stagnation lines of the vanes are tilted which results in a turnover of the cooling film to the other side of the vane at certain areas. This leads to completely uncooled areas with that injection

holes configuration (See Fig. 2.4). It was also shown that the distance between the swirler nozzles and the cascade vanes has a greater effect on the cooling film than the swirl number.

In 2015 Luque et al. [24] described their new experimental facility to investigate combustor–turbine interactions in gas turbines using multiple can combustors. Their study gives an insight into the thermal and aerodynamic effects of the outflow from a can combustor into an engine realistic geometry including cooling system and boundary conditions. Yin et al. [25] investigated the effect of inlet swirl on the downstream vane film cooling. Their results support the idea of alteration in vane leading edge stagnation line under swirling flow condition. This study was then followed by the same research group, investigating the influence of combustor inflow on vane leading edge cooling system [26]. The results showed that the multiple-swirl combustor flow field has a significant impact on the vane cooling system due to the residual swirl intensity at the combustor outlet. The stagnation line at the vane leading edge was altered compared to uniform inflow, resulting in a significant impact on leading edge film cooling effectiveness, while the pressure side film cooling system was slightly affected. The same phenomenon was reported by Insinna et al. [49, 50]. They numerically analyzed the heat transfer performance of a cooled vane, considering an exit flow filed of a reactive annular combustor simulator.

Recent research on combustor-turbine aerothermal interaction was conducted in University of Oxford by Jacobi [29], investigating the can combustor outflow into a vane cascade. Their experimental results were supported by their simulations. The study reveals the highly unsteady nature of the flow in the first vane and its effect on the heat transfer. A persistent flow structure of concentrated vorticity was also observed, which wraps around the unshielded vane's leading edge at midspan and periodically oscillates in the

spanwise direction. The reason for such behavior was found to be the interaction of the residual low-pressure swirl core and the vane's potential field. Moreover, the transient behavior of the horseshoe-vortex system due to large fluctuations in incidence was demonstrated. In another work in 2016, described by Werschnik et al. [30], a profound experimental and numerical study was done on a modified Large Scale Turbine Rig, defined by Krichbaum et al. [54]. This study includes the influence of inflow condition on heat transfer and film cooling effectiveness on the hub side endwall. It was shown that the presence of a swirling inflow, decreases the film cooling effectiveness and increases the *Nusselt* number comparing to the axial inlet flow condition. Regarding the film cooling effectiveness, a local variation was reported, which was found to be the result of local variations in the main flow dynamic pressure, located near the wall upstream of the injection holes. They stated that this local pressure variation, locally influenced the effective blowing rate for certain cooling holes, and as a consequence, lower film cooling coverage of the downstream endwall section was observed. In 2017, the same combustor-turbine fluid dynamic group at *Technische Universität Darmstadt,* numerically studied the combustor–turbine interaction on the Large Scale Turbine Rig in presence of swirl generator proposing a SST-SAS model to correctly predict the unstable flow caused by the swirl generator [53]. They also investigate the influence of combustor swirl on pressure loss and on the propagation of coolant flow [31] (see Fig. 2.5). CO_2 was used to trace the coolant flow injecting from the endwall. It was indicated by the authors that hub side endwall coolant injection influenced the pressure loss and it

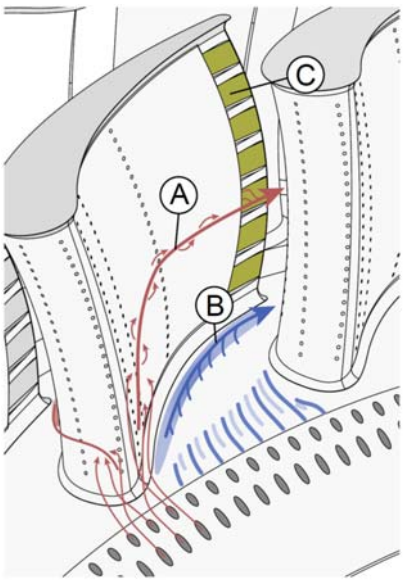

Fig. 2.5- developed flow model illustrated by *Werschnik et al.* [31]

showed an impact on trailing edge coolant slot ejection. In particular, the coolant significantly influenced the vane flow field and causes additional losses in the passage flow while reducing losses at the hub.

The importance of swirl effect on aerothermal performance of a turbine is thus undeniable. The combustor-turbine interaction must be carefully understood, from both aerodynamic and heat transfer points of view, in the design process of an HP vane cascade in presence of swirl flow at turbine inlet. Considering this fact, Shahpar et al. [27] reported an aerodynamic optimization of an NGV with high swirl caused by lean burn combustor. They propose an M-shaped NGV leading edge, suggesting that the adverse effects of the high inlet swirl can be recovered. Rosic et al. [28] numerically investigated the integrated combustor and vane concept in the gas turbines, showing benefits in terms of cooling air requirements without an adverse effect on aerodynamic performance, compared to a standard design.

The present study consists in a basic investigation on the influence of mainstream incidence on the aero-thermal performance of a film cooled nozzle vane cascade. Instead of generating a swirl in the inlet flow, discrete values of inlet flow incidence in the range of -20° to +20° have been generated and their impact on cascade performance has been experimentally studied. Incidence effects on cascade aerodynamic performance have been deeply investigated in the literature in uncooled cascades, mostly in the field of steam turbines. A thorough study which was focused only on the aerodynamics was made by Perdichizzi et al. [33] downstream of a linear turbine cascade. Their thorough study comprises testing the cascade vane in 5 different inlet flow incidence angles, ranging from -60 to +35 degrees and for various pitch-chord ratios s/c = 0.58, 0.37, 0.87 (Fig. 2.6). They observed a clear relationship between the blade loading in the first part of the blade passage and the intensity of the

secondary flows, which high levels of streamwise vorticity and intense crossflows at the endwall take place at large incidence angles and low solidities. They also reported an extreme variation in the deviation angle distribution, which the maximum overturning angle varied from zero to 15 degrees. Increasing the incidence angle and the pitch chord ratio, the region interested by secondary flows extends progressively towards the midspan. For the extreme conditions, the vortices of the two half parts of the flow channel get the midspan and interact with each other; as a consequence the overall secondary loss and the exit flow angle undergo a huge increase. Other studies [57-59] showed that a positive incidence translates into a shift of stagnation on the pressure side and into an increase in the blade front loading that in turn is responsible for the strengthening of secondary flows. Progressively increasing the incidence angle, the region interested by secondary flows extends towards the mid span with the vortices of the two half of the channel that eventually merge interacting with each other; as a consequence overall loss and exit flow angle undergo a huge increase. Conversely, negative incidence values result in a shift of stagnation on the suction side and in a front load reduction. As a consequence, secondary flows can be attenuated.

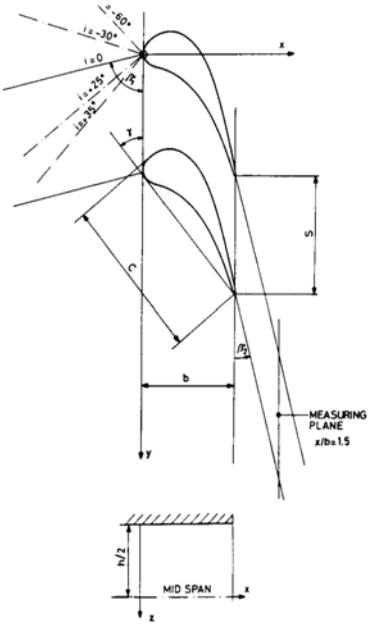

Fig. 2.6- Cascade geometry and deviation angle variation in the cascade [33].

More recently, positive incidence values have been shown to strongly influence the thermal protection over an end wall cooled through single and multiple row (Fig.2.7), as a consequence of enhanced secondary flows [60]. This general behavior is consistent with the aerodynamic impact of swirl on

cascade performance previously discussed. Unfortunately, empirical correlations like Craig and Cox [61] fail in correctly predict the impact of an incidence variation on loss generation, especially when applied to a modern, high loaded, film cooled nozzle vane cascade. Experimental data are thus necessary to have a better estimation of cooled cascade performance perturbed by swirl. However, in the literature, there seems to be no similar work (or very few work) and the subject of this thesis has not been yet introduced. A similar work was reported by Camci and Arts [32] on a cascade of transonic rotor blades. Blades were equipped with 3 rows of cylindrical holes, located on the leading edge of the blade as a showerhead cooling configuration. Different incidence angles (0°, +10° +15° and -10°) was tested to investigate the aerodynamics and heat transfer performance of the rotor cascade. They report movement in stagnation position when the incidence angle is varying from the reference angle (i = 0°). In particular, negative incidence leads to a movement in stagnation line toward the SS of the blade, and positive incidence angles instead transfer the stagnation line to PS of the rotor. They also showed the coolant split between the showerhead injection holes located on SS and PS of the blade, was strictly controlled by the position of the stagnation point at a given incidence angle. In another word, the local

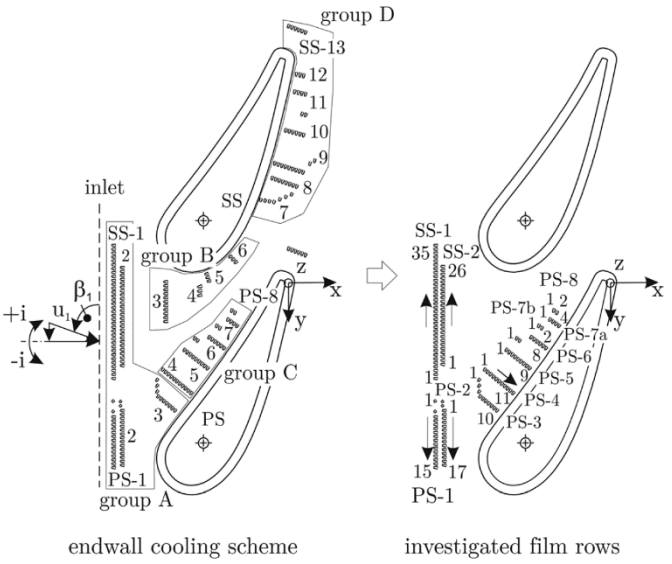

Fig. 2.7- Schematic of endwall cooling scheme reported by Kunze et al. [60]

blowing ratio for each hole was changing when the incidence angle is varying from the reference condition.

In another similar work, Perdichizzi et al. [34] investigated the aerothermal performance of a nozzle vane cascade with a generic non-uniform inlet flow. An obstruction was located at an inlet section to produce a non-uniform flow upstream of the leading edge plane. Their results showed that an inlet flow non-uniformity influences the stagnation point position when it faces the vane leading edge and a relevant increase of both 2D and secondary losses was reported. However, when it is located in between the passage it does not affect the stagnation point location, in the meanwhile allowing a reduction in the secondary loss. Fig. 2.7 shows the Tu distribution in presence of the inlet obstruction at two different tangential positions. This study was continued by Barigozzi et al. [35], investigating the effect of platform cooling.

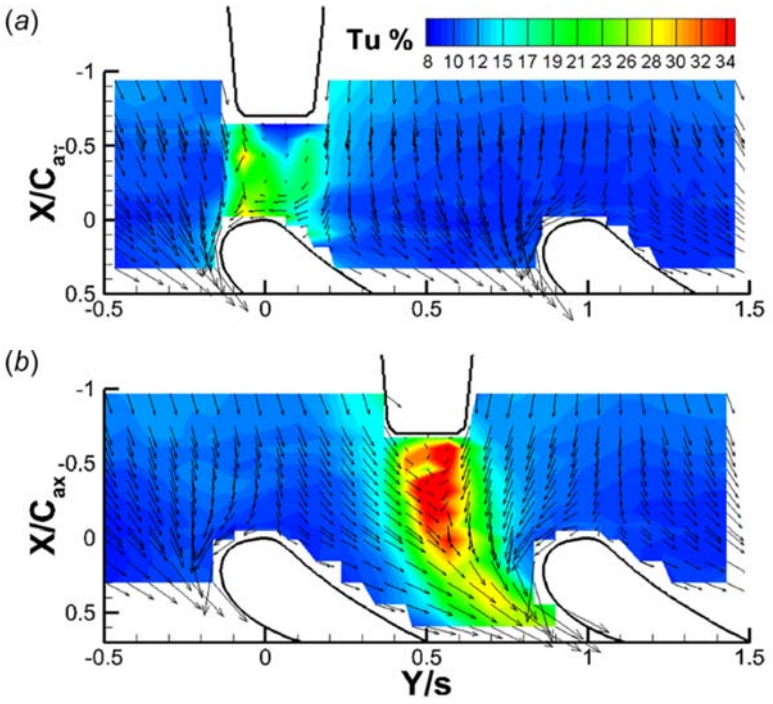

Fig. 2.7- Tu distribution for different tangential position of the obstruction reported by Perdichizzi et al. [34]

The above review, reveals the previous studies targeting the consequences of the swirl flow. Most of them use a swirl generator to replicate the swirl inside the real engine. This swirl generator was numerically modeled in advance and then experiments were perfectly executed to validate numerical simulations. A common argument among these investigations is the alteration in inlet flow incidence angle. But up to now, by author's knowledge, there is no similar work which devotes itself only to the incidence effects on aerothermal performance of the NGV.

The novelty of this research is the investigation of incidence effects on a cooled cascade in presence of slot platform cooling. Even if obtained in simplified testing condition, these findings are valuable for the design of combustor-turbine interface and allow to optimize the aero-thermal performance of the NGV, including vane and end wall cooling systems. A cascade of six high loaded vanes was designed with a geometry of a typical high pressure turbine vane in modern heavy-duty Gas Turbines. The following chapters shall illustrates the execution plan and the results obtained in this study.

3

Experimental Setup

In this chapter the experimental setup and the procedure for each set of experiments is described. Investigations for the effect of incidence angle were divided into aerodynamic and heat transfer points of view and for each part of the study, different procedures were followed.

All the tests (aerodynamic and heat transfer investigations) were done on a suction type wind tunnel available at the University of Bergamo. A fan is used to drive the air inside the test section and they are connected via a diffuser. The diffusion section partially recovers the flow kinetic energy and it allows the tunnel to reach a maximum isentropic Mach number of 0.6 at cascade exit, with an inlet turbulence intensity level of about 1.6%. The wind tunnel and its 3D model are illustrated in Fig. 3.1 and Fig. 3.2, respectively. As it's illustrated, the tunnel was entirely designed and fabricated in Plexiglas in order to have a visual access over the test section.

Fig. 3.1- Wind tunnel used in this study

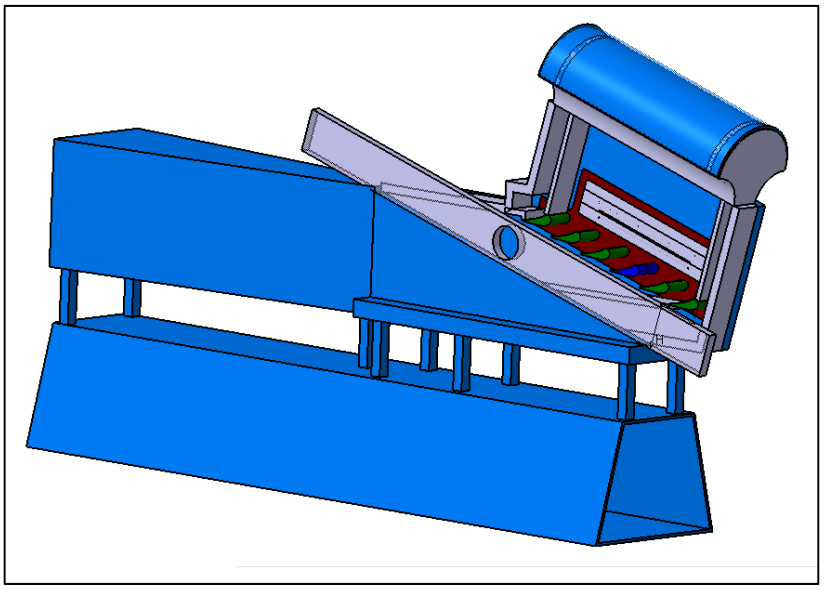

Fig. 3.2- Wind tunnel 3D model

The test section consists of a cascade of six high loaded vanes with a geometry of a typical high pressure turbine vane of a modern heavy duty gas-turbine. The vane cascade is shown in Fig. 3.3. Vanes were designed and manufactured in Plexiglas in order to have a perfect and uniform finished surface all over the vanes; in addition manufacturing in Plexiglas gives an opportunity to apply different paints for further measurements. The vane geometrical characteristics are briefly summarized in Table 3.1 and the profile of the vane is illustrated in Fig. 3.4.

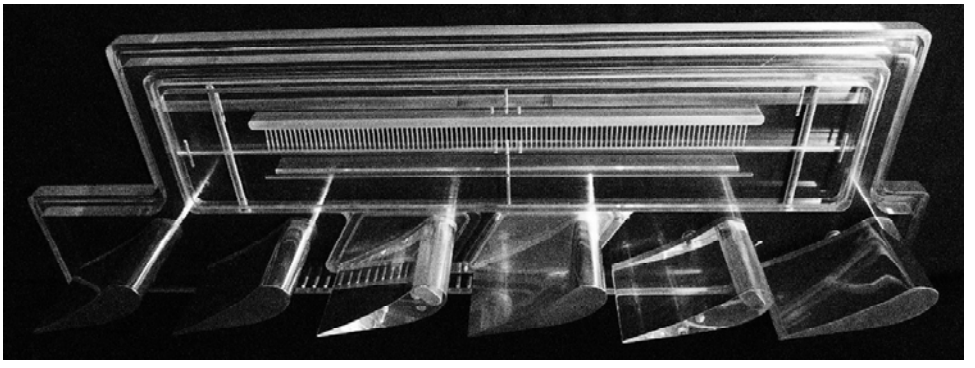

Fig. 3.3- Vane cascade of six high loaded vanes used in this investigation

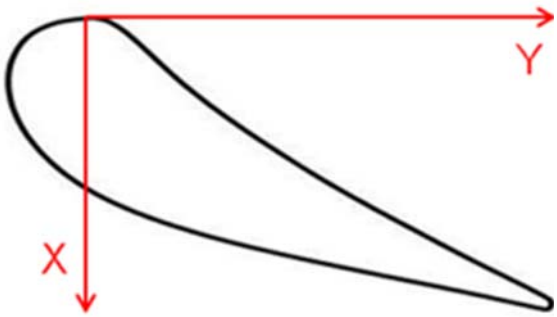

Table 3.1- Cascade geometry

s/c	1.04
H/c	0.69
Vane pitch, s	148.34 mm
Vane chord, c	142.1 mm
Inlet flow angle β	0°
Axial chord (c_{ax})	68.31 mm

Fig. 3.4- Vane profile

In order to investigate the effect of incidence, starting from 0° incidence to ±10° and ±20°, the inlet test section was modified to deliver the desired inlet flow angle at the vane leading edge. For this purpose, a pair of triangle pieces for each incidence angle were designed, manufactured and installed at the inlet section according to Fig. 3.5. T he theoretical incidence angle is being changed by introducing these new triangles and this could be done for each incidence angle (as it's shown in Fig. 3.6) in order to adjust the inclination of the two sidewalls.

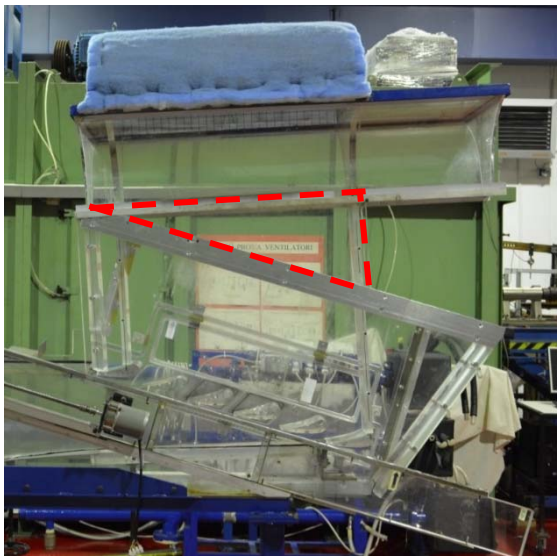

Fig. 3.5- Modified inlet section for the wind tunnel

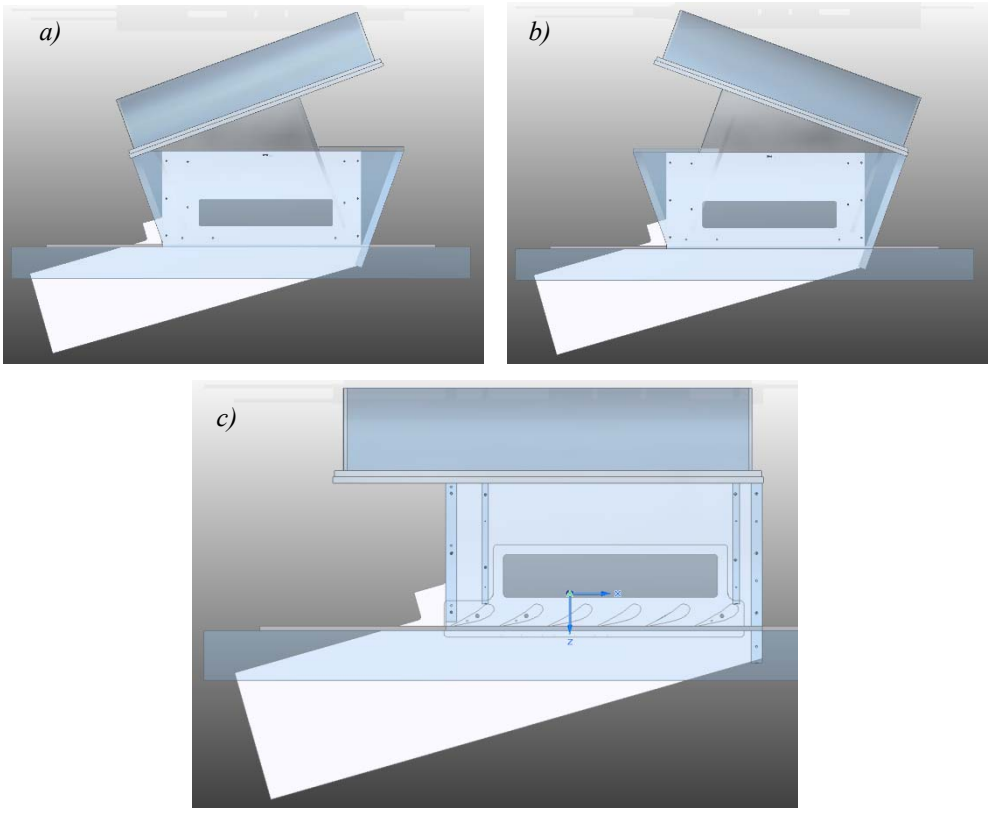

Fig. 3.6- Modified inlet section in different incidence angles, *a) +20° b) -20° and c) 0°*

A turbulence generator (Fig. 3.7) has been used in order to increase the turbulence intensity level in the inlet flow. It is located at a distance of 240mm upstream of the vane leading edge and it provides a turbulence intensity between 8 to 9% at cascade inlet, depending on the Mach number and therefore Reynolds number. Turbulence characterization was performed by means of a single wire hot wire sensor 1.6cax upstream of the leading edge plane, where also the approaching boundary layer was measured. The uniformity of the turbulence intensity along the tangential direction was verified using a 2D LDV system, which was used for characterizing the inlet flow condition at several axial distance, as well. More details could be found in Chapter 5.

Fig. 3.7- Turbulence generator

3.1. Aerodynamic Investigations

Regarding the aerodynamic investigations, different experiments were done to verify and characterize the wind tunnel setup, as well as the evaluation of cascade performance. These experiments are:

- Flow periodicity
- Vane Loading
- Inlet flow characterization
- Oil & dye visualization
- 5-hole probe investigation

Flow Periodicity:

Flow periodicity over the test cascade was verified by 31 pressure taps located downstream of the trailing edge plane. These pressure tabs are tangentially aligned to the cascade, thus they maintain a constant distance from the trailing edge plane (45% of the axial cord, c_{ax}). The isentropic Mach number distribution is hence calculated from the inlet total pressure (measured $1.6c_{ax}$ upstream of the vane leading edge plane by a 3-hole probe) and these pressure taps by acquiring static pressure distribution using a differential pressure scanner or Scanivalve. The Scanivalve is connected to the acquisition system and it was used for each test condition (i.e. each inlet flow Mach number) in order to characterize the flow conditions. Fig. 3.8 illustrates the downstream

pressure taps on the cascade, while the Scanivalve used in this study is shown in Fig. 3.9.

Fig. 3.8- Pressure taps downstream of the vane cascade

Fig. 3.9- Scanivalve

Vane Loading:

Loading on the vane was measured by using an instrumented vane, which has the exact vane profile but it was designed and manufactured in Aluminum. Fig. 3.10 illustrates the manufactured instrumented vane used in this study. The pressure taps could be noticed in this figure

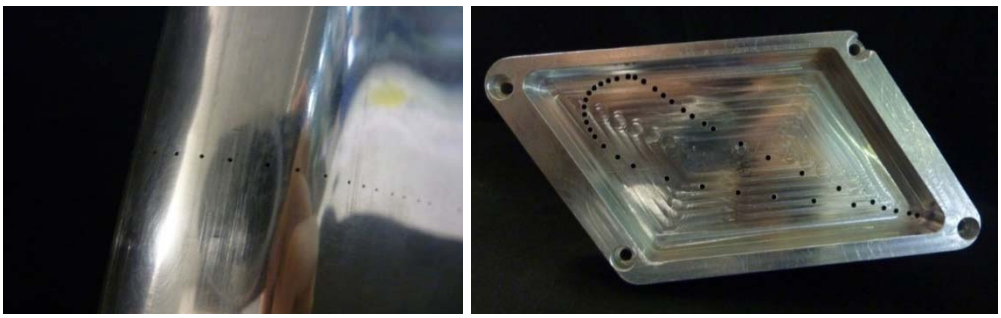

Fig. 3.10- The manufacture instrumented vane

The instrumented vane was designed with 39 pressure taps located at the midspan, 16 on the pressure side and 23 on the suction side according to Fig. 3.11, for measuring the load on the vane. Based on this figure, one could notice a closer distribution of pressure taps on the leading edge of the vane, specially on the suction side; this is due to obtain a better identification of the stagnation point.

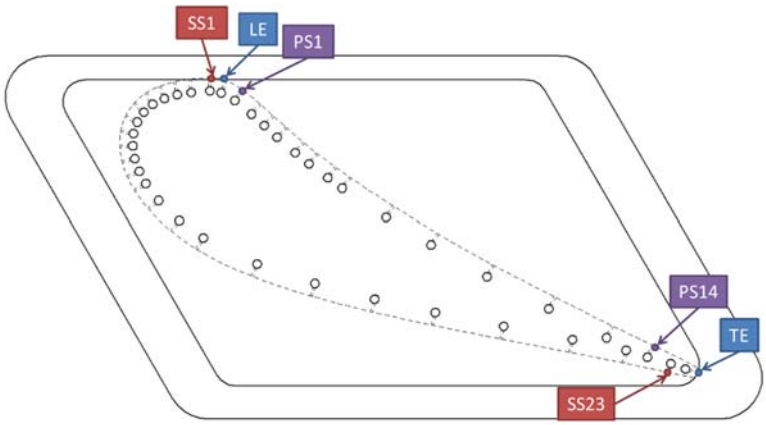

Fig. 3.11- Pressure taps orientations for the instrumented vane

Inlet flow characterization:

Inlet flow Mach number was measured using a wedge type 3 hole probe located upstream of the vane cascade (Fig. 3.12). The central hole measures total pressure of the inlet flow, while the other two holes measure the static pressure on right and left sides of the probe.

Fig. 3.12- The 3-hole probe (wedge type) used in this study

If the static pressures from two sides of the probe are not equal, the probe might not be well aligned to the main flow. For each test, the right and the left static pressures were monitored simultaneously, and the yaw angle of the probe was modified until reaching the same value for static pressures, then Mach number was controlled. The inlet flow velocity was regulated by changing the Hz of the fan, using an inverter.

The flow characteristics upstream of the vane leading edge was also investigated using the LDV technique. The probe was traversed in the tangential direction, over two vane pitches, and in different axial position from the vane leading edge plane. Thus, Mach number distribution inlet flow angle (β) and turbulence intensity level was calculated. Fig. 3.13 shows the LDV system used in this study.

Fig. 3.13- LDV system using in this research

Oil & dye surface flow visualization:

Oil and dye flow visualizations of the platform have been performed to get traces at the end wall of the 3D flow structure. The mixture of oil and dye was applied on both the vane and endwall in advance. After turning on the tunnel, oil & dye provides somewhat lasting air flow pattern on the model for photos during the test and also when the wind is off. As it can be seen in Fig. 3.14, this

technique clearly shows the flow patterns, especially the transition between laminar and turbulent flow as well as separations.

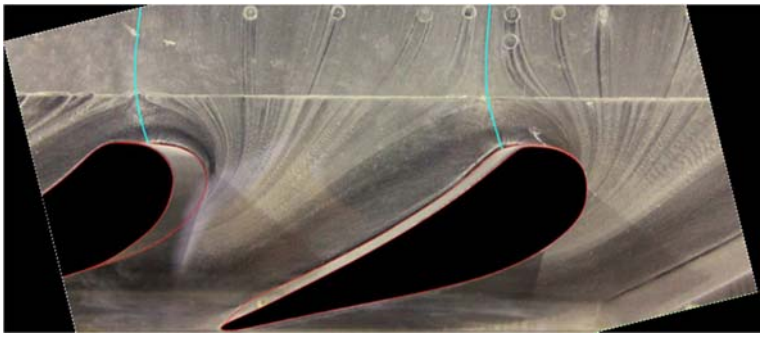

Fig. 3.14- Oil & dye visualization

5-hole probe investigation:

The 3D map of the flow at cascade exit was obtained using a miniaturized 5-hole probe shown in Fig. 3.15. The probe was traversed along the vane cascade using a traversing system. The traversing system (Fig. 3.16) was designed to move the probe in tangential, radial and angular movements and is controlled by a controlling system integrated with the acquisition system, in which different encoders were used to control and monitor the position of the probe along the cascade. During the test, the position of the probe at each step was read by the encoders and if the position of the probe was not in the acceptant range, the controlling system would correct the position. While the position was verified, pressure acquisition was then performed and thus a 3D flow field was obtained. In this research, the data were obtained by traversing the probe at a distance of $\boldsymbol{0.5c_{ax}}$ downstream of the trailing edge. The data obtained from this technique are:

- vane wake profile including Mach number distribution, exit flow angle and total pressure ratio;
- kinetic energy loss coefficient;

- secondary flow structure;
- and, vorticity distribution.

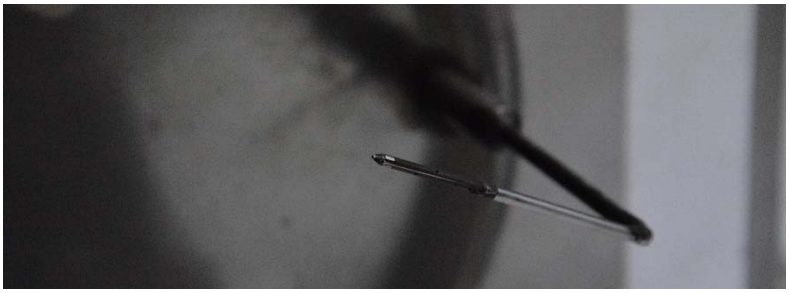

Fig. 3.15- Miniaturized 5-hole probe

Fig. 3.16- 5-hole probe traversing system

Before performing the tests, the 5-hole probe was calibrated in advance, using a calibration system shown in Fig. 3.17. The calibration system is a small-scaled wind tunnel which the air is blown into the calibration section, as the main flow, by an air compressor. The information regarding the main flow, i.e. main flow total pressure and temperature, was obtained using a pressure transducer and a T-type thermocouple. Calibration was made by changing the Yaw and Pitch angles of the probe using two different motors for each rotation and acquiring the related pressure measuring by the probe. Yaw and pitch angles were varied from -18° to +18° and -28° to +28° respectively. In addition, the Mach number of the main flow was also varied in the range of 0.05 ~ 0.6 to take also account the main flow variations.

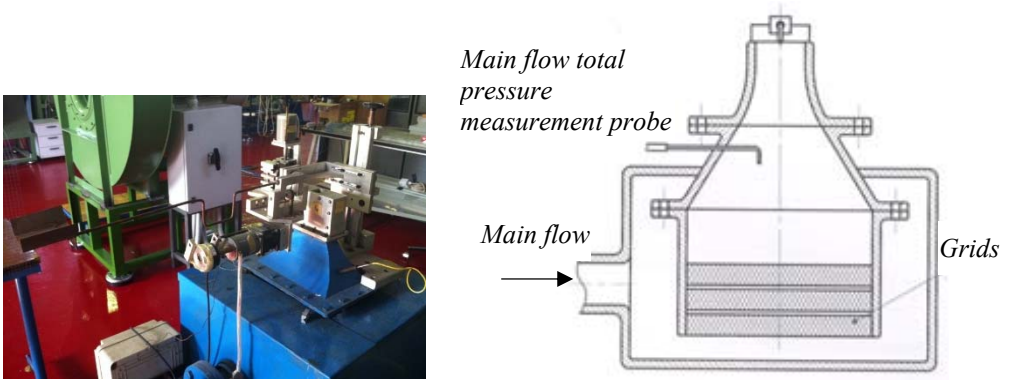

Fig. 3.17- 5-hole probe calibration system design and assembly

3.2. Cooled Cascade

For the heat transfer set of experiments, a system of cooling for the vane and endwall was designed. Endwall cooling was performed using a purge slot known as "purge gap" positioned upstream of the vane cascade according to Fig. 3.18, and as one could note, it is extended over three vane passages. The CAD design and configuration, for the purge gap is shown in Fig. 3.19. A plenum was designed in the back part of the purge gap endwall in order to connect the injection line to the purge slot. An assembly of the CAD design for the endwall cooling system is shown in Fig. 3.20, while the manufactured plenum is shown in Fig. 3.21.

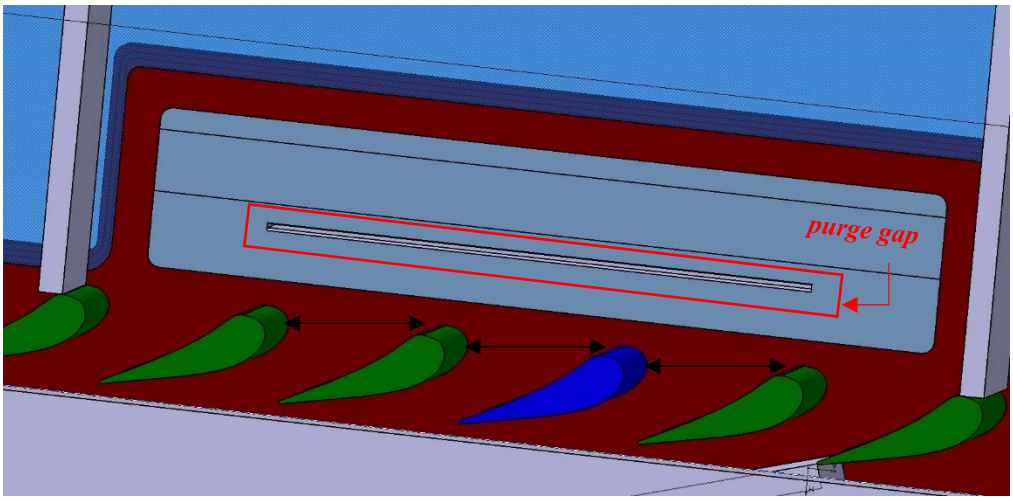

Fig. 3.18- Purge gap position

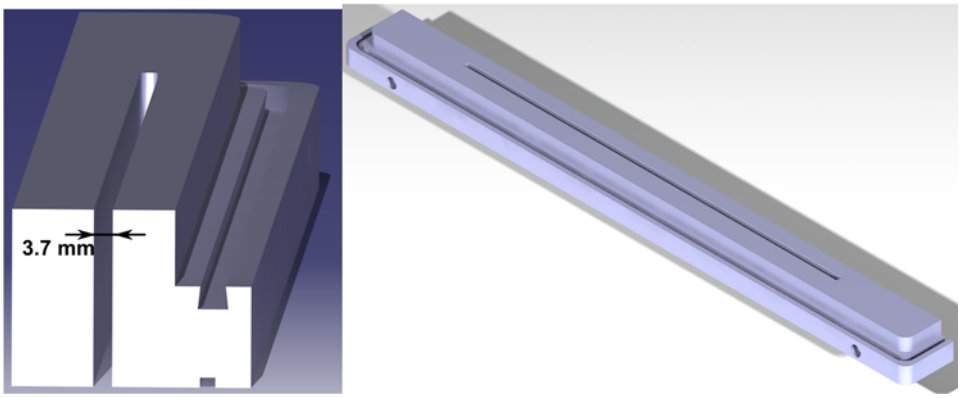

Fig. 3.19- "Purge gap" slot design and configuration

As it can be seen in this figure, metal grids were placed inside the plenum to deliver a uniform coolant flow exiting from the purge gap. Two pressure taps were located at each side of the plenum and an average of both pressures is acquired for measurement of the total pressure inside the chamber. In addition, two T-type thermocouples were placed inside the chamber to measure the temperature of the coolant.

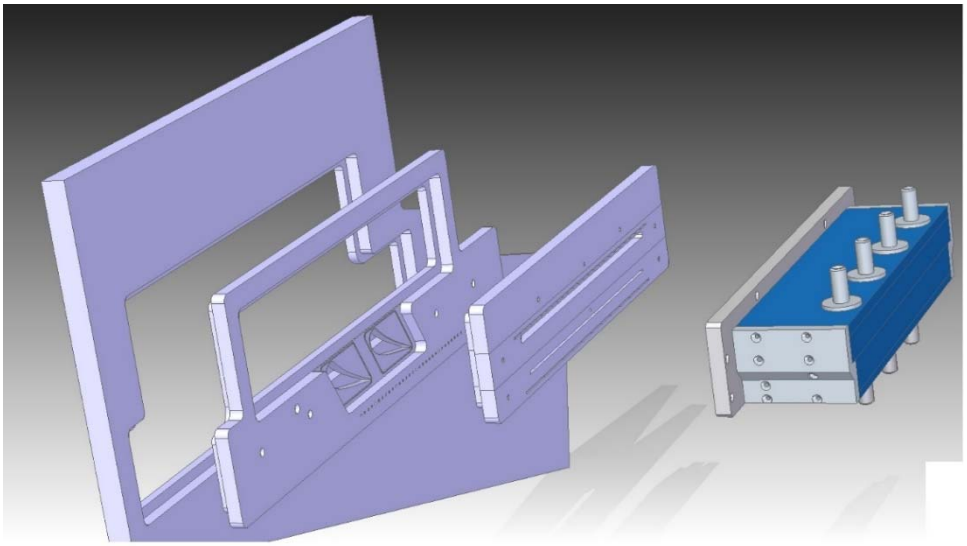

Fig. 3.20- Plenum design and assembly for the purge gap inject slot

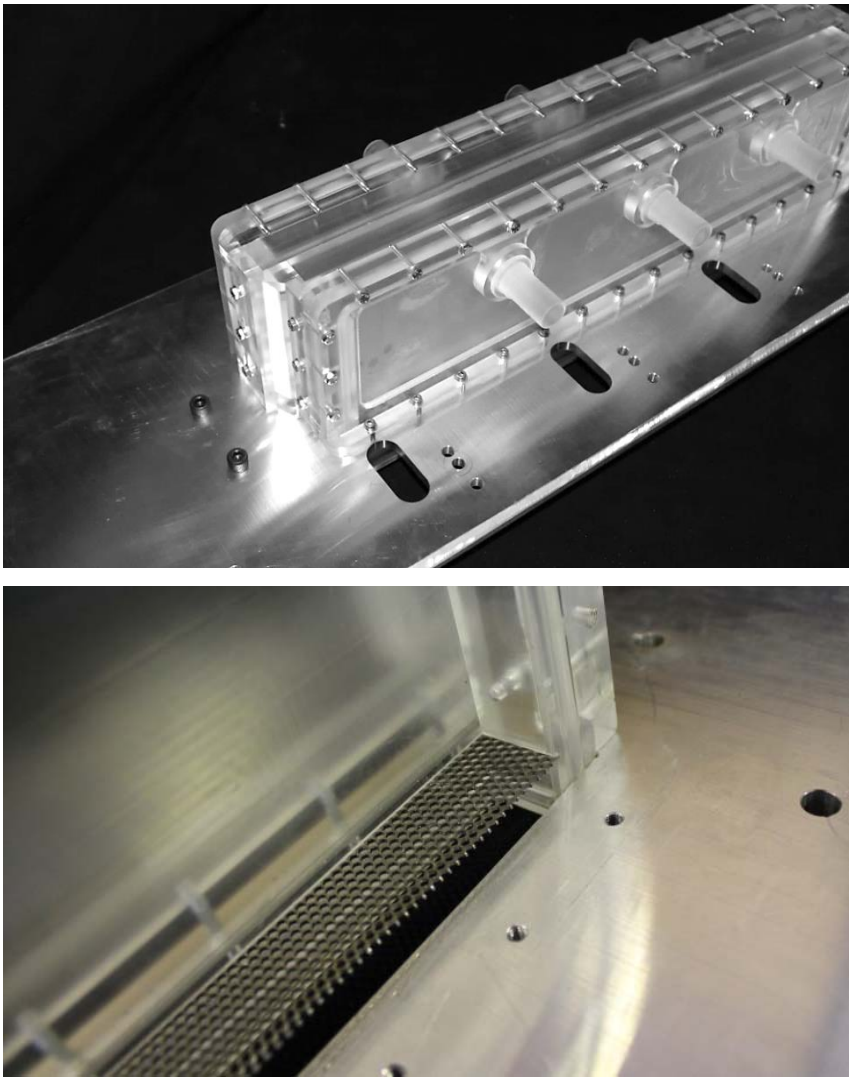

Fig. 3.21- Manufactured Plenum for the purge gap injection

Film cooling investigations on the vane were done by a showerhead cooling configuration, in which 4 staggered rows of cylindrical holes were designed in the vane leading edge zone, both on suction and pressure sides of the vane. In each row, there are 21 holes, normal to the vane profile, with a 45° angled to the radial direction toward the vane tip (see Table 3.2). A feeder chamber is designed inside the vane and the coolant is driven from the plenum into this chamber by flexible tubes. The pressure and temperature of the coolant inside

this chamber were measured by a pressure tap and a T-type thermocouple, to control and monitor the coolant condition. Fig. 3.22 demonstrates the 3D design of the vane and Fig. 3.23 illustrates the final manufactured vanes.

Table 3.2- showerhead cooling system specifications

P/D (hole pitch/ hole diameter)	7.33
L/D (hole length/hole diameter)	6.83
n° rows	4
hole radial angle	45°

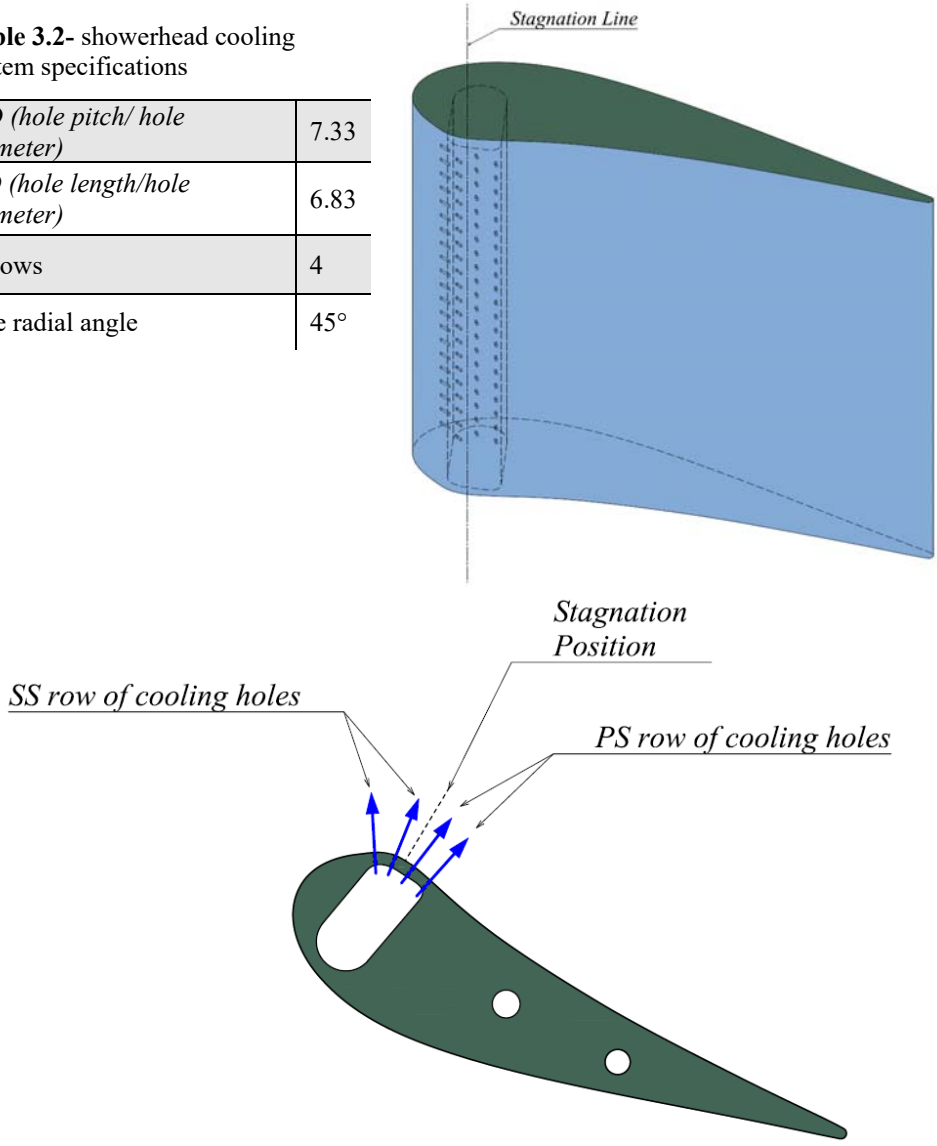

Fig. 3.22- Showerhead cooling configuration and design data

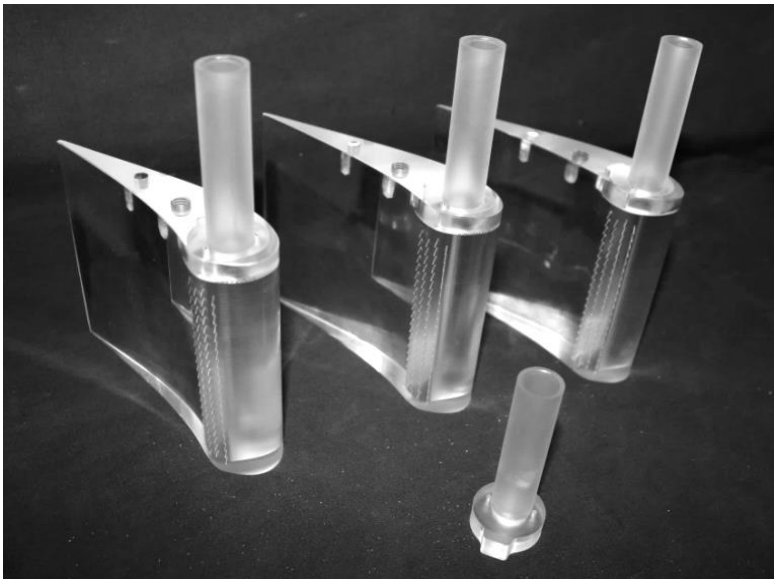

Fig. 3.23- Manufactured vanes with showerhead cooling scheme

Air was used as a coolant in this study for both showerhead and purge gap injection cases. It was produced from an air compressor unit and was controlled by control valves. The air was directed by metal pipes which were equipped with electrical heaters to increase the coolant temperature for heat transfer measurements purpose. Each of these pipes were connected to a primary plenum, and from these primary plenum, the air was transferred to the purge gap plenum and/or vane showerhead feeder chamber by flexible pipes according to Fig. 3.24.

The power required by the heaters for elevating the coolant temperature for heat transfer measurement purposes was calculated based on these assumptions; the inlet air temperature equal to the ambient temperature (20°C), the final air temperature 45°C and the specific heat (c_p) for the air is constant in this temperature range. Using these assumptions, the required power was calculated based on the mass flow rate for each cooling scheme. Therefore, for the showerhead line, a *1000W* heater was selected, while the purge gap line was equipped with a *3000W* because of its higher mass flow.

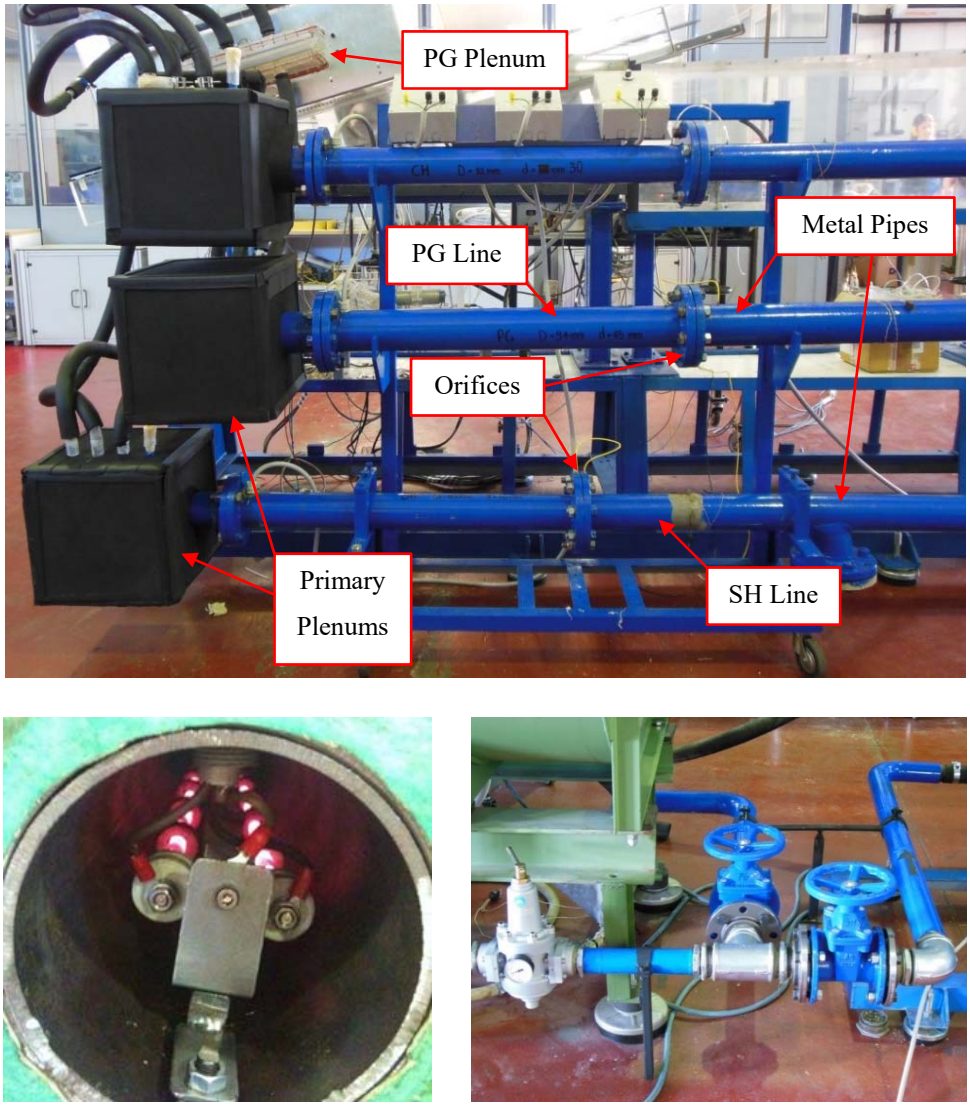

Fig. 3.24- Pipes connection between the compressor manifold and the plenums *(up)*; Regulating valves *(down right)*, Electrical heaters placed inside the pipe *(down left)*

For controlling the power for the selected heaters on each line, variable resistant "rheostat" was used. An adjustment rheostat knob was used to manually adjust each rheostats resistance during the experiments (see Fig. 3.25). Therefore, the current directed to each heater varies, hence the exiting coolant temperature alters. For the heat transfer measurements, the temperature of the coolant was adjusted in advance and then the experiments started.

Coolant injection conditions for each cooling scheme were controlled through a continuous monitoring of coolant mass flow and of the corresponding total pressure and temperature. The injected mass flow was measured by orifice devices placed inside the metal pipes.

Fig. 3.25- Rheostats using for regulating the power of the electrical heaters

4

Measurement Techniques

Different measurement techniques were utilized in this research in order to investigate aerodynamic and heat transfer performance of the vane cascade. For the heat transfer part of the study Thermochromic Liquid Crystals (or TLC) was applied, and for the aerodynamic investigations, as it was briefly mentioned in chapter 3, different instruments were used. In this chapter, all those instruments and measurement techniques will be thoroughly explained, including the uncertainty of each measurement. Uncertainty in all cases was estimated performing a perturbation analysis [43].

4.1. Aerodynamic Measurements

5-hole miniaturized aerodynamic pressure probe (1.6 mm head, advanced 50 mm to the stem) was used for aerodynamic measurements at 50% of the axial chord downstream of the trailing edge plane (X/c_{ax} = 150%). The measurement plane covers two blade passages and extends up to the blade midspan. Uncertainty in both static and total pressure was estimated to be ± 0.15% of dynamic pressure. Cascade inlet total pressure and 5-hole probe data were used to compute secondary velocity components, deviation angle $\Delta\beta$, kinetic energy loss coefficient ζ and vorticity Ω. Finally, the streamwise vorticity Ω_s was evaluated from Ω_x and Ω_y. The experimental results allow a direct estimate of Ω_x, however the Ω_y was computed in an indirect way [64], by following the procedure proposed by Gregory-Smith et al. [39], based on Crocco relation:

$$\Omega_y = \frac{1}{u}\left(\Omega_x v + \frac{a^2}{\gamma}\frac{\partial \ln p_t}{\partial Z}\right) \quad (4\text{-}1)$$

The computed uncertainty in the ζ value was ± 0. 3% at ζ = 3% and ± 0.2% at ζ = 60%, while in the flow angle it was ± 1°.

An instrumented vane was used for measuring the profile pressure distribution equipped with 39 wall taps, distributed along the vane midspan. These pressure taps are connected to a Scanivalve in order to acquire the pressure in different test conditions. The computed uncertainty for this pressure measurement was δMa_{is} = ±2%.

The inlet flow characteristics were measured by a 2D laser Doppler velocimetry (LDV). The light source was a 300mW Ar+ laser. All the measurements were carried out acquiring 20,000 burst signals at each location. Sawdust smoke was used to seed the flow. The high number of acquired signals assured statistically accurate averages; based on a 95% confidence level, uncertainties of ±0.5% and ±1.0% for mean and RMS values, respectively, have been obtained for a turbulence intensity level of 35%.

Coolant injection conditions for each cooling scheme (slot and vane showerhead) were controlled through a continuous monitoring of coolant mass flow and of the corresponding total pressure and temperature. The injected mass flow was measured by orifice devices. Coolant total pressure and temperature were measured in the feeding chambers by pressure taps and T-type thermocouples. Uncertainty for m_c was computed according to international standards for orifice devices (EN ISO 5167-2:2003(E)). Based on a 95% confidence interval δm_c resulted to be always lower than ± 2.1% for all the cooling systems.

4.2. Thermal Measurements

In the following, a description of TLC measurement used in this study and the relevant calibration procedures for the platform and for the vane, developed at turbomachinery research group of the University of Bergamo, is reported [35, 37].

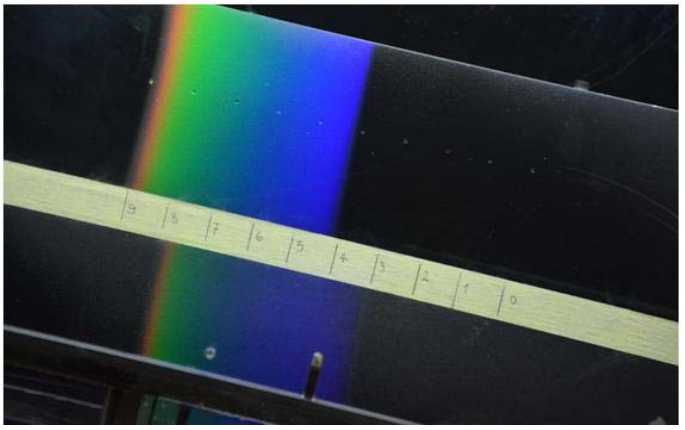

Fig. 4.1- An example of a TLC picture

Film cooling effectiveness on the platform and on the vane was obtained using the transient Thermochromic Liquid Crystal technique. For the platform, the calibration of wide banded TLC (10°C bandwidth) was performed on an instrumented flat aluminum plate shown in Fig. 4.2, which is equipped with 10 calibrated T-type thermocouples ($\delta T = \pm 0.1$°C). The surface is illuminated by means of two strips of white light LED while the color play of TLC is captured by a Nikon D7100 camera with a resolution of 4496×3000 *px*. For the vane, because of its curvature profile on the leading edge area, calibration was done using an aluminum cylinder shown in Fig. 4.3. This is due to resembling the leading edge curvature and thus, to limit the color perception. This cylinder is equipped with 12 calibrated T-type thermocouples ($\delta T = \pm 0.1$°C). The surface is illuminated by the same LED strips used for the flat plat calibration, and the same Nikon D7100 camera but with borescope mounted was used with an exposure time of 1/20s and a resolution of 6000×4000 *px*.

Heat transfer study has been performed during the different time of the year, thus a variation in mainstream temperature between summer and winter was inevitable. Therefore, in general, two types of TLC with different red start temperature was used: *20°C* red start for cold seasons and *25°C* red start for warm seasons. In Fig. 4.2 both TLC were applied on the calibration plate, in which 25°C red start TLC started to illuminate at higher T.

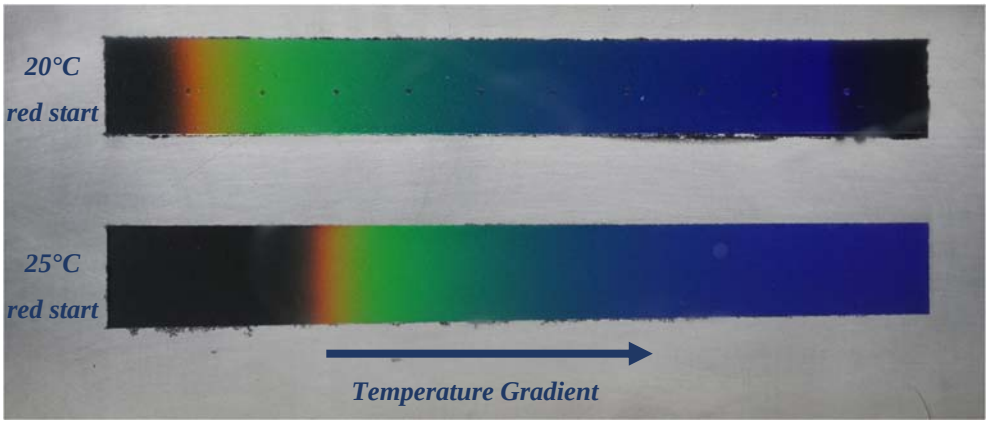

Fig. 4.2- Aluminum calibration plate for 20°C and 25°C red start temperature TLCs, applied for measurement of the platform film cooling effectiveness

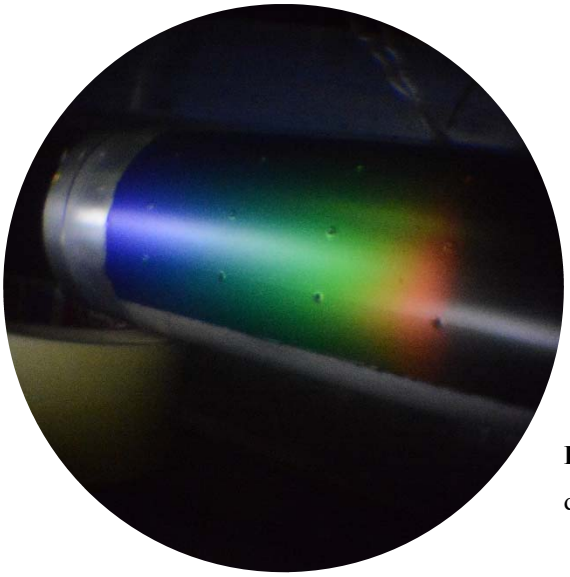

Fig. 4.3- Cylindrical shape calibration device inside the wind tunnel

For TLC measurements, the camera must stay perpendicular with respect to the surface otherwise color perception would happen and as a result, a significant unwanted measurement error occurred. For the endwall cooling measurements this was not the problem; however, investigations on the vane encountered some limitations. Due to the presence of the turbulence generator, a direct access to the leading edge region was not allowed. To overcome this problem, a 6 mm diameter borescope was connected to the camera (Fig. 4.4). Moreover, to allow to capture images from both PS and SS of the vane, the upstream section of the wind tunnel side wall was modified in order to incorporate a traversing system (Fig. 4.4). With such a solution, the borescope, and the camera as well, can move continuously along the tangential direction at a fixed distance from the vane leading edge of 65 mm, corresponding to $0.95c_{ax}$. In this way, each test on the vane must be divided into two experiments, one on SS and another experiment individually on PS of the vane. Fig. 4.4 clearly illustrates these two distinct experiments and also shows the borescope used in this study inside the tunnel. Typical images according to this procedure is here presented in Fig. 4.5.

The calibration procedure was initiated by generating temperature gradient over the aluminum plate surface, using an electrical heater placed inside the calibration plate on the right side of Fig. 4.2. On the other side, cooling water was circulated inside the plate to reduce the temperature on the left side of the Fig. 4.2. The device were first black painted and then sprayed with TLCs. Then, when a stable rainbow colored appeared on the calibration device, temperature acquisition and image capturing were performed simultaneously. Between the camera and the calibration plate, a piece of Plexiglas with a thickness similar to the wind tunnel wall thickness (*35mm*) was placed in order to take real test condition into account.

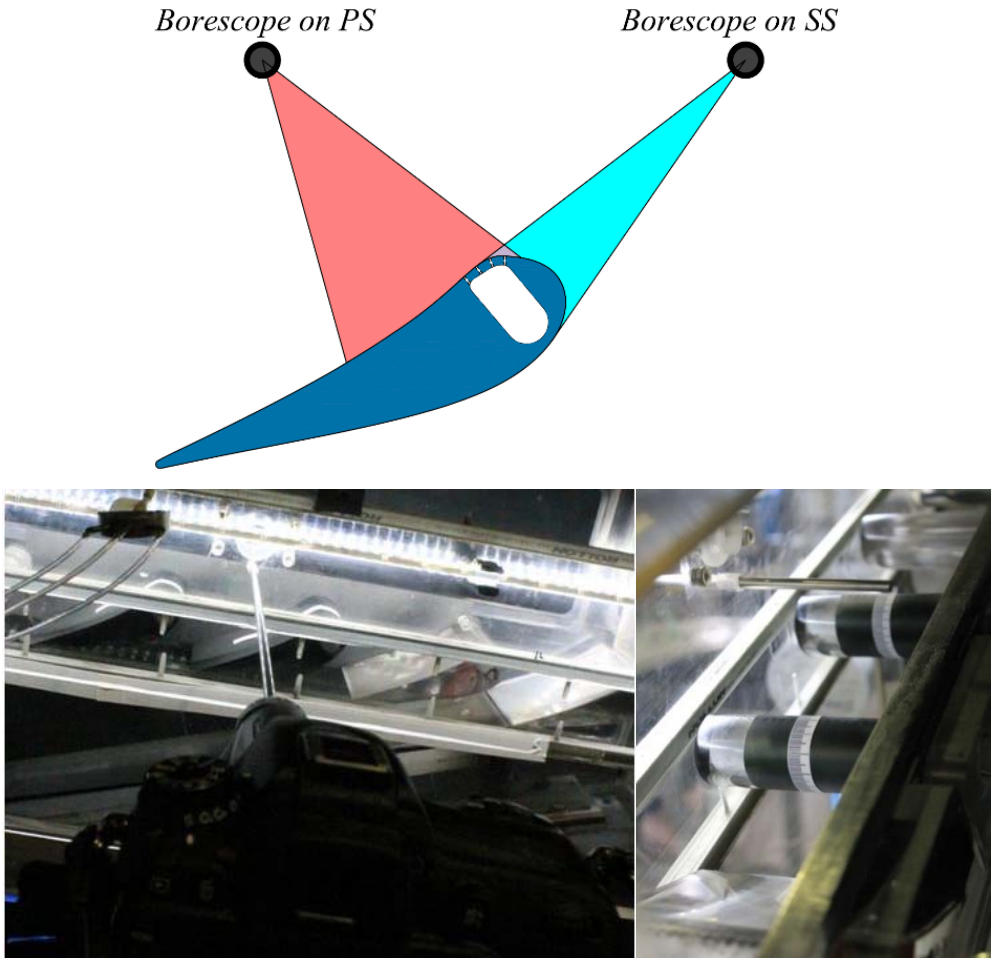

Fig. 4.4- Borescope and its configuration inside the tunnel

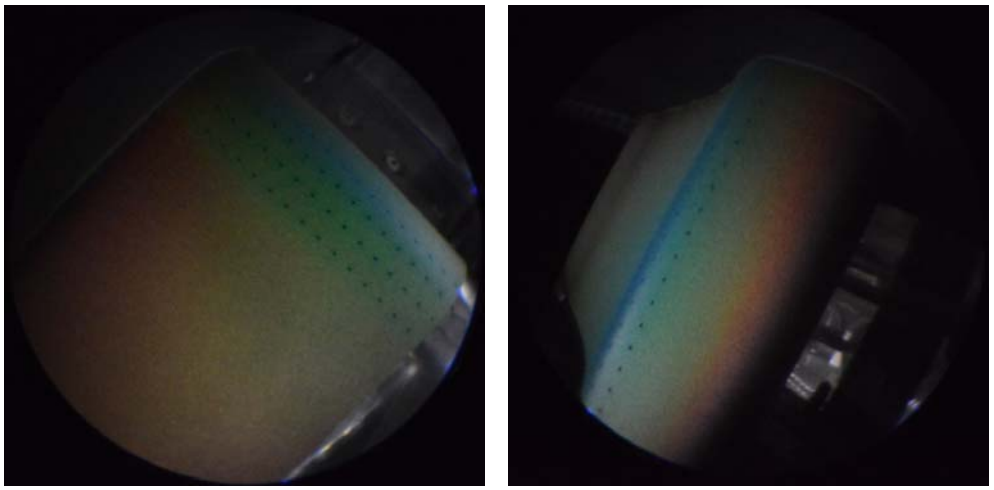

Fig. 4.5- Borescope and its configuration inside the tunnel

For the cylindrical calibration device, the same procedure was followed; a temperature gradient is generated by a heater on one side and a water cooling zone on the other side of the cylinder. When a stable TLC color appeared, temperature acquisition and image capturing performed together. Since in real tests the borescope goes inside the wind tunnel, a Plexiglas piece was not placed between the borescope and calibration device.

RGB images are then converted in HSI code [38]: the HUE value for each pixel was then extracted and put together with the corresponding temperature value (linearly interpolated between the thermocouple data) to generate a HUE-temperature calibration curve as shown in Fig. 4.6. For the cylindrical device, images were taken at several inclination angle with respect to the camera axis, allowing to define a relationship between curvature and color change, then a vertical slice 4.5° wide was extracted at several angular positions. As Fig. 4.6 shows, all curves almost collapse on a unique trend when HUE is below 120. For larger HUE values (corresponding to the blue color), increasing the angle, i.e. increasing the surface curvature, a decrease in the temperature value can be observed. This means that in regions of high curvature, the same temperature value is expected to move the color perception towards the blue. Also note that the presence of the borescope modifies the calibration curve only at the high HUE [52]. However, for all the tests such a high HUE values were never reached, thus eliminating any further color perception error. It should be noted that all calibrations and measurements were performed in the dark, in order to eliminate any influence of background illumination. Moreover, an illumination intensity was provided as uniform as possible to the model surface by properly orienting the lighting system, in the meanwhile avoiding any light reflection onto the camera.

After performing the calibration, quasi-steady tests were applied to measure the adiabatic film cooling effectiveness (η) both on the platform and on the

vane. The quasi-steady tests were realized heating the coolant while the mainstream flow stays at room temperature. A test was done in advance to verify the influence of SH on platform cooling. The same test was repeated validating the influence of PG on vane showerhead cooling. Neither the former nor the latter effects were observed. Therefore, platform tests were done by heating only the PG coolant; likewise, during the measurements on the vane only the SH coolant was heated.

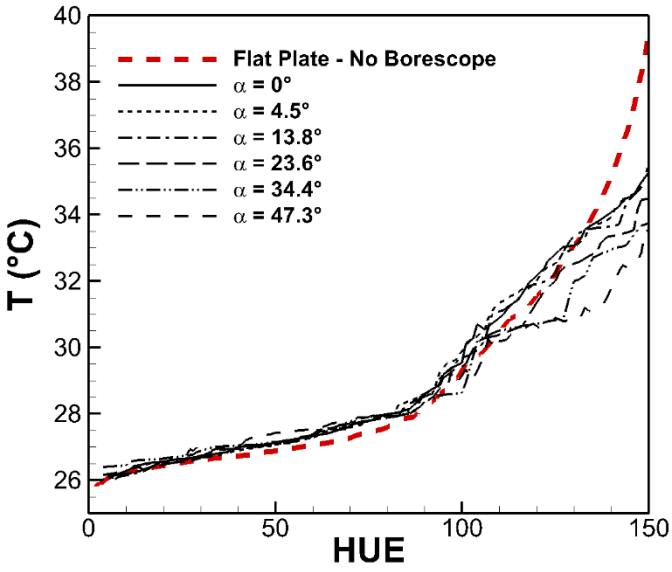

Fig. 4.6- TLC calibration curves for variable surface curvature α

During experiments, the ambient temperature was controlled in order to have a red color as uniform as possible on both platform and leading edge vane surfaces; i.e. at the lower bound of TLC active band, with the wind tunnel running at the desired Mach number. PG and SH cooling supply lines had been previously set at the desired mass flow rate and the cooling air was heated up at about 40°C (resulting in a density ratio *DR* of about 0.95), but blowing in the atmosphere. When a stable temperature was reached inside the primary plenums, as well as a red color on the surfaces, cooling lines (flexible tubes) were suddenly connected to their relative cooling systems. In the meantime, the camera starts acquiring images at a fixed rate of about 1 fps and temperature variation inside the feeding chamber T_c and main flow temperature T_∞ were

acquired as well for a test duration of 60s. The temperature variation inside the SH and PG plenums are presented in Fig. 4.7.

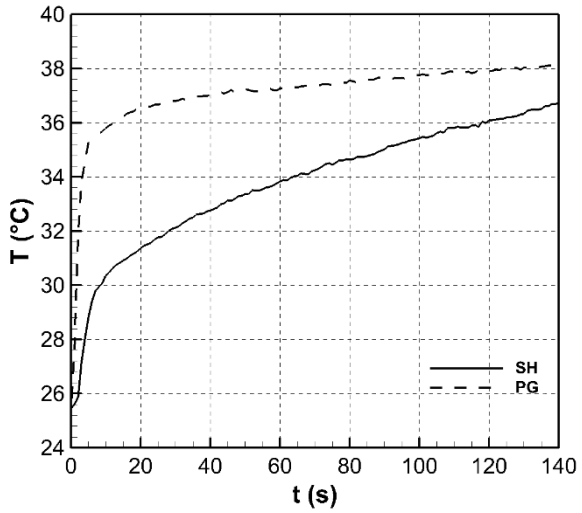

Fig. 4.7- Temperature variation inside the SH and PG plenum during a test

For measuring η, the RGB to hue conversion [38] is applied to a single image recorded after a time period of about 20 to 30*s*, i.e. before conduction effects around the cooling area become too relevant and when a stable temperature level inside the plenum was reached, for both platform and vane investigations, as well as on the tested surface. Each image was also selected in such a way to avoid significant conduction phenomena For the SH cooling case, the image was always selected after 30s, when the temperature difference between the internal cavity and the surface became negligible, and a correction was applied using a FEM calculation. For the purge gap the image was selected checking for conduction effect. Conduction was checked by looking at the upstream of the purge slot, where it was painted in advance with the TLC to check the TLC color change made by the conduction effect. Moreover, each image was recorded with a 1*s* exposure time: each image thus reflects an average of platform surface temperature over this same time interval. As this time interval is reasonably long, no further averaging over multiple images was performed. This again to limit conduction phenomena. For the vane, to correct the distortion in the acquired images and to correctly size each image as well, a

ruler was attached on the vane surface. Fig. 4.8 shows an example of pictures taken to correct image distortion.

TLC measurement is a heat-transfer based technique and data obtained from heat transfer techniques are known to have conduction effects around the injection area [56]. The conduction effect may lowers the accuracy of data and it's an unavoidable problem associated with heat transfer techniques. In quasi-steady measurements, conduction won't happen for the platform cooling because of the short test duration. However, on the vane despite the low conductive material (Plexiglas) used in this investigation, the conduction happened. Mostly because of the small thickness of material around the injection holes on the vane. Therefore, the vane surface temperature measured by TLC in the showerhead region was lowered to eliminate conduction effects in between the rows of holes.

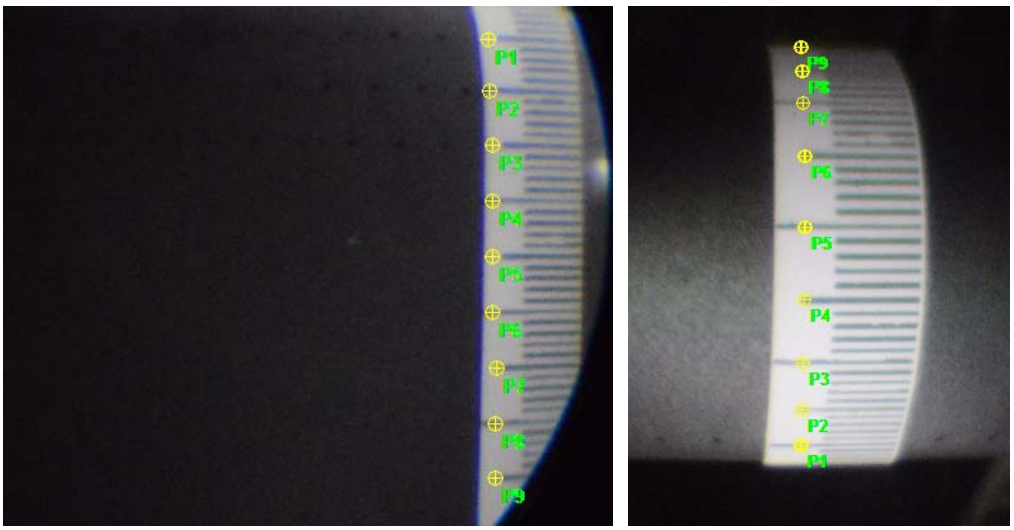

Fig. 4.8- Reference images for distortion correction for PS *(Left)* and SS *(Right)* of the vane

That reduction was derived from a preliminary time-dependent finite element method (FEM) simulation carried out using Comsol Multiphysics® [52, 55]. Fig. 4.9 shows the calculated midspan vane surface temperature

distribution at t = 25s after the injection and the derived correction curve around the leading edge, at BR = 3.

The correction was assumed to be constant across the vane span. Therefore, conduction effects are still present around each cooling hole, but to a lesser extent. This procedure resulted in a reduction of the measured temperature by up to 2.2 °C, within -0.05<s/C<0.05. This correction was applied for the vane showerhead results in the region extending in between the rows of holes and surrounding the cooling holes.

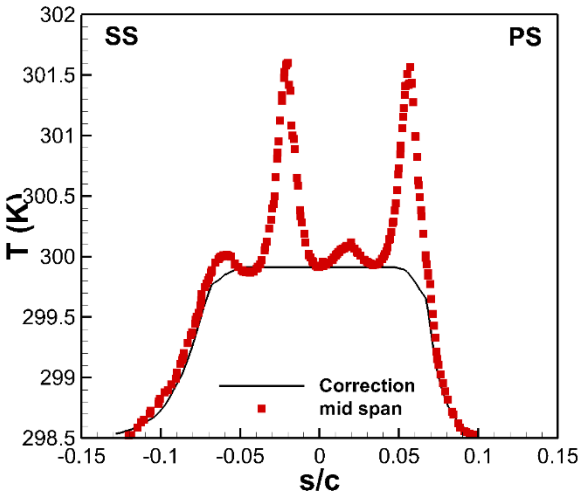

Fig. 4.9- Conduction correction at time t = 25s

Regarding the uncertainty of TLC measurements, the platform film cooling effectiveness uncertainty depends on TLC (δT_w = ± 0.3°C) and thermocouple measurements (δT_∞ = ± 0.1°C and δT_c = ± 0.5°C) and conduction effects. In regions where conduction phenomena do not exist, the η uncertainty will range from ± 4.2 % with η = 0.8, up to about ± 15 % when η = 0.1. No correction was applied to the data, as regions where conduction takes place are small and do not affect the general platform thermal behavior [43, 35].

For the vane showerhead, film cooling effectiveness uncertainty depends on the TLC, the thermocouple measurements and conduction effect as well. In region where conduction phenomenon do not exist, the η uncertainty will range from ± 4.7% with η = 0.8, up to about ± 15% when η = 0.1. [43, 44, 52].

5

Results

The objective of this research was to investigate the influence of the inlet flow angle on the aerothermal performance of a turbine nozzle vane cascade. For this purpose, the inlet flow incidence angle was varied and experiments were followed for each incidence angle. For each angle, LDV measurements were done for verifying the real flow incidence angle; once validated, the aerodynamic experiments were done both on the solid and cooled cascade. After characterizing the aerodynamic effects of that incidence angle, heat transfer measurements were followed starting with the endwall cooling experiments, and finally, vane film cooling investigations were performed.

For both sets of experiments, 0° incidence angle was the reference condition. The main flow Mach number was varied in order to investigate the main flow effects on the aerothermal performance. The condition in which all tests were run was Ma_1 (inlet Mach number) = 0.12; some variations in the $Ma_{2,is}$ took place depending on the incidence angle; this is due to a modification in the inlet cross section, and thus in the air mass flow through the wind tunnel. Coolant mass flow was designed to vary from nominal condition to minimum and maximum conditions for both purge gap injection and vane showerhead cooling injection. As it was mentioned, the mass flow was controlled during the experiments by measuring the pressure and temperature of the coolant inside the purge gap plenum and vane showerhead chamber. So, a calibration was made in advance for assigning each mass flow condition to a unique pressure

ratio. The injection line calibration was performed at each incidence angle and at each main flow Mach number. Fig. 5.1 illustrates the cascade geometry investigated in this study together with the measurement plane for 5-hole probe investigations. In Table 5.1(a) and 5.1(b), general test matrixes for all the performed aerodynamic and heat transfer experiments, respectively, is presented.

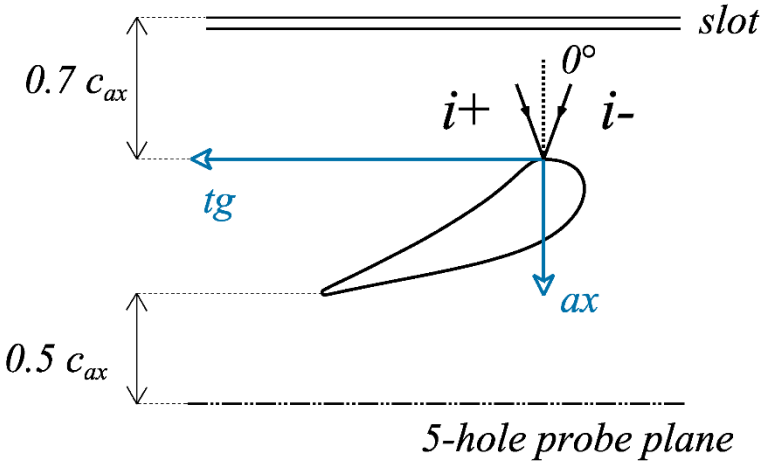

Fig. 5.1- Cascade geometry and the concept of incidence angle

Table 5.1(a)- General test matrix for aerodynamic investigations

	Test	Test type	Test Condition			Incidence angle				
			$Ma_{2,is}$							
			0.2	0.4	0.6	+20°	+10°	0°	-10°	-20°
Solid cascade	*Aerodynamics*	*Inlet boundary layer*	✓	✓	✓	-	-	✓	-	-
		Vane wake at cascade exit	✓	✓	✓	✓	✓	✓	✓	✓
		LDV upstream, of cascade midspan	-	✓	-	✓	✓	✓	✓	✓
		Vane loading	-	✓	-	✓	✓	✓	✓	✓
		Surface flow visualization	-	✓	-	✓	-	✓	-	✓
		3D flow field	-	✓	-	✓	✓	✓	✓	✓

Table 5.1(b)- General test matrix for heat transfer investigations

	Test	Test type	Test Condition $Ma_1 = 0.12$ ($Ma_{2,is} = 0.4$)						Incidence angle				
			PG			SH							
			Min	*Nom*	*Max*	*Min*	*Nom*	*Max*	+20°	+10°	0°	-10°	-20°
Cooled Cascade	***Aerodynamics***	*Vane wake at cascade exit*	-	✓	-	-	✓	-	✓	✓	✓	✓	✓
		3D flow field	✓	✓	✓	✓	✓	✓	✓	✓	✓	✓	✓
	Heat Transfer	*TLC test on endwall*	✓	✓	✓	✓	✓	✓	✓	✓	✓	✓	✓
		TLC test on vane (PS & SS)	✓	✓	✓	✓	✓	✓	✓	✓	✓	✓	✓

In this chapter results from the aforementioned procedure will be presented and a comparison between each incidence angle will be discussed.

5.1. Solid Cascade

5.1.1. 0° Angle Incidence, The Reference Case

The first tests were performed to verify the tunnel characteristics at 0° incidence with turbulence generator. To define the correct position of the turbulence generator with respect to the vane cascade, turbulence intensity was measured using a hot wire probe. The probe was positioned at a fixed distance from the leading edge plane (at $1.6c_{ax}$), varying the position of the turbulence generator. All turbulence values are calculated making use of only the streamwise fluctuating velocity component, so turbulence isotropy could be assumed as:

$$Tu_1 = \frac{\sqrt{\overline{u'^2}}}{U_1} \tag{5-1}$$

LDV measurements confirmed the isotropic assumption at least for the axial and tangential fluctuating velocity components. Fig. 5.2 shows the measured Tu_1 values as a function of the normalized distance of the turbulence generator from the vane leading edge at different cascade operating conditions, where *d* is the rod diameter equal to 10mm. Installing the turbulence generator at a distance of *22d* delivers a turbulence intensity (Tu_1) between 9% and 10% at cascade inlet, depending on the operating Mach number and thus Reynolds number. The numerical integration of the autocorrelation function of the acquired hot wire signals also yielded the integral length scale Λ_x.

Table 5.2 summarizes the measured Tu_1 values, the corresponding values of the integral length scale and the expected Tu_1 value at the leading edge plane. Since the turbulence decay rate could be estimated, Tu_1 level at vane leading edge was estimated using the correlation shown in Fig 5.2. In addition, the LDV tests confirmed the validity of this prediction.

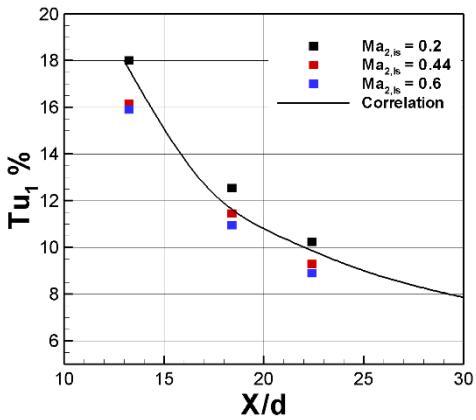

Fig. 5.2- Turbulence intensity vs. the position of turbulence generator

Table 5.2- Inlet turbulence characteristics

Operating cascade Mach number	*0.2*	*0.4*	*0.6*
%Tu_I at HW probe location (x/d = 13.25)	18.0	16.15	15.9
Λ_x *(mm)*	14.9	11.8	11.5
%Tu_I at cascade inlet (x/d = 22)	10.2	9.3	8.9

After characterizing the turbulence intensity level, the inlet boundary layer was investigated at $1.6c_{ax}$ and at three tested cascade operating conditions. The result is reported in Fig. 5.3 and in Table 5.3. As Fig. 5.3 clearly shows, no differences in the approaching boundary layer were detected since the inlet Mach number only changes between *0.056* to *0.16*. In all cases, integral parameters indicate the presence of a fully turbulent boundary layer.

The 5-hole probe traversing was done at 50% c_{ax} downstream the trailing edge plane to characterize the wake structure. Fig. 5.4 reports results from the midspan probe traversing along two vane passages, for three tested Mach number.

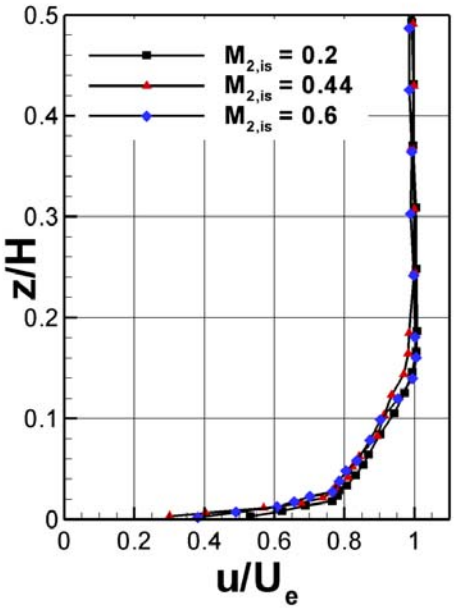

Fig. 5.3- Inlet boundary layer profile at $1.6c_{ax}$

Table 5.3- Inlet boundary layer characteristics

Operating cascade Mach number	*0.2*	*0.4*	*0.6*
Thickness δ (mm)	14.6	14.8	14.7
Displacement thickness δ^* (mm)	2.06	2.3	2.53
Momentum thickness (mm)	1.49	1.53	1.74
Shape factor H_{12}	1.38	1.5	1.45

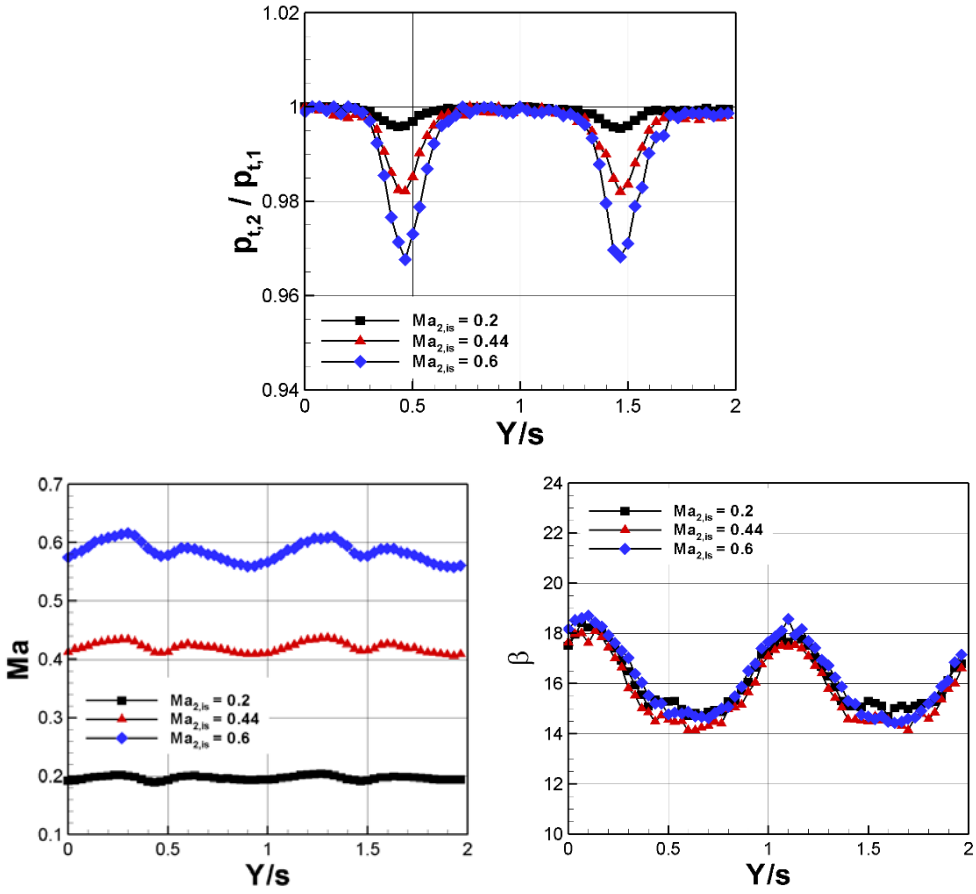

Fig. 5.4- Vane wake profiles at cascade exit (0.50c_{ax}); total pressure ratio (*up*), Mach number distribution (*down left*) and flow exit angle *β* (*down right*)

Figure 5.5 shows the kinetic energy loss coefficient distribution and vorticity distributions with superimposed the secondary velocity vectors. The measurement was made by 5-hole probe traversing at 50% c_{ax} downstream of

the vane trailing edge covering the half vane span and at $Ma_{2,is} = 0.4$. According to Fig. 5.5 one can notice a well-defined secondary flow structure. Looking at the endwall (*Z/H=0*), the loss core regarding the corner vortex has a higher peak value than the passage vortex; however, the flow filed is mainly dominated by the passage vortex. It can be perceived by the wide high loss region on the SS of the wake. Moreover, it can be observed that the wake is relatively thick and that the two dimensional region is limited to a narrow span around the mid span.

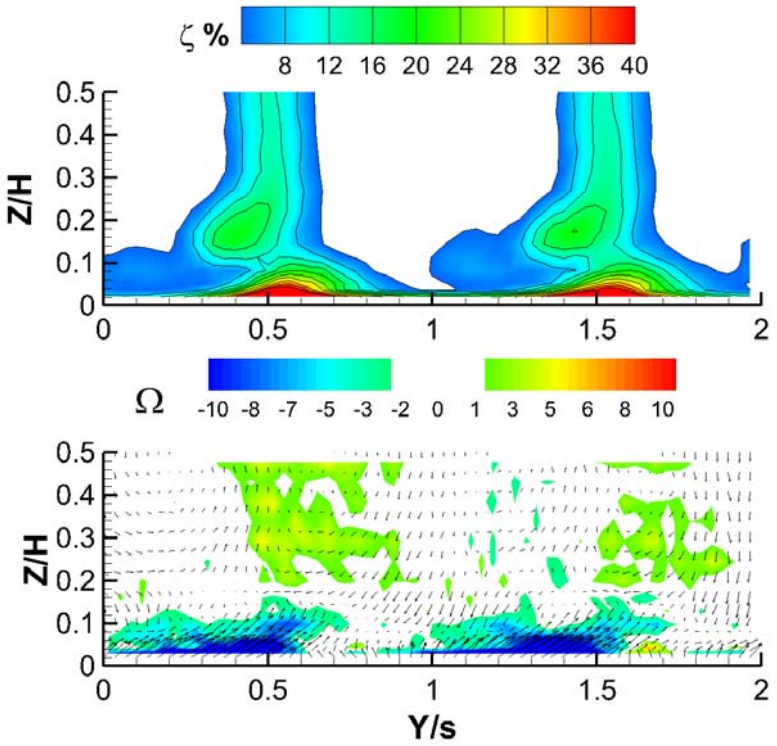

Fig. 5.5- Kinetic energy loss distributions *(up)* and vorticity distribution with secondary velocity vectors *(down)* measured at $0.50c_{ax}$, ($Ma_1 = 0.12$, $i = 0°$)

The data presented in above section were assumed to be the reference conditions since they were done at 0° incidence angle and the cascade was not cooled. To characterize the effect of the coolant on the aerodynamics, the above

experiments were repeated with the cooled platform, which will be thoroughly discussed later in section 5.2.

5.1.2. Inlet Flow Investigations(LDV results)

To characterize the inlet flow condition for different incidence angles, a 2D LDV probe was traversed at three axial locations upstream the leading edge plane: at X/c_{ax} = - 0.35, - 0.80 and - 1.6; however only data belonging to the X/c_{ax} = - 0.35 location are shown here, as they present a better idea of inlet flow condition for variable incidence. Fig. 5.6(a) & 5.6(b) illustrate the pitch wise profiles of flow angle and Mach number distribution in various incidence angles, respectively. It should be mentioned that the flow angle β is defined with respect to the axial direction, which means that a positive inlet flow angle will result in a negative incidence to the vane according to the incidence definition.

The reported distributions show a periodic flow distribution along the pitch in the cascade entrance region and a good consistency between the different incidence cases in terms of inlet Mach number, being the averaged inlet Mach number always about 0.12. By averaging the inlet flow angle values over the two pitches and taking the one measured at the theoretical 0° incidence case as a reference, the actual incidence angle reported in Table 5.4 are obtained.

The slightly negative incidence detected at the theoretical 0° incidence case (it should be note that the positive inlet flow angle of 4.3° corresponds to a negative incidence according to incidence definition) is due to the turbulence generator that induces a flow deviation upstream of the cascade.

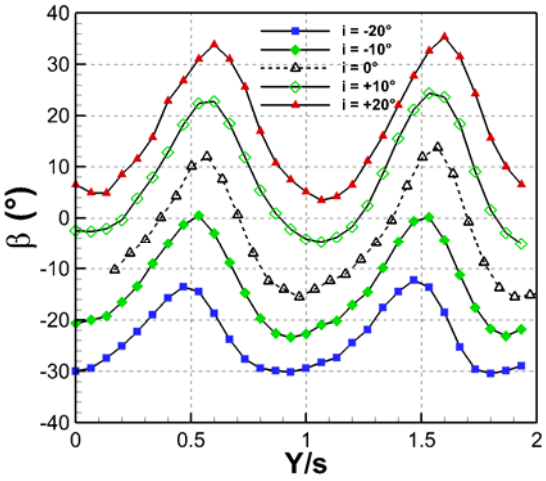

Fig. 5.6(a) - Inlet flow angle at X/c_{ax} = -0.35 for variable incidence angles (Ma_1 = 0.12)

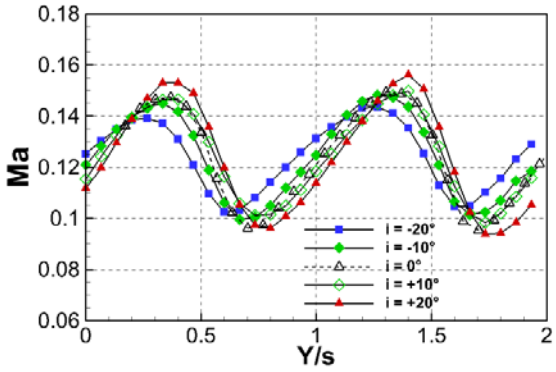

Fig. 5.6(b) – Ma distribution at X/c_{ax} = -0.35 for variable incidence angles (Ma_1 = 0.12)

Table 5.4- Inlet averaged flow angle for variable incidence angle

i theoretical (°)	*β(°)*	*i* actual (°)
-20	*23.6*	*-19.4*
-10	*13.6*	*-9.3*
0	*4.3*	*0*
+10	*-7.2*	*11.5*
+20	*-17*	*21.3*

5.1.3. *Vane Load*

In the next step, vane load distribution was measured using the instrumented vane described in chapter 4. The result is presented in Fig. 5.7 which reports the vane load distributions measured at a fixed inlet Mach number of 0.12 and variable incidence. The effect of the inlet flow incidence angle can be clearly seen in this figure: the positive incidence angle results in an increased load on the vane and a shift of stagnation line toward the pressure side of the vane, particularly evident in the +20° incidence case. No flow separation is observed along the suction side. The peak Mach number on the suction side is only slightly reduced, while the adverse pressure gradient is anticipated.

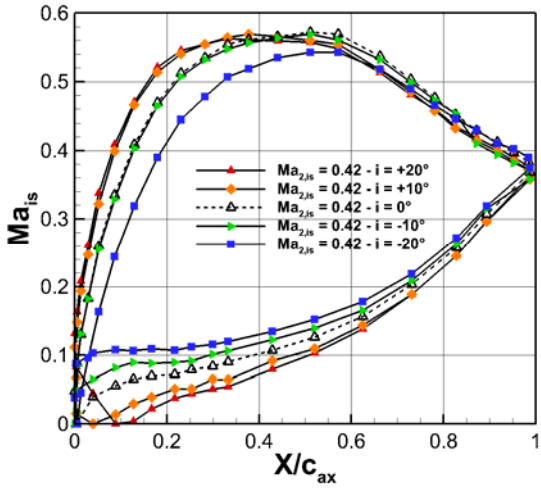

Fig. 5.7- Vane load distribution at Ma_1 = 0.12 for variable incidence angles

Conversely, the negative incidence results in a reduced load on the vane front side and in a shift of the stagnation point towards the suction side. The peak Mach number on the suction side is significantly

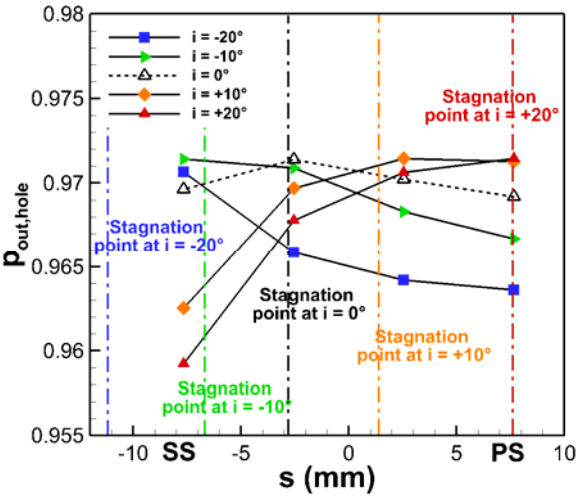

Fig. 5.8- Pressure values at hole exit section, data derived from vane load distribution in Fig. 5.7

reduced, while the adverse pressure gradient is slightly postponed. A shift of the stagnation point towards the suction side also takes place for the -10° incidence case, while the front loading almost remains the same as for the 0° incidence case. The movement of the stagnation line is responsible for the variation in the film cooling efficiency on the vane and could be considered as the key parameter for designing the cooling configuration on the vane.

From load distribution, static pressure at holes exit location was computed for the different inlet flow angles. Results are reported in Fig. 5.8. Also, the stagnation line position variation is reported. It should be noted that the stagnation line at 0° incidence is in fact shifted towards the suction side with respect to its theoretical position, due to the slightly negative inlet flow angle. Looking at this figure, one could note that the pressure distribution over the cooling holes is varying at each incidence angle. At +20° incidence, the outlet hole pressure is decreasing from last row on PS to the upstream rows. This gives an anticipation that for +20° incidence, most of the coolant would be delivered toward the SS. At -20 incidence, however, the pressure is decreasing from the row located at SS to the last row located at PS; thus the coolant would be delivered toward the PS.

5.1.4. Surface Flow Visualization (oil&dye)

Oil & dye surface flow visualization was then done on the platform to get traces of the 3D flow structures at the endwall, as well as on the vane suction side. Fig. 5.9 shows the flow visualization for -20°, 0° and +20° incidence angles on the endwall, while Fig. 5.10 shows vane SS one. All tests were done at nominal Mach number. The shift for the stagnation line at each incidence angle was evident on the platform and is marked in Fig. 5.9. Both figures show clearly that by increasing the incidence angle, secondary flows undergo a significant enforcement and that the spanwise region affected by the passage vortex is also widening considerably. In fact, oil & dye trace at the trailing edge

increases from about 13.5% of vane span for the -20° incidence case, to 17.5% for the 0° incidence case up to 27.3% of vane span for the +20° incidence case.

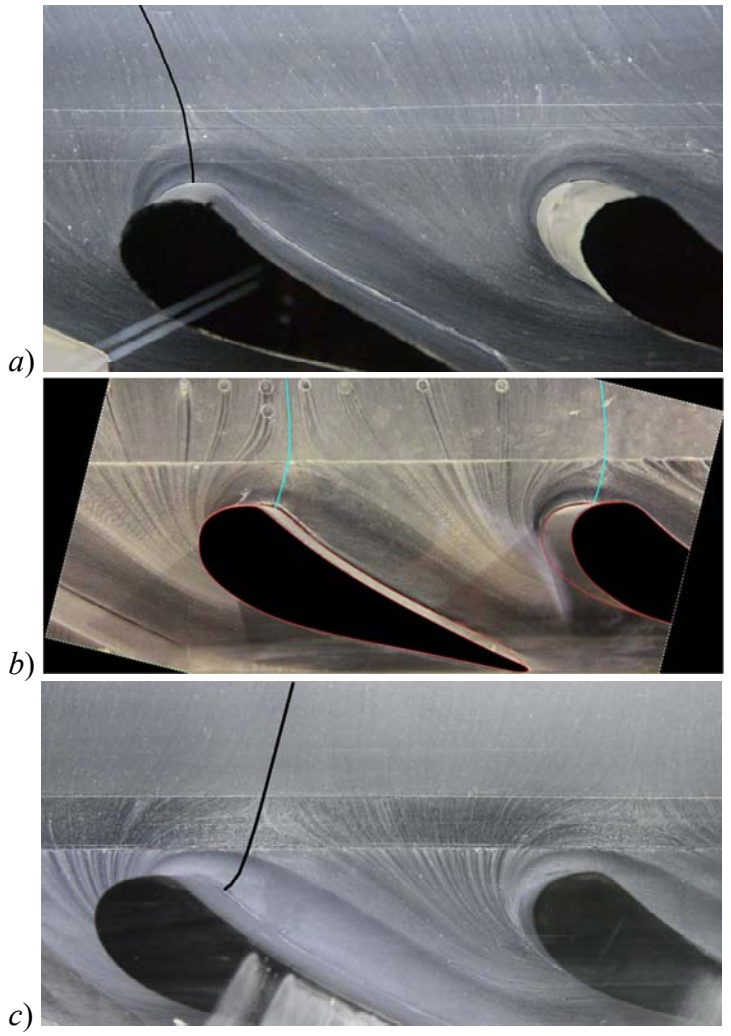

Fig. 5.9- End wall Oil and dye flow visualization for $Ma_1 = 0.12$: *a*) $i = -20°$, *b*) $i = 0°$ and *c*) $i = +20°$

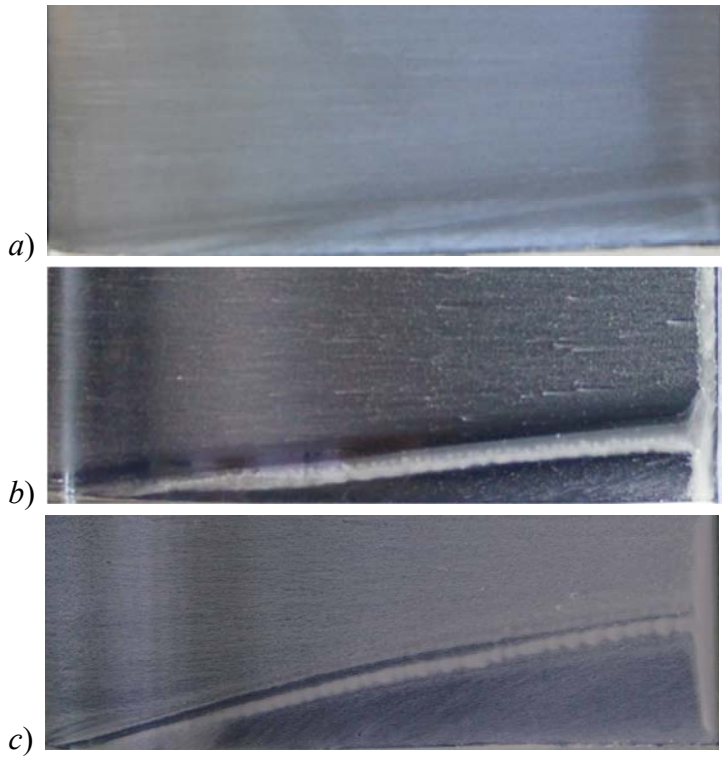

Fig. 5.10- Vane SS Oil and dye flow visualization for $Ma_1 = 0.12$: *a*) $i = -20°$, *b*) $i = 0°$ and *c*) $i = +20°$

5.1.5. *3D Flow Filed investigation (5-hole probe experiments)*

The 3D flow field downstream of the cascade was then analyzed in order to evaluate the cascade aerodynamic performance at each incidence angle. Data reported in Fig. 5.11, were obtained by traversing a 5-hole probe at midspan and at $0.5c_{ax}$ downstream of the trailing edge for $Ma_1 = 0.12$. According to this figure, the wake velocity defect progressively increases lowering the incidence angle. The downstream Mach number distribution reduces for +/-10° incidence angles and then reduces even more for the +/-20° cases; this is due to the progressive reduction of inlet cross section. However, the exit flow angle almost remains unchanged, showing that inlet incidence angle doesn't affect the exit flow angle.

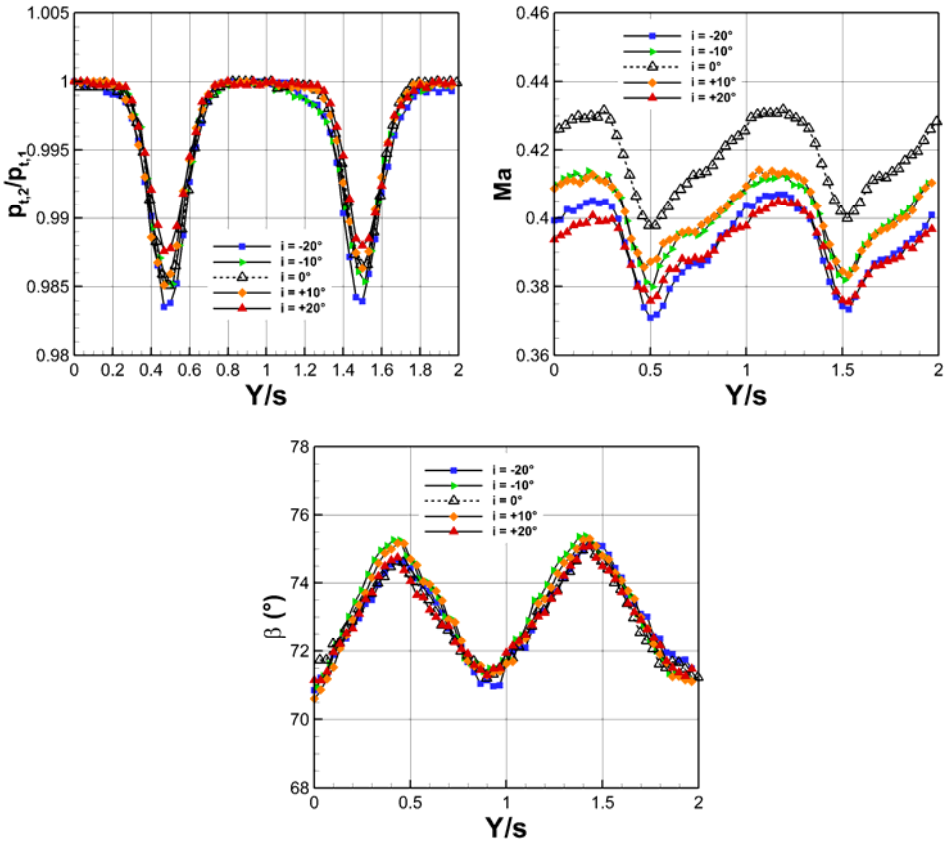

Fig. 5.11- Vane wake profiles at cascade exit; total pressure ratio, Mach number and β.

The influence of incidence on secondary flows behavior was investigated by traversing 5-hole probe through the half passage; starting from midspan toward the endwall and for two vane pitches. Fig. 5.12 illustrates the kinetic energy loss coefficient and the vorticity distributions with superimposed the secondary velocity vectors for various incidence angles. As expected, strong variation took place in the secondary flow when the incidence angle is changing. Considering 0° incidence angle as the reference, when it comes to the positive incidence angle the loss core linked to the passage vortex is widened and moves towards the midspan, while its peak value slightly increased and in the meanwhile, overturning is increasing. The 2D wake region gets smaller in spanwise direction, and with 3D flow effects extending up to about 40% of the vane span when i =+20°.

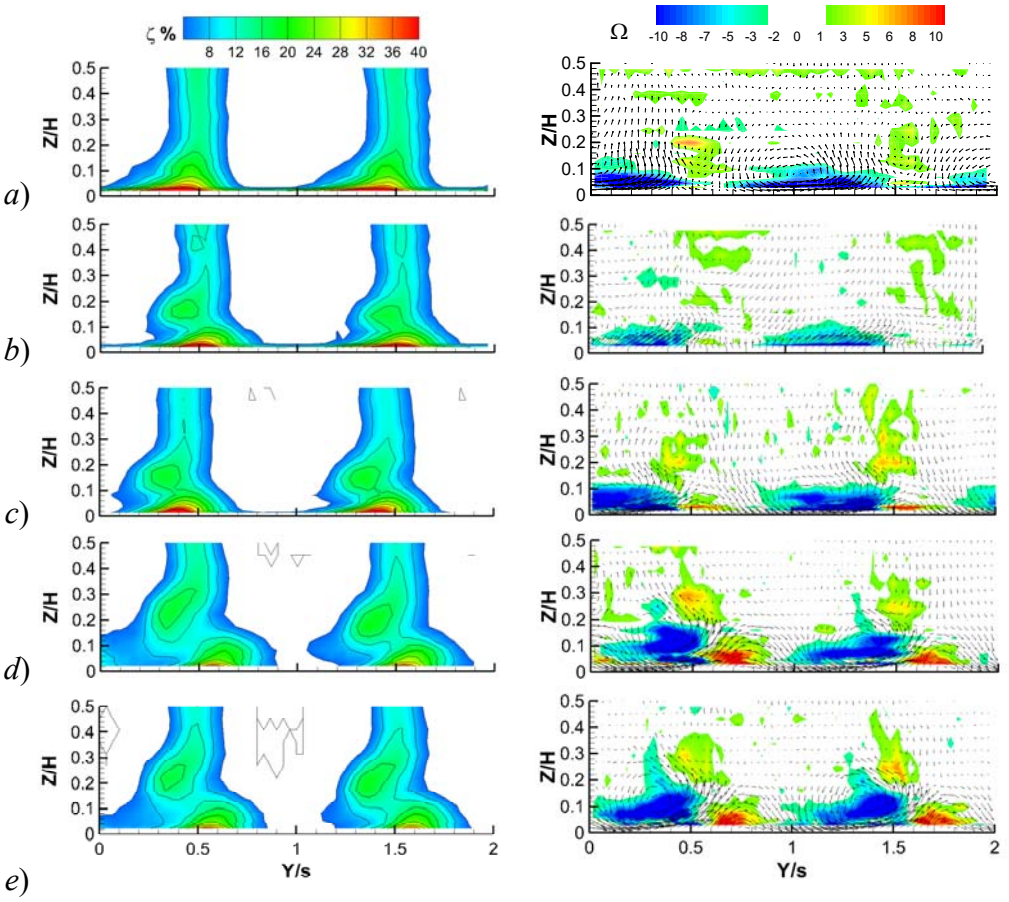

Fig. 5.12- Kinetic energy loss and vorticity distributions ($0.50c_{ax}$ – $Ma_1 = 0.12$): *a*) i = -20°, *b*) i = -10°, *c*) i = 0°, *d*) i = +10° and *e*) i = +20°.

The corner vortex is also intensified, as clearly shown by the vorticity distribution. All these modifications are coherent with the increased end wall cross flow, with the increased vane front loading (see Fig. 5.7), with the displacement separation lines upstream of the vane leading edge, illustrated in Fig. 5.9 (c) and with the increase in the spanwise extension of the suction side region affected by the passage vortex, illustrated in Fig.5.10 (c). On the other side, the loss core associated with the passage vortex progressively disappears when moving to a negative incidence; the peak loss moves towards the end wall, while the 2D wake region gets wider in spanwise direction with slightly higher losses. This is consistent with the reduced front loading on the vane

reported in Fig. 5.7 (specially at the lower tested i = -20°) and with the flow visualization; in particular, shift of separation lines toward the vane leading edge, illustrated in Fig. 5.9 (a) and the reduction in the spanwise extension of the region affected by the passage vortex along the vane suction side, illustrated in Fig.5.10 (a). Comparing +10° and -10° incidence cases, it confirms that the positive incidence displays a much stronger influence on secondary flows development, since -10° results are similar to those at 0°, while the +10° aerodynamics resembles more the +20° incidence case.

The span wise distribution of pitch averaged losses and deviation angle for the tested configurations are plotted in Fig. 5.13. According to these results, one could note that negative incidence contributes in reducing the passage vortex related peak loss, especially at -20°. Positive incidences instead move the passage vortex towards mid span, slightly increasing its peak value, in the meanwhile increasing the overturning.

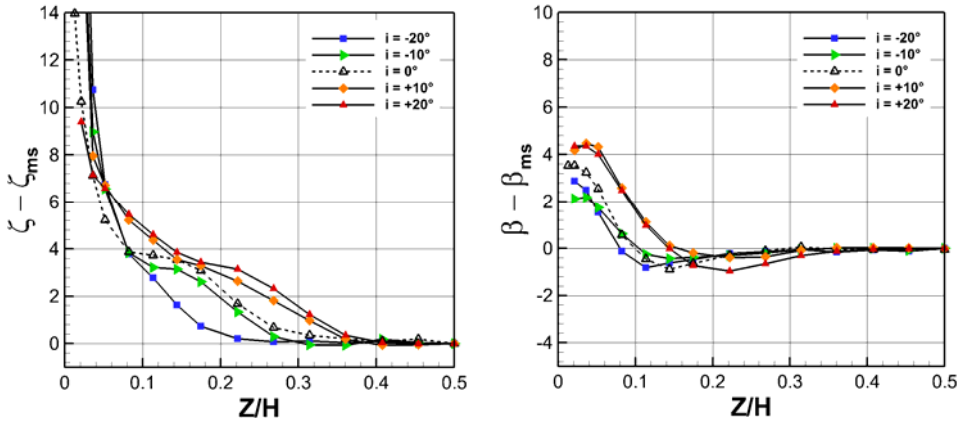

Fig. 5.13- Span wise distributions of: (*left*) kinetic energy loss coefficient and (*right*) deviation angle

5.2. Cooled Cascade

Moving to the cooled cases, it has to be remembered that the cascade was cooled both from vane leading edge and platform. As it was indicated before, endwall cooling was realized through a slot located upstream of the leading edge plane to simulate the gap between combustor and stator platforms; vane showerhead cooling is realized through 4 rows of cylindrical holes evenly distributed around the stagnation line. Air was used as the coolant. The information regarding the injection condition could be found in Table 5.5.

Table 5.5- Injection Coolant properties *(blowing ratio and mass flow rate)*

	Vane Showerhead			*Purge Gap*		
	Min	*Nom*	*Max*	*Min*	*Nom*	*Max*
BR	2.2	2.7	3.2	0.4	0.5	0.6
%MFR	0.39	0.49	0.59	1.4	1.9	2.4

5.2.1. *Aerodynamics of the Cooled Cascade*

Heat transfer study wouldn't be valuable without the aerodynamic information, therefore aerodynamic investigation was done on cooled cascade in advance. 5-hole probe traversing at midspan downstream of the vane cascade gives the information about the wake profile at cascade exit. The test was done at Ma_1 = 0.12 and for the nominal injection condition of both SH and PG. Results are plotted for one wake (*central cooled blade*) in Fig. 5.14.

A progressive velocity defect reduction is observed when reducing the inlet flow incidence. Similar variations also take place in the exit flow angle distributions. This could be related to the shift in stagnation position: moving from -20° to +20° more and more coolant is diverted towards the suction side, resulting in a stronger impact on the boundary layer development along this side of the vane.

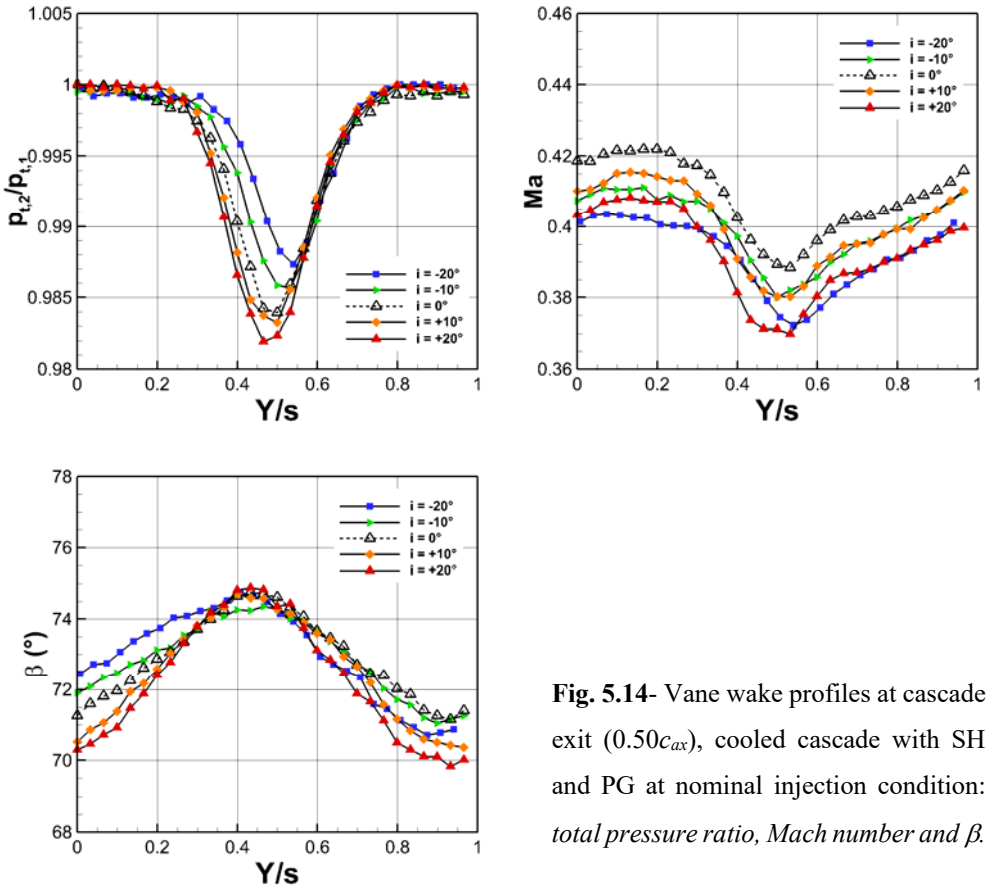

Fig. 5.14- Vane wake profiles at cascade exit ($0.50c_{ax}$), cooled cascade with SH and PG at nominal injection condition: *total pressure ratio, Mach number and β.*

3D flow field investigations downstream of the cooled cascade was done at multiple injection condition combinations. Based on the previous experiments, +20° and -20° incidence angles have shown a strong impact on the solid cascade. Thus for these two incidence angles a set of experiments were designed: 3 tests with both SH and slot blowing at variable blowing ratio *M* (i.e. both at *Nom*, *Min* and *Max* injection condition); a test only with slot blowing at its nominal *M*; and finally a test with only SH blowing at its nominal *M*. For other incidence angles, results are only presented for *Nom* injection condition of vane showerhead and purge slot. Fig. 5.15 and 5.16 plot the kinetic energy loss coefficient and vorticity distributions with superimposed the secondary velocity vectors, respectively. Note that plots only show the second vane wake, as periodicity was good enough to investigate only one vane passage.

Comparing to what was reported at solid cascade condition (Fig. 5.12), huge variations in secondary flow structure take place when the cascade is cooled, in particular when the slot is purging. In +20° incidence, the 2D wake region at midspan almost disappears, with 3D flow effects extending up to Z/H=0.5. The passage vortex loss peak value slightly reduces, but the loss core moves tangentially towards mid channel. A second loss core appears at about 40% of the vane span, coupled with a high positive vorticity region. This indicates the presence of a vortex rotating against the passage vortex, probably corresponding to the SS leg of horseshoe vortex and/or the trailing shed vorticity. Finally, the corner vortex also intensifies

When only the vane SH is blowing (solid platform), secondary flows come back to the uncooled structure (see Fig. 5.12), with only a slight increase in the midspan loss.

At lowest negative incidence (-20°), injection of coolant flow influences the secondary flow structure, but the effect is not as evident as +20°. In fact change in the coolant blowing ratio doesn't significantly affect the secondary flow structures. By the way, the passage vortex loss peak moves tangentially towards the pressure side of the adjacent vane.

A weak trace of a second loss core appears at about 15% of the vane span, coupled with a high positive vorticity region. This indicates the presence of a vortex rotating against the passage vortex, probably corresponding to the SS leg of horseshoe vortex and/or the trailing shed vorticity. Finally, the corner vortex also intensifies. Similar to the +20° incidence angle, the effect of SH cooling on the aerodynamics was negligible.

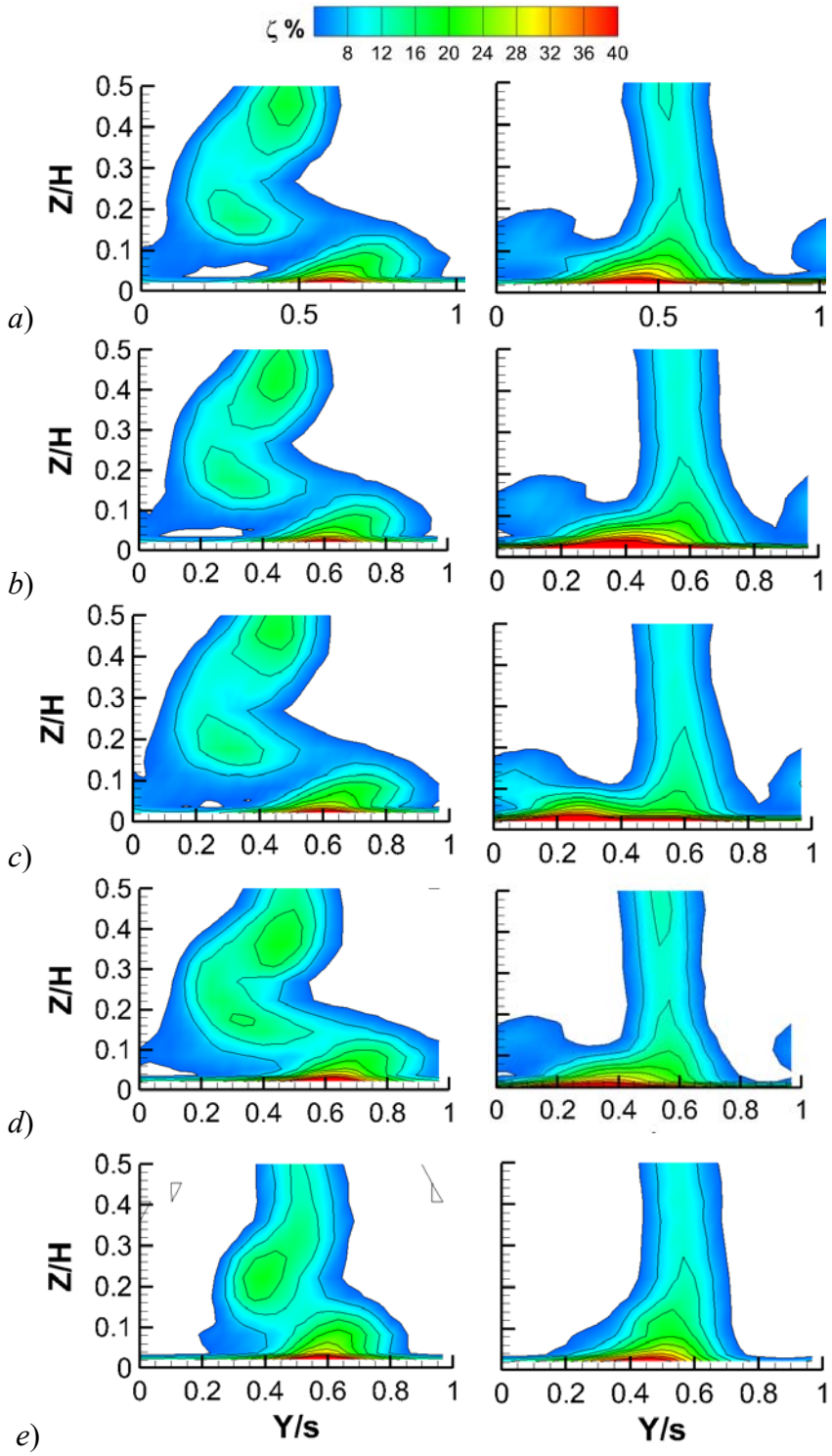

Fig. 5.15- Kinetic energy loss distributions, left plots at i = +20° and right plots at i = -20° *a*) All Nom, *b*) All Min, *c*) All Max, *d*) SP only Nom and *e*) *SH* only Nom.

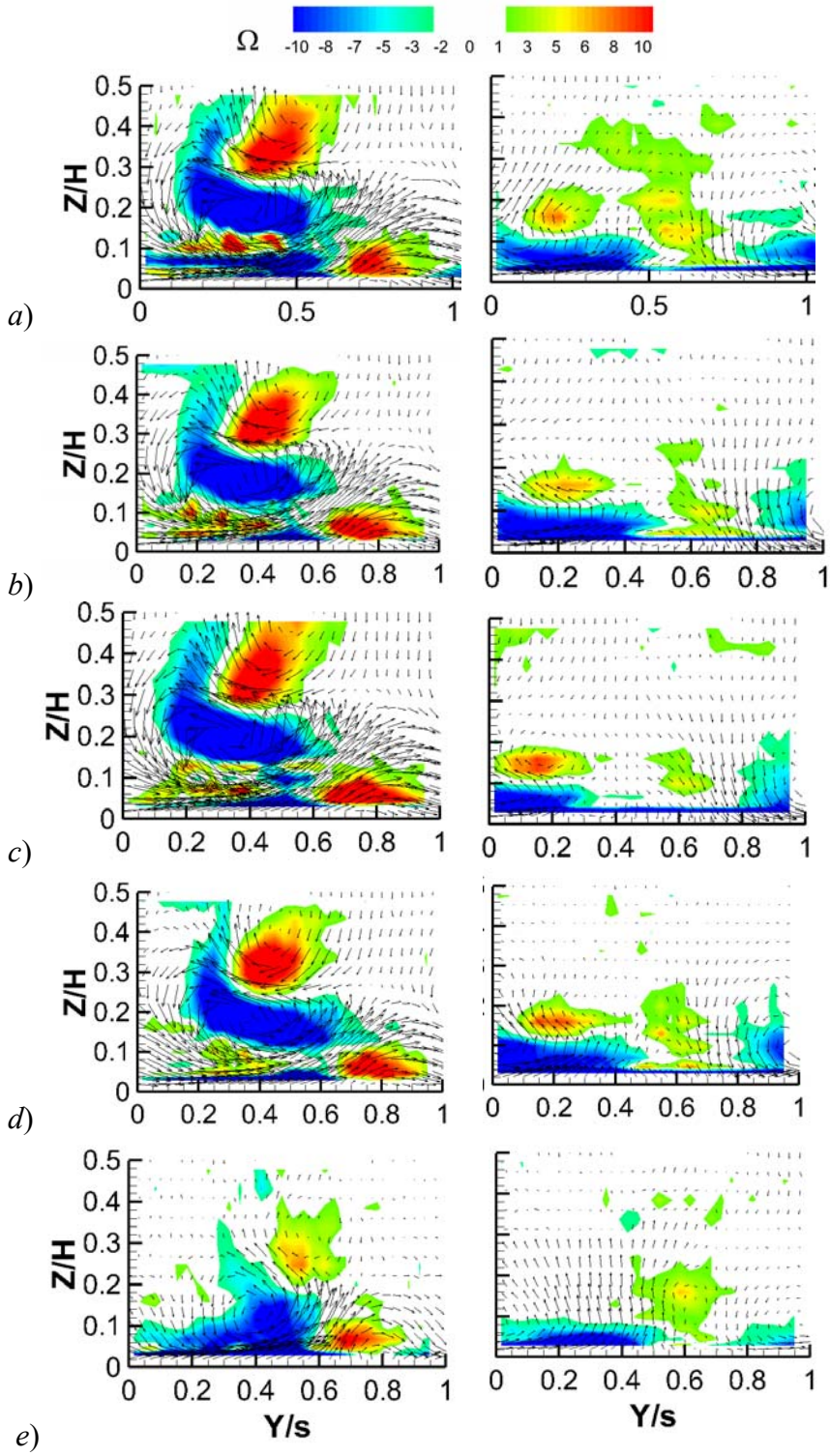

Fig. 5.16- Vorticity distributions with secondary velocity vectors, left plots at $i = +20°$ and right plots at -20° *a*) All Nom, *b*) All Min, *c*) All Max, *d*) SP only Nom and *e*) SH only Nom

To have a better insight into this, the spanwise distribution of pitch averaged losses and deviation angle for the tested configurations was calculated for +20° and -20° incidence angles and are shown in Fig. 5.17 and Fig. 5.18, respectively. The midspan loss and flow angle values have been used as a reference for the analysis of secondary flows effects. Looking at +20° figure, it can be noticed that the spanwise loss distribution is only marginally affected by coolant injection, despite the measured huge local loss variations. When the slot is blowing, loss highly increases at the end wall, while it reduces close to zero at about *0.25Z - 0.3Z*. From -20° figure we can see that when the slot is blowing, loss highly increases at the end wall and over the region extending up to about *0.2Z*. For both incidence angles, injection variation doesn't significantly influence their behavior. When only the vane is cooled at nominal *M*, no differences with respect to the solid case are detected for both incidence angles.

Concerning the deviation angle, only marginal variations can be observed in -20°. Both underturning and overturning are slightly increased by slot injection, only marginally affected by slot and SH injection condition. SH injection alone does not modify the spanwise distribution of deviation angle. On the other hand, much higher variations can be observed in highest incidence angle. Overturning and underturning are both strongly increased by slot

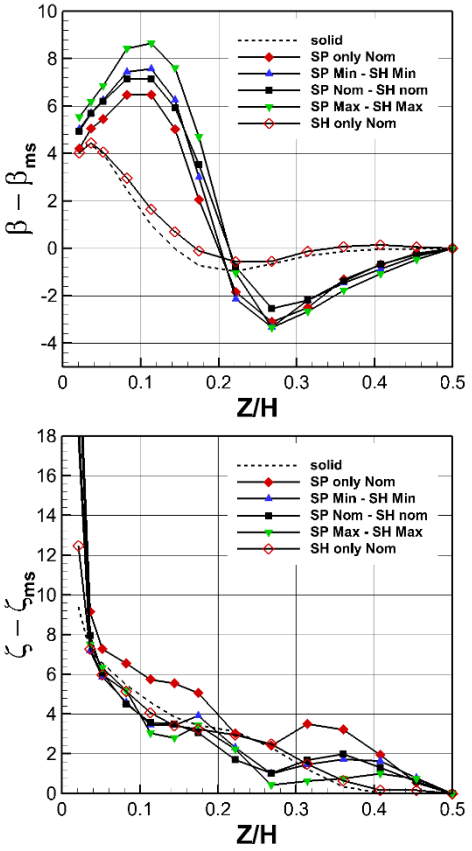

Fig. 5.17- Span wise distributions of kinetic energy loss coefficient and deviation angle for +20° in multiple injection conditions

injection and their effects, extend a lot towards midspan. While the case with both slot and SH injection shows only a marginal influence.

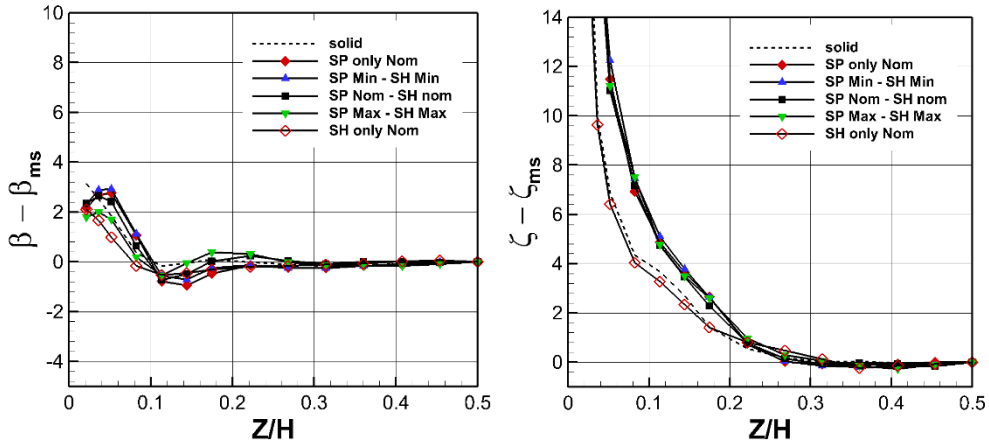

Fig. 5.18- Span wise distributions of kinetic energy loss coefficient and deviation angle for -20° in multiple injection

Considerable insight has been gained with regard to the aerodynamic study of the lowest and the highest incidence angles when the cascade is cooled. Multiple cooling conditions were investigated and based on the results, as stated before, for other incidence angles test matrix were limited to nominal injection of purge slot and vane showerhead. The test matrix is summarized in Table 5.6.

Fig. 5.19 demonstrates the 3D flow field comparison for various incidence angles, all at nominal *M*. The averaged losses and deviation angle is plotted in Fig. 5.20. Considering 0° incidence angle as the reference, coolant injection through the upstream slot and at vane showerhead does not change the 3D flow general structure. Passage and corner vortex related loss peaks are intensified and the 2D wake region shows larger losses. Coolant

Table 5.6- Test matrix for aerodynamic investigations of cooled cascade

Case	*M_PG*	*M_SH*	*Incidence Angle*				
			-20	*-10*	*0*	*+10*	*+20*
1	*Nom*	*Nom*	✓	✓	✓	✓	✓
2	*Min*	*Min*	✓	-	-	-	✓
3	*Max*	*Max*	✓	-	-	-	✓
4	*Nom*	-	✓	-	-	-	✓
5	-	*Nom*	✓	-	-	-	✓

injection through the slot is also responsible for the widening of the passage vortex loss region in the tangential direction close to the wall. An incidence reduction down to -10° does not show significant differences with respect to the previous case. As it was indicated before, much stronger variations are observed at the lowest tested incidence of -20°. On the other side, positive incidence results in a strong modification of secondary flows structures, already at i =+10°, with only minor modifications when further increasing i up to +20°. Comparing +10° and -10°, it should be noted that the positive incidence displays a more impressive phenomenon since -10° results are very similar to those at 0°, while the +10° aerodynamics resembles the +20°.

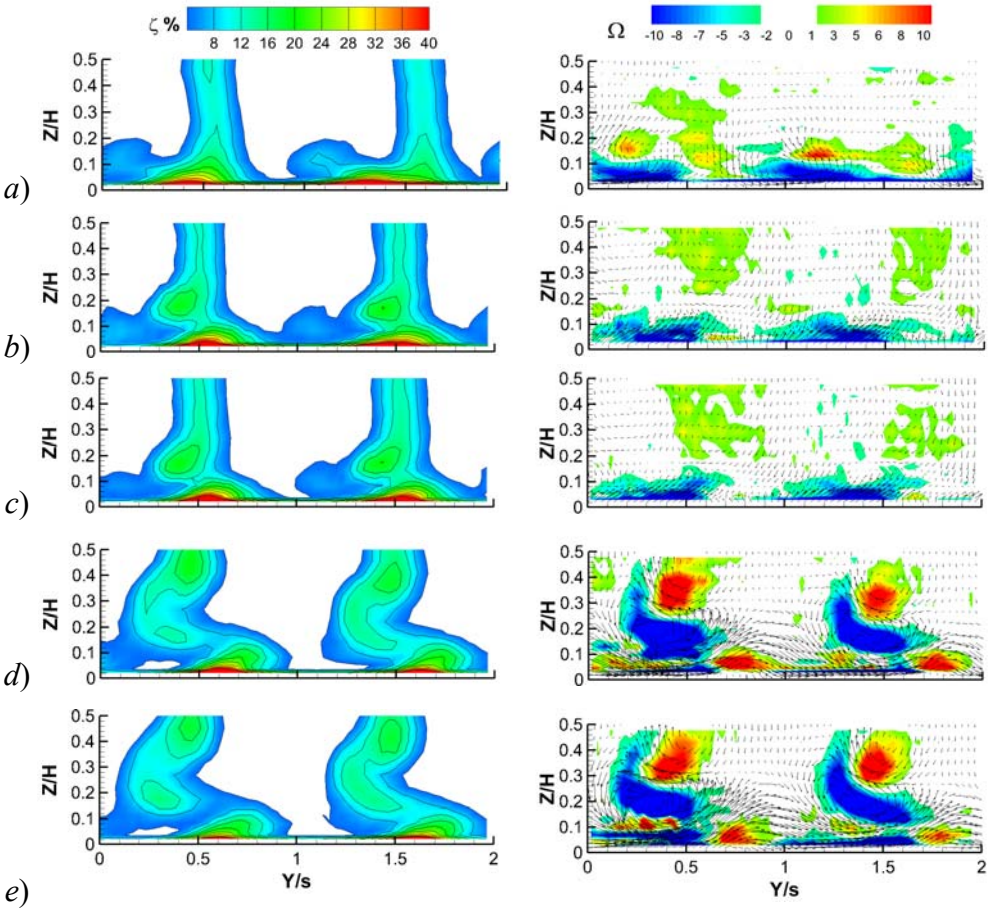

Fig. 5.19- Kinetic energy loss and vorticity distributions, Ma_1=0.12, (All at nominal condition on both SH and PG): *a*) i = -20°, *b*) i = -10°, *c*) i = 0°, *d*) i = +10° and *e*) i = +20°

Generally speaking, in cooled cascade condition, corner vortex and the vorticity intensifies. To better quantify the impact of incidence on the flow behavior downstream of the cascade, Fig. 5.20 reports the span averaged distributions of kinetic energy loss coefficient and deviation angle, all derived from 5-hole probe measurements. Results for the solid and the cooled cascades are reported side by side.

Starting from the 0° incidence case and the solid cascade, reducing the incidence initially does not give significant variations. But at -20° incidence a significant reduction in the passage vortex related peak loss is observed. Positive incidences move the passage vortex towards midspan, slightly increasing its peak value, in the meanwhile increasing the overturning. Negative incidence values do not affect the spanwise distribution of both loss and deviation angle in the cooled cascade, neither at the lowest tested incidence of -20°. Conversely, positive incidences have a strong impact especially on the deviation angle distribution, with a huge variation of both under and overturning. A redistribution of loss rather than a loss increase takes place.

Finally, mass averaging the local loss distributions all over the passage, overall kinetic energy loss coefficients were computed. The so-called primary definition is here considered:

$$\bar{\bar{\zeta}} = \frac{\overline{\overline{U_{2,is}^2}} - \overline{\overline{U_2^2}}}{\overline{U_{2,is,ms}^2}} \tag{5-1}$$

All data are referred to the solid cascade with 0° incidence. Fig. 5.21 shows that solid and cooled cascades behave in a similar way when changing the inlet flow angle. Negative incidence values result in a small decrease of losses that instead strongly increase at positive values. Coolant injection is responsible for an increase in the loss level that ranges from about 0.6% at -20° up to about 1.0% at +20°. This is consistent with the strongest interaction between coolant

injected through the slot and secondary flows, the latter intensified by the positive incidence.

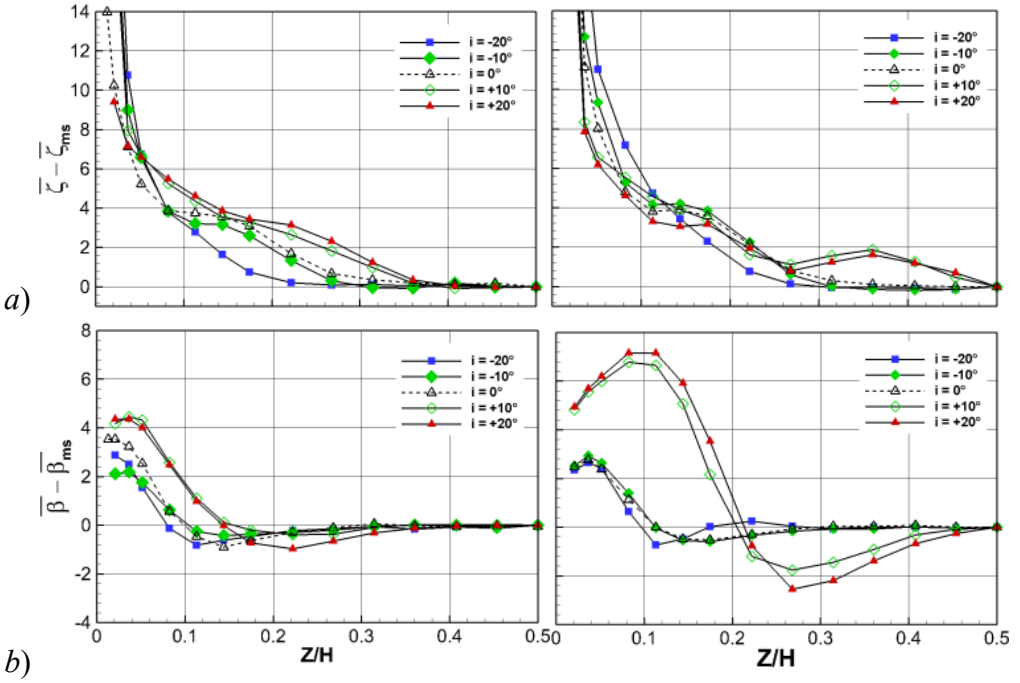

Fig. 5.20- Spanwise *a*) loss distribution (primary definition) and *b*) flow angle deviation for variable incidences, Ma_1=0.12; solid cascade *left* and cooled cascade *right* (cooling at nominal condition on both SH and PG)

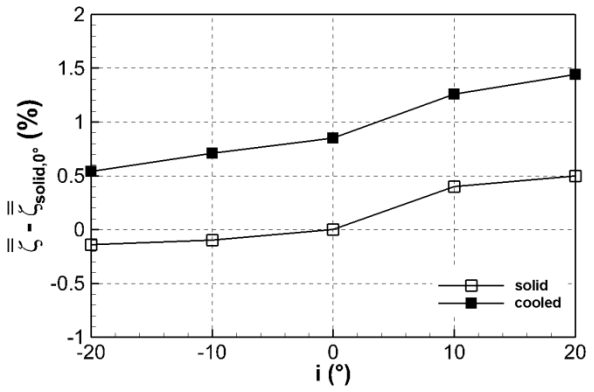

Fig. 5.21- Mass averaged overall kinetic energy loss coefficient for solid and cooled cascade

5.2.2. *Platform film cooling effectiveness*

Once the aerodynamic characteristics were investigated, the heat transfer experiments were done on the cooled platform. For each incidence angle, tests have been done in 3 injection condition; PG blows at its *Nom*, *Min* and *Max* blowing ratio (*M*), but SH was injected only at its nominal blowing ratio since the SH injection variation doesn't affect the endwall cooling. The mainstream temperature remains at ambient temperature, while coolant flow from the slot was heated up to about 40°C in advance, then it was injected through the purge gap. In the beginning, tests have been repeated twice: first heating the SH flow and then with SH flow at room temperature. As again no significant differences were observed, in all tests SH was blown at room temperature. Fig.5.22~5.24 illustrate calculated platform effectiveness distributions with PG at *Min*, *Nom,* and *Max* blowing ratios, respectively for variable incidence. Note that the vane depicted in the figures with a dotted line indicates the real position of the vane on the end wall. All tests have been carried out at nominal Mach number (Ma_1 = 0.12) and with high inlet turbulence intensity of about 9%.

From these figures it can be perceived that mass flow injected through the slot is able to effectively protect the end wall front part and the mid channel section, leaving the leading edge and pressure side region uncooled, whatever the incidence angle. Slot blowing ratio increment results in an improvement of thermal protection, with coolant that moves further downstream, up to the vane leading edge and more approaching the pressure side. This behavior is more evident at negative incidence angles, in particular for i = -20°. For i = +20°, thermal protection marginally increases with rising the blowing rate only upstream of the leading edge. Focusing the attention on the 0° incidence case, a loss in effectiveness downstream of the passage vortex separation line takes place, however, an improvement in efficiency is seen when slot injection increases to *Max* condition.

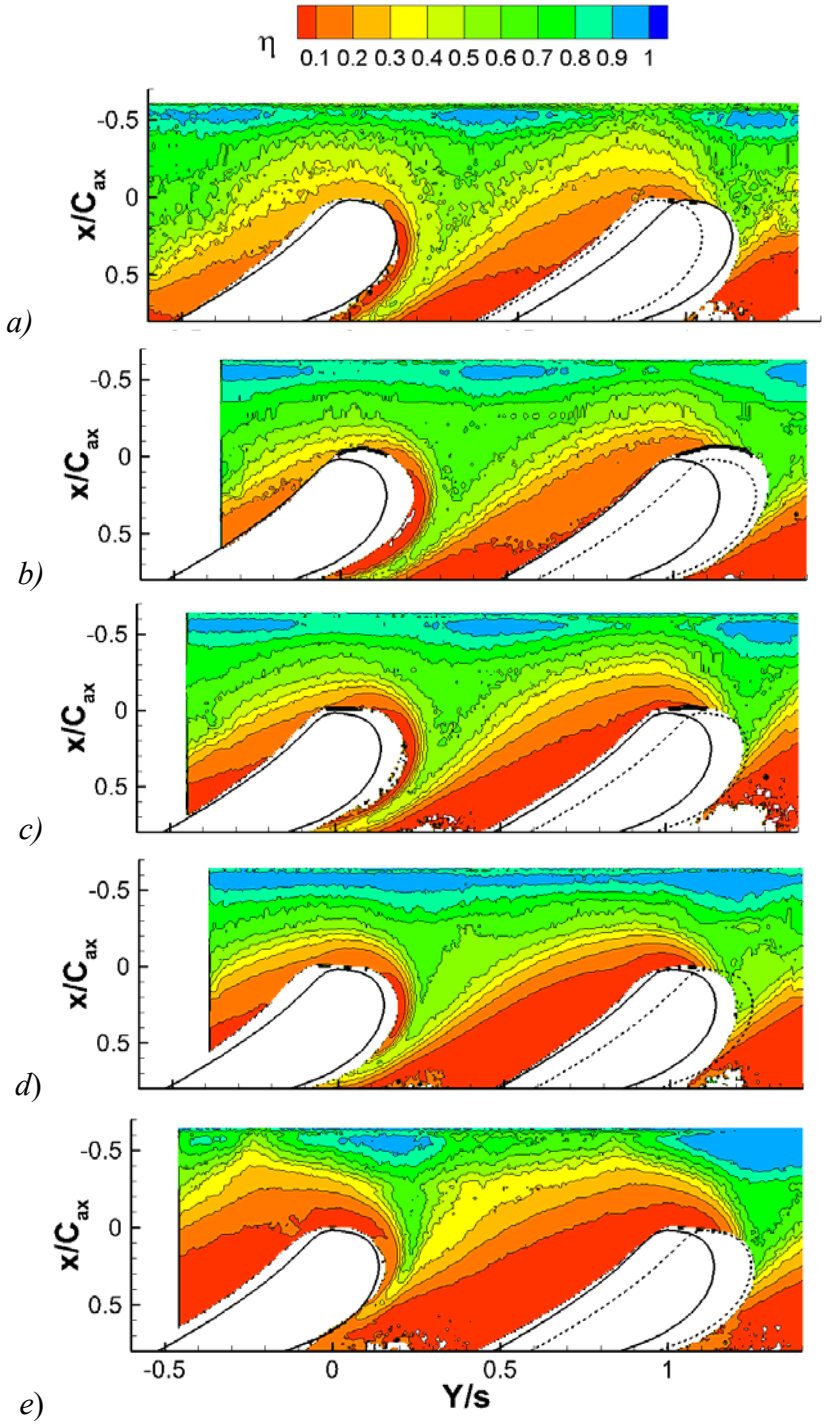

Fig. 5.22- Film cooling effectiveness distributions; All at Ma_1 = 0.12, *PG* at *Min* and *SH* at *Nom*; *a*) i = -20°, *b) i* = -10°, *c*) i = 0° *d*) i = +10° and *e*) i = +20°

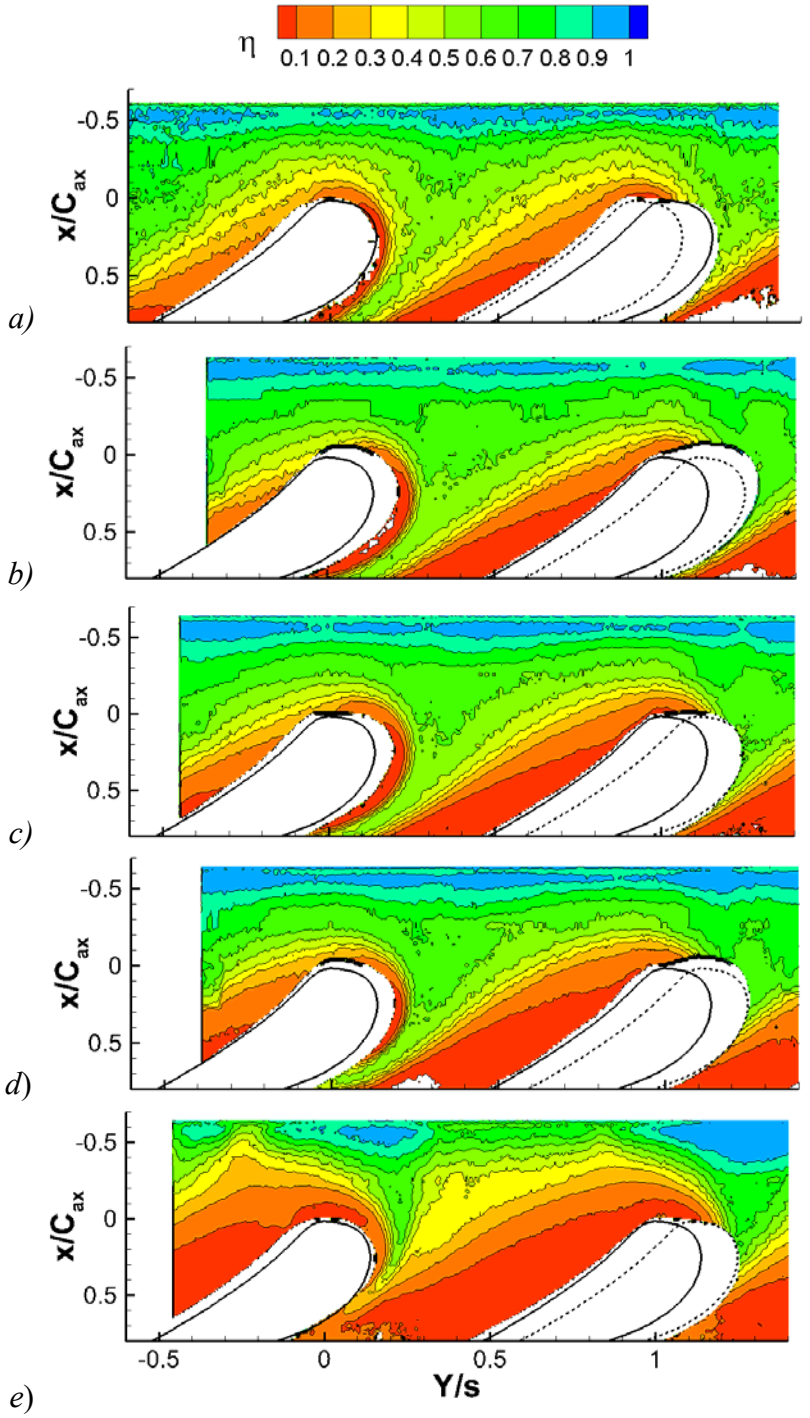

Fig. 5.23- Film cooling effectiveness distributions; All at $Ma_1 = 0.12$, *PG* and *SH* at *Nom*; *a*) $i = -20°$, *b)* $i = -10°$, *c*) $i = 0°$ *d*) $i = +10°$ and *e*) $i = +20°$

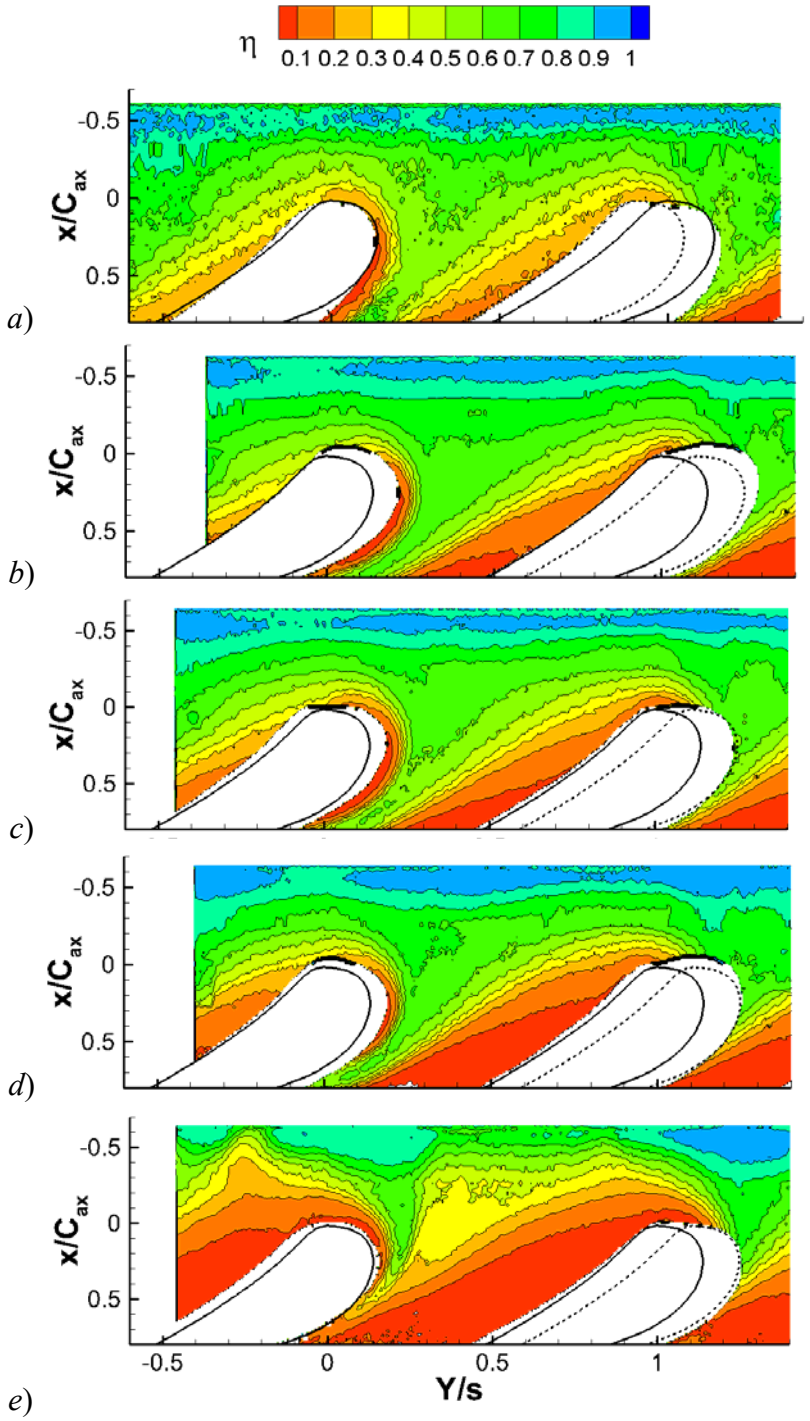

Fig. 5.24- Film cooling effectiveness distributions; All at Ma_1 = 0.12, *PG* at *Max* and *SH* at *Nom*; *a*) i = -20°, *b) i* = -10°, *c*) i = 0° *d*) i = +10° and *e*) i = +20°

As far as incidence variation is concerned, a general decrease in thermal protection is attained at positive incidence, while at negative incidence the thermal protection is similar to the 0° incidence case, with only a slight improvement inside of the passage. Comparing the η distribution in *Nom* slot blowing ratio at +20° with the one measured at -20° incidence, and considering the flow visualizations, the following relevant differences can be noted:

i) coolant discharge along the slot is less uniform, due to the stronger influence of stagnation upstream of the cascade;

ii) the coolant stays farther from the leading edge because of a higher intensity of horseshoe vortex legs;

iii) persistency of coolant inside of the passage decreases because of the more intense action of the passage vortex.

When considering the intermediate incidence angles of -10° and +10°, it is evident that negative incidence values do not give strong variations to the coolant footprint on the end wall, in accordance with the aerodynamic results. Conversely, positive incidence angles result in a significant loss of protection already at i = +10°, again in agreement with the strengthening of horseshoe and passage vortex activity.

Worth to note the progressive shift in the position at which the coolant impact on the vane suction side while changing the incidence: at -20° coolant is found rear in the passage, while at +20° no coolant is found after $X/c_{ax} = 0.5$.

To gain a better insight of inlet flow incidence angle variation on the endwall adiabatic film cooling effectiveness, data from the *Nom* slot injection (Fig.5.23) were laterally averaged over one pitch ($0 < Y/s < 1$) to get the mean distribution along the axial direction. The result is plotted in Fig. 5.25. According to this figure, it can be clearly seen that the worst case here is $i = +20°$, where the curve

keeps its significant distance from other cases. For the other incidence angles also, η_{av} drastically decreases, independently from what the incidence angle is. Increasing *i* to positive values translates into a progressive reduction in the platform thermal protection. Reducing the incidence below 0° instead has a marginal impact on the thermal protection of the platform. This is in agreement with secondary flows behavior.

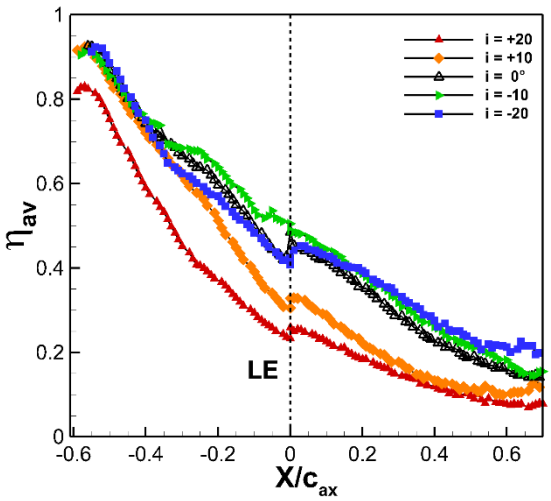

Fig. 5.25- Laterally averaged adiabatic film cooling effectiveness (η_{av}) for variable incidence at nominal blowing ratio

In order to quantify in a unique value the thermal protection capability, data were also averaged over the full area of the same single passage. Results are shown in Fig. 5.26 as a function of incidence, taking the 0° incidence case as a reference. A huge decrease in overall effectiveness takes place for positive incidence while no significant differences take place for negative i values. At nominal blowing ratio, the overall effectiveness decreases of about 6.7% when changing the incidence from 0° to +10°. Increasing the incidence up to +20°, the effectiveness decreases of 16.1%.

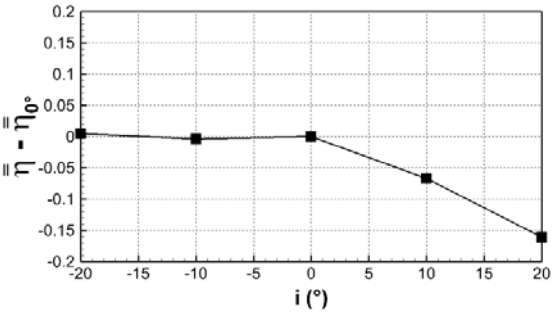

Fig. 5.26- Area averaged adiabatic film cooling effectiveness ($\bar{\eta}$) for variable incidence at nominal blowing ratio

5.2.3. *Vane showerhead film cooling effectiveness*

The adiabatic film cooling effectiveness for the vane showerhead cooling scheme was then investigated using TLC technique. Fig.5.27 illustrates the procedure in which these data were obtained. As it was mentioned in chapter4, due to the limitations, borescope was used for acquiring the TLC color play on the vane. For each BR, tests were being divided into two different experiments, one on PS and other on SS of the vane.

Fig. 5.28 shows calculated film cooling effectiveness on the vane in variable incidence angles and for *Min*, *Nom* and *Max* showerhead blowing ratios, respectively. All tests have been done at $Ma_1 = 0.12$ and purge slot was injected at its nominal blowing ratio (since it doesn't affect the vane film cooling effectiveness).

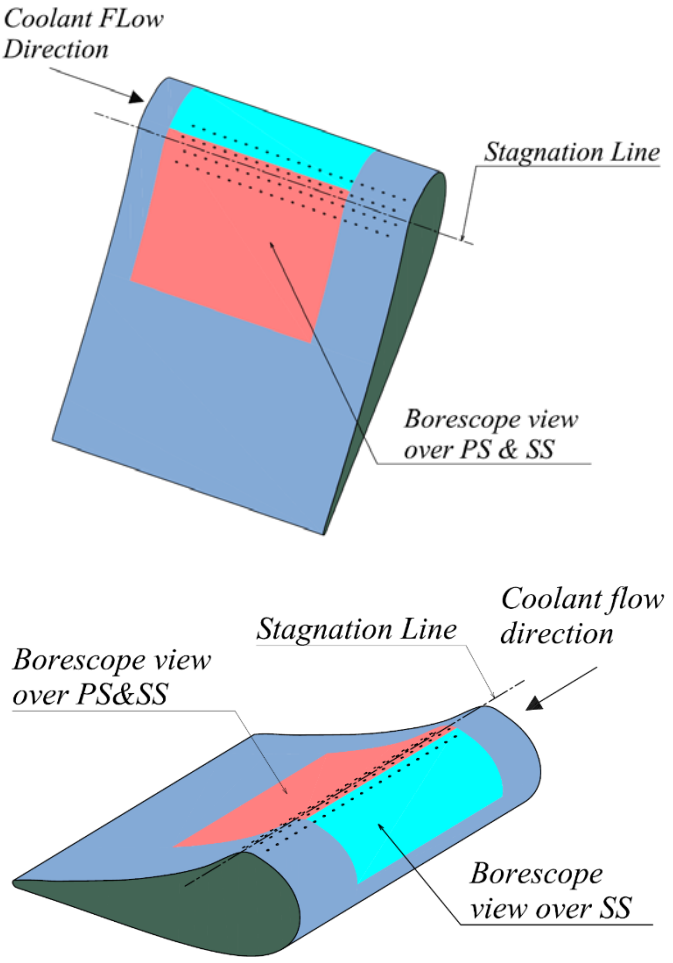

Fig. 5.27- Vane film cooling effectiveness investigations using the borescope

Please note that *s* is the surface coordinate, i.e. a curvilinear coordinate always tangent to the vane surface; it is here normalized with the vane chord *C*. The origin for this coordinate is the stagnation point. In each picture, the position of the stagnation line derived from solid vane load distribution has been reported as a dashed line.

Focusing on these figures, one can note the accumulation of the coolant on tip region of the vane. This is due to the hole angle towards the tip which results in a well cooling performance at midspan, leaving the region close to the hub poorly cooled. Starting with 0° incidence the highest efficiency levels can be observed in between the SS holes, with the thermal protection quickly decreasing along the SS front portion. When blowing ratio *M* is increased, a small gain in thermal protection takes place especially along the PS, but when *M* is reduced the thermal protection strongly decreases all over the vane surface. Moving to the positive incidence angle, i = +10°, results in a reduction in thermal protection along the pressure side of the vane, which is worsened when moving to the highest incidence angle. For i = +20°, this reduction is coupled with a small increase along the front suction side.

Moving to the negative incidence angles instead gives a better performance on the PS, but it loses the thermal protection on the SS, which in i = -20° practically no thermal protection is present along the SS. i = -10° shows a slight improvement comparing to -20°, but it still failed to protect the SS of the vane. These results are well consistent with the displacement of the stagnation point around the leading edge from pressure to suction side when incidence angle varies from + 20° to -20°. To better understand the effect of blowing ratio (*M)* on film cooling effectiveness, data from each plot in Fig. 5.28 were laterally averaged (η_{av}) and the result is reported in Fig. 5.29 for various incidence angles.

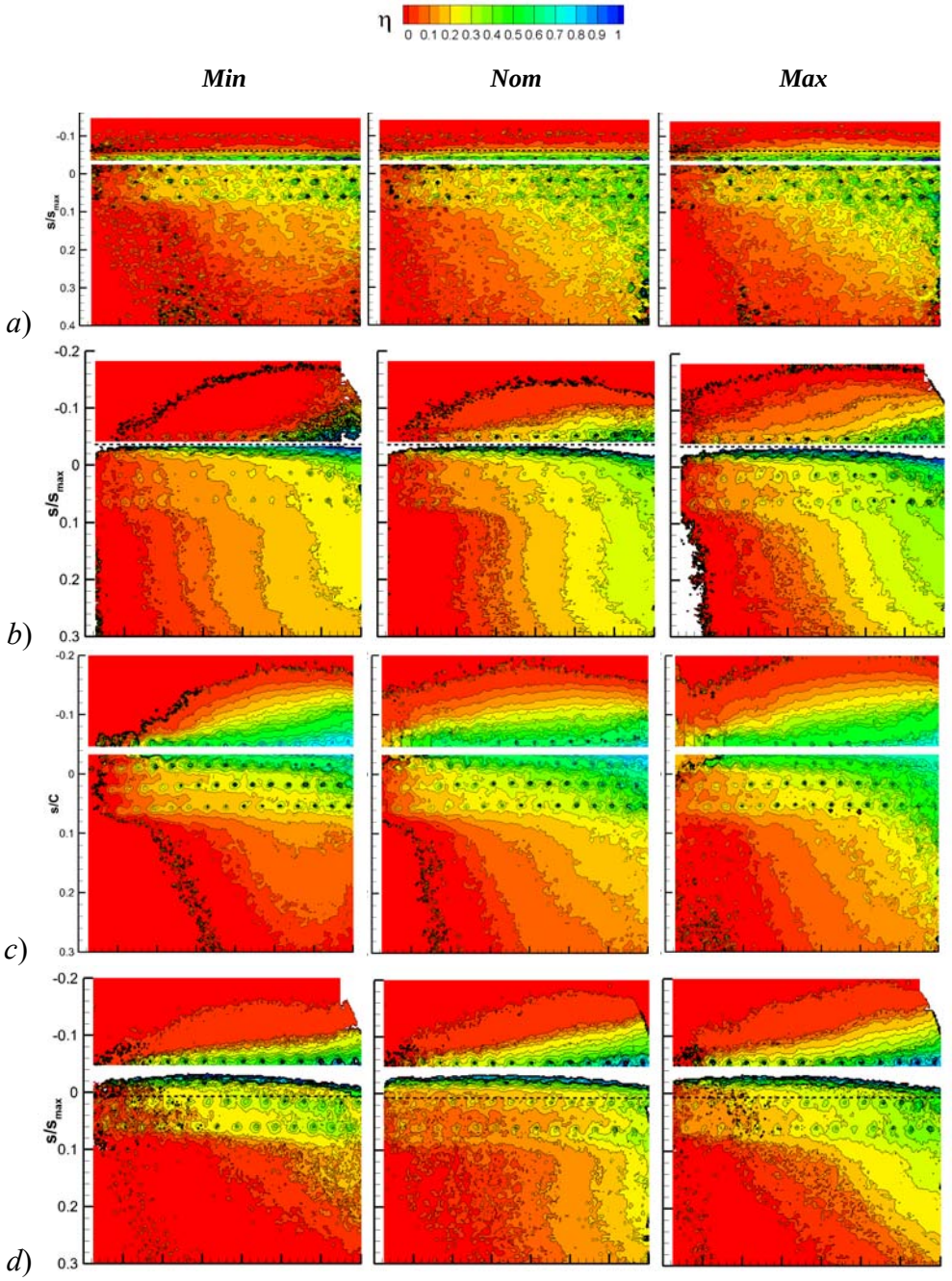
η
0 0.1 0.2 0.3 0.4 0.5 0.6 0.7 0.8 0.9 1
Min
Nom
Max
a)
b)
c)
d)
s/s_max
s/C

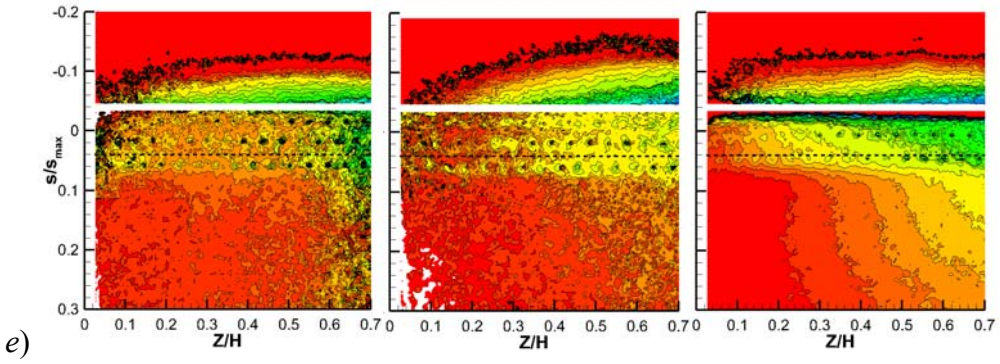

Fig. 5.28- Film cooling effectiveness distributions; All at $Ma_1 = 0.12$, *PG* at *Nom* and varied *SH*; *a*) $i = -20°$, *b) i* = -10°, *c*) $i = 0°$ *d*) $i = +10°$ and *e*) $i = +20°$

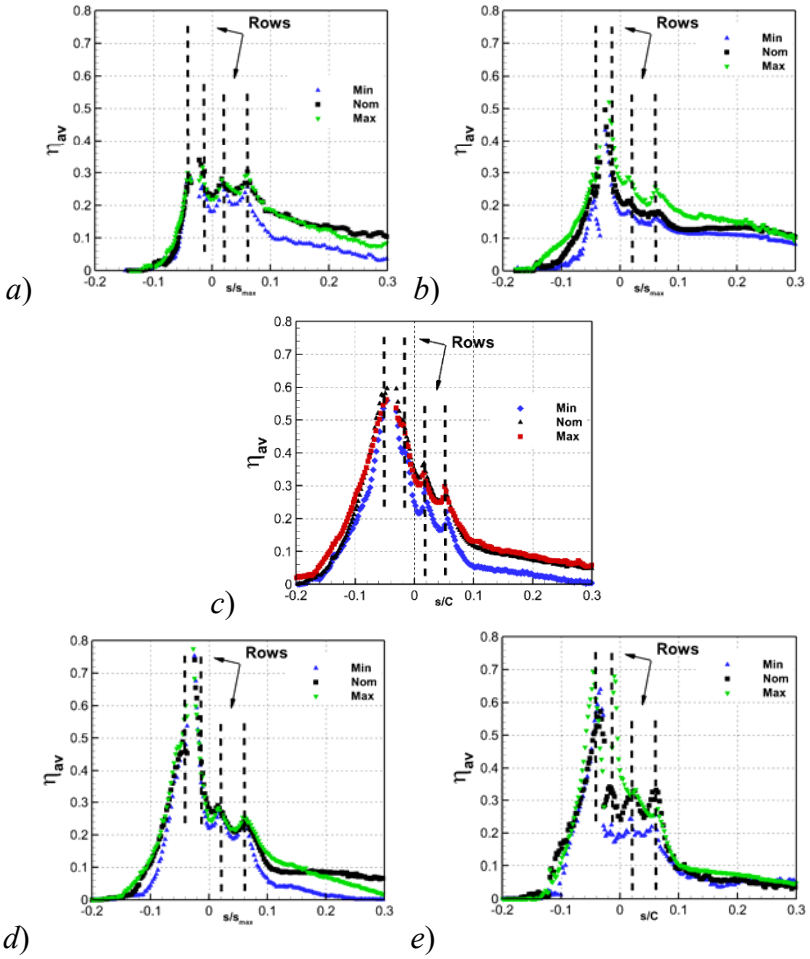

Fig. 5.29- Laterally averaged vane film cooling effectiveness for variable blowing ratio: *a*) $i = -20°$, *b) i* = -10°, *c*) $i = 0°$ *d*) $i = +10°$ and *e*) $i = +20°$

Looking at the Fig. 5.29, almost in all incidence cases increasing the coolant flow from *Min* blowing ratio to the *Nom*, the distribution of the coolant over the vane increases and it doesn't significantly change in *Max* blowing ratio. Only a marginal enhancement is seen at $i = +10°$ in *Max* injection.

To better observe the incidence influence on the vane film cooling effectiveness, lateral average at nominal injection for each incidence angle are plotted together and is presented here in Fig. 5.30. According to this figure, comparing to the reference incidence angle $i = 0°$, the effect of incidence angle is apparent: negative incidence cases leads to a progressive increase in thermal protection along the pressure side and a reduction along the front suction side; positive incidence instead is responsible for the pressure side poor efficiency and a slight efficiency enhancement in suction side.

In order to quantify the thermal protection capability of showerhead cooling in a unique value, data were averaged over the full area and is plotted as a function of the blowing ratio *(M)* and also as a function of incidence angle. The results are illustrated in Fig. 5.31. Area averaged for SS and PS were calculated separately at SH *Nom* injection and is reported in Fig. 5.32 as a function of *i*.

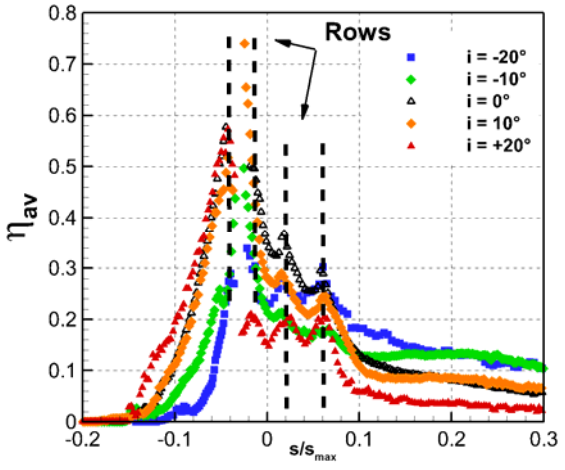

Fig. 5.30- Laterally averaged adiabatic film cooling effectiveness for the cooled vane in variable incidence angles and at nominal blowing ratio

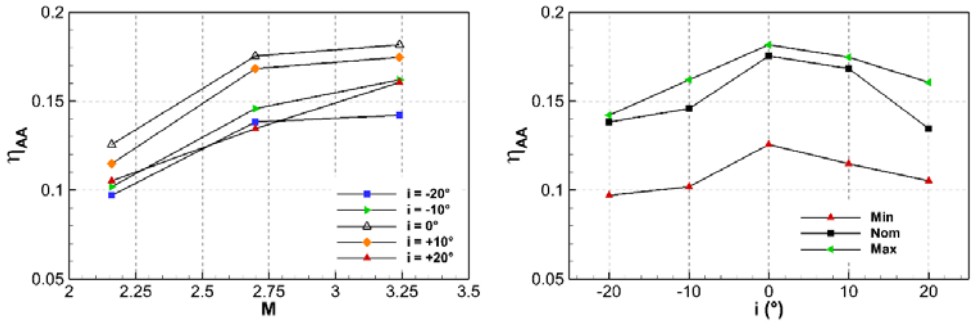

Fig. 5.31- Area averaged adiabatic film cooling effectiveness for variable injection condition *(left)* and for variable incidence *(right)*

This overall efficiency undergoes a continuous improvement by increasing the injection up to the maximum blowing. The maximum efficiency is attained in 0° incidence case. Moving either way to positive and negative incidence cases, lose in thermal protection on the vane is happening. From this figure it can be concluded that unlike the endwall cooling, positive incidences are not the worst case anymore, in fact negative incidence also showed a poor cooling performance. This means that the movement in stagnation line adversely affects cooling performance mostly on negative angles, while in positive incidence it only affects the +20 incidence angle. To define the reason of such behaviors, we have to look at Fig 5.32 where area averaged effectiveness for suction side and pressure side were separately computed for the different incidence angles. This figure clearly reveals that positive and negative incidence angles sweep away the coolant respectively to the suction side and pressure side of the vane. Looking at the suction side, area-averaged effectiveness sharply increases up to $i = 0°$, then levels on when moving up to +20°. Along both pressure and suction side, a plateau is observed in between 0° and +10°. This could be explained by their stagnation point, which for these two cases remains in between the same two rows of cooling hole.

These results add to the importance of incidence considerations in designing stage of showerhead cooling configuration.

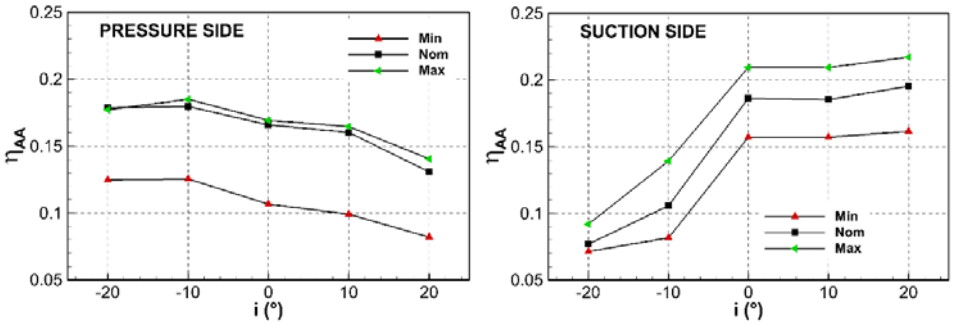

Fig. 5.32- Area averaged film cooling effectiveness for variable incidence for suction side and pressure side of the vane

6
Conclusions

The analysis presented in this study was generally divided into two general divisions: *I)* Aerodynamic analysis of the cooled and solid cascade and *II)* Heat transfer investigation and analysis. Adiabatic film cooling effectiveness *(η)* on the platform and on the vane was obtained from TLC measurements. Aerodynamic characteristic of the cascade was obtained using LDV technique, 5-hole probe traversing and instrumented vane. The aerothermal effects of incidence variation were investigated in different cases. In each case, the effort was made to take all the key parameters into account, in order to contribute a thorough study to the body of literature, which includes, by the knowledge of the author, only a few studies regarding the subject. To draw the conclusions, the data from the previous chapters are summarized here to provide a better understanding about the incidence effects on aerothermal performance of a nozzle cascade.

Starting from the aerodynamics, the effect of the inlet flow incidence angle was clearly seen in this research. A variation in stagnation point position on vane leading edge was observed when the inlet flow incidence angle was changed in the range of -20° to +20°. The stagnation line moves toward the pressure side of the vane in positive incidence angles and conversely moves to the suction side of the vane in negative incidence angles. In case of showerhead film cooling on the vane, the coolant split between the pressure side and suction side was strictly controlled by the position of stagnation line. Change in

stagnation also showed an influence on the local blowing ratio of the injection holes. As it was reported before, from load distribution static pressure at holes exit location was computed for the different inlet flow angles and it was reported in chapter five (Fig. 5.8). According to this figure, the outlet pressure on the cooling holes is varying at different incidence angle. The result of such behavior is that the blowing ratio a specific row of holes becomes significantly high when the stagnation is aligned to this row, therefore the most coolant flow from this row would be lost in the mainstream. This is an important parameter in designing the showerhead cooling configuration since in real engine the variation in incidence angle is happening along the span, due to the swirl flow.

This phenomenon, stagnation line movement, was clearly observed in the investigation of vane adiabatic film cooling effectiveness. In particular, moving to the positive incidence angle, i = +10°, results in a reduction in thermal protection along the pressure side of the vane, which is become worsened when moving to the highest incidence angle. For i = +20°, this reduction is coupled with a small increase along the front suction side. Moving to the negative incidence angles instead gives a better performance on the PS, but it losses the thermal protection on the SS, which in i = -20°, practically no thermal protection is present along the SS. i = -10° shows a slight improvement comparing to -20°, but it still failed to protect the SS of the vane.

3D flow field investigations revealed that for positive incidence angle the passage vortex moves towards the midspan, its peak value slightly increased and in the meanwhile, overturning is increasing. These effects intensifies in the cooled cascade; in which the 2D wake substituted with a higher 3D loss core coupled with a high positive vorticity region. On the other side, a negative incidence angle contributes to reducing the passage vortex related peak loss, especially at -20; however, in cooled cascade condition, corner vortex and the vorticity intensifies. In addition, comparing +10° and 10°, it should be noted

that the positive incidence displays a more impressive phenomenon since -10° results are very similar to those at 0°, while the +10° aerodynamics resembles the +20° incidence case.

Platform cooling results showed that the adiabatic cooling effectiveness *(η)* undergoes a general decrease in thermal protection at positive incidence, while at negative incidence the thermal protection is more similar to the 0° incidence case, with only a slight improvement inside of the passage. The worst case here happened at the +20° incidence angle. This is due to the fact that in +20° the passage vortex intensifies and when the coolant is blowing from the purge slot, it failed to properly protect the endwall. By moving to +10° incidence angle, an improvement was noticed and further reducing the incidence below the 0° angle almost has no significant impact on the thermal protection of the endwall. This is also in agreement with the secondary flow behavior.

To draw a conclusion from the thermal point of view, it goes without saying that facing a swirling flow could be detrimental to the first nozzle vane cascade. If the flow faces the nozzle vane with a positive incidence angle, it would be a damage risk for the endwall. Thus, it is recommended to consider an extra cooling configuration on the endwall, such as endwall film cooling, specially where the passage vortex separation lines takes place. Negative incidence is not a threat to the endwall cooling, in fact, it partially enhances it respecting to the reference incidence case. However, since it affects the vane cooling performance, considerations should be made, also for this case. Shaped holes could be a better configuration for the showerhead cooling scheme since the jet stays more on the surface, and it lifts-up from the vane surface at higher blowing ratio. In addition, considerations should be made to protect the hub side of the vane using a different showerhead cooling holes pattern and distribution.

It’s obvious that the high-temperature high-pressure flow exiting the combustor chamber doesn’t contain a certain incidence, instead, the flow

behavior in a real engine is such a complex phenomenon to assign a certain incidence. Therefore, this study could be considered as a basic research to understand how the inlet flow incidence could affect the NGV behavior. These findings could add to a growing body of literature, specially for CFD developers, since the experimental data regarding this subject are not so abundant in the literature.

Nomenclature

c	Vane chord
C_p	Specific heat at constant pressure
C_v	Specific heat at constant volume
D	Hole diameter
$DR = \rho_c \,/\, \rho_\infty$	Density ratio
FE	Flow energy
ft	Foot
g	Gravitational acceleration
H	Blade height, Enthalpy
h	Enthalpy
i	Incidence
IE	Internal energy
KE	Kinetic energy
L	Hole length
m	Mass flow
M	Blowing ratio $= {\rho_c V_c}/{\rho_\infty V_\infty}$
Ma	Mach number
n	Polytropic exponent
PE	Potential Energy
P	Pressure, hole pitch
Q	Heat transfer, volume flow rate
Q_A	Heat added to the cycle
R	Gas constant
Re	Isentropic outlet Reynolds number
s	Vane pitch, Entropy, Second
T	Temperature

Tu	Turbulence intensity level
U	Local mean velocity, Internal Energy
V, v	Velocity
W	Mechanical work
X,Y,Z	Cascade coordinate system
z	Elevation

Greeks

α	Angle
β	Flow angle (axial direction),
β_p	Pressure ratio
γ	Specific heat ratio C_p/C_v
Δ	Difference
δ	Thickness
η	Film cooling effectiveness
Λ	Integral length scale
ν	Kinematic viscosity
ρ	Flow density
$\zeta = (U_{2is}^2 - U_2^2)/\overline{U}_{2is,ms}^2$	Kinetic energy loss coefficient
Ω=$\Omega_s c/U_1$	Vorticity

Subscripts

1	Inlet
2	Outlet
AA	Area averaged
ax	Axial
av	averaged
aw	Adiabatic wall
c	Cooling flow, Compressor
cnst	Constant
f	Cooling film
g	gas
is	Isentropic condition
s	Isentropic

opt	Optimum
sys	System
surr	Surrounding
th	Thermal
T	turbine
w	Wall
∞	Free stream
sys	System
surr	Surronding

Overbar

_	Pitch averaged
=	Area averaged, Mass averaged

Abbreviations

$BR = {\rho_c V_c}/{\rho_\infty V_\infty}$	Blowing ratio
CAD	Computer-aided design
CFD	Computational fluid dynamics
DLE	Dry low emission
FEM	Finite element method
Fig	Figure
fps	Frame per second
GE	General electric
HSI	Hue, saturation and intensity
HTC	Heat transfer coefficient
HW	Hot Wire
LDV	Laser Doppler velocimetry
LED	Light emitting diode
LPM	Lean-premixed combustor
LSTR	Large scale turbine rig
Max	Maximum injection condition
MFR	Mass flow rate
Min	Minimum injection condition
ms	Midspan

NGV	Nozzle guide vane
Nom	Nominal injection condition
OTDF	Overall temperature distribution factor
PG	Purge gap
PS	Pressure side of the vane
px	Pixels
RGB	Red, Green and Blue color channles
RMS	Root mean square
RTDF	Radial temperature distribution factor
SAS	Scale adaptive simulation
SH	Showerhead
SP	Slot purge injection flow
SS	Suction side of the vane
SST	Shear stress transport
TBC	Thermal Barrier Coating
TLC	Thermochromic liquid crystals

References

[1] Powerplant technology, M.M. El-Wakil

[2] Johan J. Moverare. Sten Johansson, Roger C. Reed, Deformation and damage mechanisms during thermal–mechanical fatigue of a single-crystal superalloy, Acta Materialia, Volume 57, Issue 7, April 2009, Pages 2266-2276

[3] R. Schafrik, S. Walston, Challenges for high temperature materials in the new millennium, R.C. Reed, K.A. Green, P. Caron, T.P. Gabb, M.G. Fahrmann, E.S. Huron, *et al.* (Eds.), Superalloys 2008, The Minerals, Metals & Materials Society, Warrendale, PA (2008), p. 3

[4] B. Lakshminarayana, "Fluid Dynamics and Heat Transfer of Turbomachinery", 1996, John Wiley & Sons, Inc.

[5] M. Sautner, S. Clouser, J.C. Han, "Determination of Surface Heat Transfer and Film Cooling Effectiveness in Unsteady Wake Flow Condition", AGARD Conference Proceedings 527, 1993.

[6] J.C. Han, S. Dutta, S. V. Ekkad, "Gas Turbine Heat Transfer and Cooling Technology", Taylor & Francis, 2000.

[7] I. Dincer, Y. A. Cengel, "Energy, Entropy and Exergy Concepts and Their Roles in Thermal Engineering", Entropy 2001, 3(3), 116-149.

[8] IE Treager, "Aircraft gas turbine engine technology", 1979, Gregg Division McGraw Hill.

[9] E. E. Halila, D. T. Lenahan, T. T. Thomas, "Energy Efficient Engine", GE Co., NASA CR-167955.

[10] J. D. Mattingly, “Elements of Gas Turbine Propulsion”, McGraw-Hill, New York, 1996

[11] K. Takeishi, M. Matsuura, S. Aoki, T. Sato, “An experimental Study of Heat Transfer and Film Cooling on Low Aspect Ratio Turbine Nozzles”, ASME *J. Turbumach*., 112, 488, 1990.

[12] R.J. Goldstein, “Film cooling”, Advances in Heat Transfer, 7, 321–379, 1971.

[13] H. Moustapha, M. F. Zelesky, N. C. Baines, D. Japikse, “Axial and Radial Turbines” Concepts NREC, 2003.

[14] D. G. Bogard, K. A. Thole, “Gas Turbine Film Cooling”, Journal of Propulsion and Power, Vol.22, N0. 2, March-April 2006.

[15] W. Lazik, Th. Doerr, S. Bake, R. v. d. Bank, L. Rackwitz “Development of Lean-Burn Low-NOx Combustion Technology at Rolls-Royce Deutschland” ASME Turbo Expo 2008, GT2008-51115, 2008.

[16] G. Schmid, A. Krichbaum, H. Werschnik, H. P. Schiffer, “The Impact of Realistic Inlet Swirl in a 1 ½ Stage Axial Turbine”, Proceeding of ASME Turbo Expo 2014, GT2014-26716, 2014.

[17] M. D. Turrell, P. J. Stopford, K. J. Syed, and E. Buchanan. CFD simulation of the flow within and downstream of a high-swirl lean premixed gas turbine combustor. In ASME Turbo Expo 2004: Power for Land, Sea, and Air, pages 31–38, 2004. doi: 10.1115/GT2004-53112.

[18] Turrell, M. D., Stopford, P. J., Syed, K. J., and Buchanan, E., 2004. “CFD simulation of the flow within and downstream of a high-swirl lean premixed gas turbine combustor”. Proceedings of ASME Turbo Expo (GT2004-53112).

[19] Klapdor, E. V., 2011. “Simulation of combustor-turbine interaction in a jet engine”. P.h.D thesis, TÜ Darmstadt.

[20] Klinger, H., Lazik, W., and Wunderlich, T., 2008. “The engine 3e core engine”. Proceedings of ASME Turbo Expo, 2008(43116),pp. 93–102

[21] Qureshi, I., Smith, A. D., and Povey, T., 2013. “Hp vane aerodynamics and heat transfer in the presence of aggressive inlet swirl”. Journal of Turbomachinery, 135.

[22] Giller, L., and Schiffer, H.-P., 2012. “Interactions between the combustor swirl and the high pressure stator of a turbine”. Proceedings of ASME Turbo Expo, 2012(GT2012-69157).

[23] Schmid, G., and Schiffer, H.-P., 2012. “Numerical investigation of inlet swirl in a turbine vane cascade”. Proceedings of ASME Turbo Expo (GT2012-69397), June.

[24] Luque, S., Kanjirakkad, V., Aslanidou, I., Lubbock, R., Rosic, B., and Uchida, S., 2015A new experimental facility to investigate combustor–turbine interactions in gas turbines with multiple can combustors”.

[25] Yin, H., Qin, Y., Ren, J., Jiang H.,”Effect of Inlet Swirl on the Model Leading Edge of Turbine Vane”, ASME Turbo Expo 2013, Texas, USA, June 2013, GT2013-94471.

[26] Yin, H., Liu, S., Feng, Y., Li, M., Ren, J., Jiang, H., “Experimental test rig for combustor-turbine interaction research and test results analysis”, Proceeding of ASME Turbo Expo 2015: Turbine Technical Conference and Exposition, Montréal, Canada, June 2015, GT2015-42209.

[27] S. Shahpar, and S. Caloni, 2012. “Aerodynamic optimization of high pressure turbines for lean-burn combustion system”. Proceedings of ASME Turbo Expo (GT2012-69228), June.

[28] Rosic, B., Denton, J. D., Horlock, J. H., and Uchida, S., 2012. “Integrated combustor and vane concept in gas turbines”, Journal of Turbomachinery, 134(3), p. 031005.

[29] S. Jacobi, C. Mazzoni, K. Chana, and B. Rosic. “Investigation of unsteady flow phenomena in first vane caused by combustor flow with swirl”. 2016, GT2016-57358.

[30] H. Werschnik, J. Hilgert, M. Bruschewski, H. P. Schiffer “Combustorr-Turbine Aerothermal Interaction in an Axial Turbine – Influence of Varied Inflow Conditions on Endwall Heat Transfer and Film cooling Effectiveness”. Proceedings of ASME Turbo Expo 2016: Turbomachinery Technical Conference and Exposition, Seoul, Korea, June 2016, GT2016-57171.

[31] H. Werschnik, J. Hermann, H. P. Schiffer, C. Lyko “The Influence of Combustor Swirl on Pressure Losses and the Propagation of Coolant Flows at The Large Scale Turbine Rig (LSTR)”, Proceedings of 12th European Conference on Turbomachinery Fluid dynamics & Thermodynamics (ETC12), Stockholm, Sweden, ETC2017-139, 2016.

[32] C. Camci, T. Arts, “Effect of Incidence on Wall Heating Rates and Aerodynamics on a Film Cooled Transonic Turbine Blade”, Transaction of ASME, 90-GT-46, 1990.

[33] A. Perdichizzi, V. Dossona, “Inlet angle and Pitch-Chord Effects on Secondary Flows Downstream of a Turbine Cascade” Transactions of ASME, 92-GT-184, 1992.

[34] A. Perdichizzi, H. Abdeh, G. Barigozzi, M. Henze, J. Krueckels, “Aerodynamic Performance of a Nozzle Vane Cascade with a Generic Nonuniform Inlet Flow Condition-Part I: Influence of Nonuniformity Location”, Journal of Turbomachinery, Vol. 139, March 2017.

[35] G. Barigozzi, H. Abdeh, A. Perdichizzi, M. Henze, J. Krueckels, “Aerodynamic Performance of a Nozzle Vane Cascade with a Generic Nonuniform Inlet Flow Condition-Part II: Influence of Purge and Film Cooling Injection”, Journal of Turbomachinery, Vol. 139, October 2017.

[36] D. E. Sokolowski, “Toward improved durability in advanced aircraft engine hot sections”, ASME Turbo Expo 1988, Amsterdam, Netherland June 5-9, 1988.

[37] G. Barigozzi, A. Perdichizzi, M. Henze, J. Krueckels, “Aerodynamic and Heat Transfer Characterization of a Nozzle Vane Cascade With and Without Platform Cooling”, Proceedings of ASME Turbo Expo, June 15-19, 2015.

[38] C. Camci, K. Kim, S. A. Hippensteele, “A New Hue Capturing Technique for the Quantitative Interpretation of Liquid Crystal Images Used in Convective Heat Transfer Studies”, J. Turbomach. 114, 765-775, 1992.

[39] D. G. Gregory-Smith, C. P. Graves, J. A. Walsh, “Growth of Secondary Losses and Vorticity in an Axial Turbine Cascade,” ASME Journal of Turbomachinery, 110(1), pp. 1–8, 1988.

[40] M. D. Barringer, K. A. Thole, M. D. Polanka, J. P. Clark, and P. J. Koch. “Migration of Combustor Exit Profiles Through High Pressure Turbine Vanes”. ASME Journal of Turbomachinery, 131:021010–1–10, 2009.

[41] A. Lefebvre, “Gas Turbine Combustion (Combustion: An International series)”, Taylor & Francis, Philadelphia, PA, 1999.

[42] S. V. Alekseenko, P. A. Kuibin, and V. L. Okulov, “Theory of ConcentratedVortices”, Springer, Berlin, pp. 309–378, 2007.

[43] S.J. Kline, F.A. McClintock, “Describing uncertainties in single sample experiments”, Journal of Mechanical Engineering (1953) 3–8.

[44] G. Wagner, E. Schneider, J. von Wolferdorf, P. Ott, B. Weigand, “Method for analysis of showerhead film cooling experiments of highly curved surface”, Experimental Thermal and Fluid Science, vol. 31, 381-389, 2007.

[45] M. L. Nathan, T. E. Dyson, D. G. Bogard, S. D. Bardshaw, “Adiabatic and overall effectiveness for the showerhead film cooling of a turbine vane”, Journal of Turbomachinery, vol. 136, 2014.

[46] I. S. Jung, J. S. Lee, “Effects of orientation angles on film cooling over flat plate boundary layer temperature distribution and adiabatic film cooling effectiveness’, Transaction of ASME, 99-GT-143, 1999.

[47] Syred, N., and Khalatov, A., 2006, Advanced Combustion and Aerothermal Technologies, ed., Springer.

[48] Dunn-Rankin, D., and Therkelsen, P., 2016, Lean Combustion Technology and Control, ed., Elsevier, 2nd edition.

[49] M. Insinna, D. Griffini, S. Salvadori, F. Martelli, 2014, "Conjugate heat transfer analysis of a film cooled high-pressure turbine vane under realistic combustor exit flow conditions", ASME paper GT2014-25280.

[50] M. Insinna, D. Griffini, S. Salvadori, F. Martelli., 2015, "Effects of Realistic Inflow Conditions on the Aero-Thermal Performance of a Film-Cooled Vane", Proc. of the 11th European Turbomachinery Conference (ETC11), Madrid, Spain, March 23-27.

[51] D. Griffini, M. Insinna, S. Salvadori, F. Martelli, 2016, "Clocking Effects of Inlet Nonuniformities in a Fully Cooled High-Pressure Vane: A Conjugate Heat Transfer Analysis", J. Turbomach, 138, pp. 021006-1:10.

[52] G. Barigozzi, S. Ravelli, 2015, “Combined Experimental and Numerical Study of Showerhead Film Cooling in a Linear Nozzle Vane Cascade” Proceedings of ASME Turbo Expo 2015, Montréal, Canada, GT2015-42397.

[53] J. Hilgert, M. Bruschewski, H. Werschnik, H. P. Schiffer, 2017, “Numerical Studies on Combustor-Turbine Interaction at the Large Scale Turbine Rig (LSTR)”, Proceedings of ASME Turbo Expo 2017, Charlotte, NC, USA, GT2017-64504.

[54] Krichbaum, A., Werschnik, H., Wilhelm, M., Schiffer, H.- P., and Lehmann, K., 2015. “A Large Scale Turbine Test Rig for the Investigation of High Pressure Turbine Aerodynamics and Heat Transfer with Variable Inflow Conditions”. GT2015-43261, Proceedings of ASME Turbo Expo 2015.

[55] S. Ravelli, G. Barigozzi, 2017, “Comparison of RANS and Detached Eddy Simulation Modeling Against Measurements of Leading Edge Film Cooling on a First-Stage Vane”, Journal of Turbomachinery, Vol. 139.

[56] H. Abdeh, M. Miranda, S. Rouina, G. Barigozzi, 2017, “Development of PSP Technique for Vane Film Cooling Investigations”, Energy Procedia, Vol. 126, P. 802-809.

[57] Sieverding, C.H., 1985, “Recent Progress in the Understanding of Basic Aspects of Secondary Flows in Turbine Blade Passages”, J. Eng. Gas Turbine and Power, 107, pp. 248-257.

[58] Dossena, V., D'Ippolito, G., Pesatori, E., 2004, “Stagger Angle and Pitch-Chord Ratio Effects on Secondary Flows Downstream of a Turbine Cascade at Several Off-design Conditions”, ASME Paper GT2004-54083.

[59] Tsujita, H. and Yamamoto, A., 2014, “Influences of Incidence Angle on 2D-Flow and Secondary Flow Structure in Ultra-Highly Loaded Turbine Cascade”, J. Therm. Science, 23, pp. 13-21.

[60] Kunze, M., Vogeler, K., Crawford, M., Brown, G., 2014, “Single and Multiple Row Endwall Film-Cooling of a Highly Loaded First Turbine Vane with Variation of Loading”, J. Turbomach., 136, pp. 061012-1:14.

[61] Craig, H.R.M. and Cox, H.J.A., 1971, “Performance Estimation of Axial Flow Turbines”, Proc Instn Mech Engrs, 187, pp.32-71.

[62] Y. Huang, V. Yang, “Dynamics and stability of lean-premixed swirl-stabilized combustion” Progress in Energy and Combustion Science 35 (2009) 293–36

[63] H. J. Perkins, “The formation of streamwise vorticity in turbulent flow”, Journal of Fluid Mechanics, (1970), Vol. 44, part 4, pp. 721-740.

[64] Barigozzi, G., Fontaneto, F., Franchini, G., Perdichizzi, A., Maritano, M., Abram, R., “Influence of coolant flow rate on aero-thermal performance of a rotor blade cascade with endwall film cooling”, Proceeding of ASME Turbo Expo 2011, June 6-10, Vancouver, Canada.